



# Multiferroicity and metal-insulator transitions in strongly correlated electron systems

**Author:**

Li, Fei

**Publication Date:**

2015

**DOI:**

<https://doi.org/10.26190/unsworks/2702>

**License:**

<https://creativecommons.org/licenses/by-nc-nd/3.0/au/>

Link to license to see what you are allowed to do with this resource.

Downloaded from <http://hdl.handle.net/1959.4/54247> in <https://unsworks.unsw.edu.au> on 2024-04-29

**MULTIFERROICITY AND  
METAL-INSULATOR TRANSITIONS IN  
STRONGLY CORRELATED ELECTRON  
SYSTEMS**

**FEI LI**

A THESIS SUBMITTED IN FULFILMENT OF THE  
REQUIREMENTS FOR THE DEGREE OF MASTER OF  
SCIENCE



School of Physical, Environmental, and Mathematical Sciences  
The University of New South Wales, Canberra  
January 2015

# Contents

<b>Contents</b>	<b>i</b>
<b>List of Figures</b>	<b>iii</b>
<b>List of Tables</b>	<b>vii</b>
<b>Declaration</b>	<b>viii</b>
<b>Acknowledgements</b>	<b>ix</b>
<b>Abstract</b>	<b>xi</b>
<b>1 Introduction</b>	<b>1</b>
1.1 Multiferroicity . . . . .	1
1.1.1 Incompatibility between ferroelectricity and magnetism	3
1.1.2 Routes to multiferroicity: proper multiferroics . . . . .	4
1.1.3 Routes to multiferroicity: improper multiferroics . . . . .	5
1.2 Metal-insulator transitions and electronic orderings . . . . .	8
<b>2 Experimental principles</b>	<b>12</b>
2.1 X-ray diffraction . . . . .	12
2.1.1 Diffraction geometry . . . . .	13
2.1.2 Diffraction cross section . . . . .	13
2.2 X-ray absorption spectroscopy . . . . .	15
2.2.1 Theory . . . . .	15
2.2.2 Techniques . . . . .	18
2.3 Resonant X-ray diffraction . . . . .	20
2.3.1 Theory . . . . .	20
2.3.2 Diffraction geometry and cross section . . . . .	22
2.4 Scanning Electron Microscopy . . . . .	24
2.5 Magnetization measurements . . . . .	25

<b>3</b>	<b>Synthesis and characterisation of vanadium doped <math>\text{La}_2\text{Ti}_2\text{O}_7</math></b>	<b>28</b>
3.1	Introduction . . . . .	28
3.2	Synthesis and characterization . . . . .	29
3.2.1	Challenges of doping vanadium into $\text{La}_2\text{Ti}_2\text{O}_7$ . . . . .	29
3.2.2	Synthesis . . . . .	30
3.2.3	Crystal structure . . . . .	32
3.2.4	Magnetic properties . . . . .	35
3.3	Conclusion . . . . .	38
<b>4</b>	<b>Oxygen isotope substitution effect on magnetism in multi-ferroic <math>\text{CaMn}_7\text{O}_{12}</math></b>	<b>39</b>
4.1	Introduction . . . . .	39
4.2	Synthesis of $\text{CaMn}_7\text{O}_{12}$ . . . . .	42
4.2.1	Synthesis . . . . .	42
4.2.2	Morphology and composition . . . . .	42
4.2.3	Crystal structure . . . . .	44
4.3	Oxygen substitution effect on magnetism . . . . .	46
4.3.1	Oxygen substitution experiment . . . . .	46
4.3.2	Crystal structure . . . . .	47
4.3.3	Determination of $^{18}\text{O}$ content . . . . .	48
4.3.4	Magnetic properties . . . . .	49
4.4	Conclusion . . . . .	53
<b>5</b>	<b>Investigation of the order parameter of Pr in the filled skutterudite <math>\text{PrRu}_4\text{P}_{12}</math> by resonant soft x-ray diffraction</b>	<b>54</b>
5.1	Introduction . . . . .	54
5.2	Experimental . . . . .	56
5.3	Results . . . . .	57
5.4	Discussion . . . . .	62
5.5	Conclusion . . . . .	67
<b>6</b>	<b>Summary and outlook</b>	<b>69</b>
<b>A</b>	<b>Reliability factors of Rietveld refinement</b>	<b>72</b>
	<b>Bibliography</b>	<b>73</b>

# List of Figures

1.1	Schematic diagram of a) coupling ferroelectricity, ferromagnetism and ferroelasticity to form a multiferroic (redrawn after [2]) and b) a conceptual four-state multiferroic memory device. . . . .	2
1.2	Schematic showing different microscopic mechanisms of ferroelectricity in proper multiferroics [6] (see text). . . . .	5
1.3	Schematic show of mechanisms for improper multiferroics. Top: the KNB model [8]; bottom: the inverse DM model [9]. $\mathbf{P}_{el}$ and $\mathbf{P}_{ion}$ refers to FE polarization induced by electronic and ionic displacement contribution respectively. . . . .	6
1.4	Schematic showing A) charge, B) orbital and C) spin degree of freedom [19]. . . . .	8
2.1	Geometry of X-ray diffraction in real lattices (top) and in reciprocal lattices (bottom). Figure taken from [28] and [30] respectively. . . . .	14
2.2	Total electron yield mode for soft X-ray absorption spectroscopy. . . . .	19
2.3	Schematic illustration of the resonant X-ray diffraction (after [34]). Note that the first two processes corresponding to absorption are in essence the basic principles of X-ray absorption spectroscopy. . . . .	21
2.4	The scattering geometry of resonant X-ray diffraction. . . . .	23
2.5	Dependence of inverse susceptibility on temperature for three typical types of magnetic materials [36]. . . . .	25
3.1	Crystal structure of the layered perovskite oxide $\text{La}_2\text{Ti}_2\text{O}_7$ with space group $\text{P2}_1$ in different views created by VESTA program [39]. Ti atoms (represented by blue balls) are in an octahedral environment of oxygen (red dots). . . . .	29
3.2	XRD pattern of $\text{La}_2\text{Ti}_{2-x}\text{V}_x\text{O}_7$ ( $x = 0.0625, 0.125$ and $0.25$ ) prepared by annealing in air. The peaks marked by asterisks are identified as the $\text{LaVO}_4$ phase. . . . .	30
3.3	XRD pattern of $\text{La}_2\text{Ti}_{2-x}\text{V}_x\text{O}_7$ ( $x = 0.125$ ) prepared by a) air annealing and b) water quenching. The peaks marked by asterisks are identified as a $\text{LaVO}_4$ phase. The insets show the magnified patterns with $2\theta$ of $20 \sim 27^\circ$ . . . . .	31

3.4	XRD pattern of $\text{La}_2\text{Ti}_{2-x}\text{V}_x\text{O}_7$ ( $x = 0.0625, 0.125$ and $0.25$ ) prepared by water quenching. A trace amount of $\text{LaVO}_3$ and $\text{LaVO}_4$ impurities are found for $x = 0.25$ sample, marked by a plus mark and an asterisk mark respectively. The $x = 0$ sample is prepared by air annealing. . . . .	32
3.5	The refinement of XRD data of $\text{La}_2\text{Ti}_{2-x}\text{V}_x\text{O}_7$ ( $x = 0, 0.0625$ and $0.125$ ). The red circles are the observed data while the black solid line is the square-least fitted line; the green ticks shown below are the Bragg positions; the blue line at the bottom is the difference between the observed and calculated data. . . . .	33
3.6	The lattice parameters of $\text{La}_2\text{Ti}_{2-x}\text{V}_x\text{O}_7$ ( $x = 0, 0.0625$ and $0.125$ ) obtained from the refinement. The error bars are created from the estimated standard deviations of the refined parameters; for $a$ , $b$ and $V$ they are smaller than the size of the plotting symbols. . . . .	34
3.7	M-H curves for $\text{La}_2\text{Ti}_{2-x}\text{V}_x\text{O}_7$ ( $x = 0, 0.0625$ and $0.125$ , from bottom to top). . . . .	36
3.8	Magnetic susceptibility $\chi$ measured at 500 Oe as a function of temperature for $\text{La}_2\text{Ti}_{2-x}\text{V}_x\text{O}_7$ ( $x = 0, 0.0625$ and $0.125$ ). The inset shows the temperature evolution of $1/\chi$ for the doped samples and the Curie-weiss fitting. The temperature dependence of $1/\chi$ for the pure sample is not included here, which consists of a large diamagnetic component. . . . .	37
4.1	The crystal structure of $\text{CaMn}_7\text{O}_{12}$ (Top: $\text{Im}\bar{3}$ ; bottom: $\text{R}\bar{3}$ ) created using the VESTA program [39]. Mn1 denotes $\text{Mn}^{3+}$ of C in an $\text{AC}_3\text{B}_4\text{O}_{12}$ formula surrounded by four oxygen atoms forming a plane; Mn2 (Mn3) denotes $\text{Mn}^{3+}$ ( $\text{Mn}^{4+}$ ) of B which is in an octahedral environment of oxygen. . . . .	40
4.2	SEM image of the sample before (panels a) and b)) and after (panels c) and d)) purification. . . . .	43
4.3	Results of the Rietveld refinement of the XRD pattern of $\text{CaMn}_7\text{O}_{12}$ measure at room temperature. The red points denote measured data; the black line is the calculated pattern. The top tickmarks represent the Bragg peaks for $\text{CaMn}_7\text{O}_{12}$ while the below ones for the impurity phase $\text{CaMn}_2\text{O}_4$ . The difference curve is shown as a blue line at the bottom. The inset shows the fit of $\text{CaMn}_2\text{O}_4$ peaks. . . . .	45
4.4	The experimental set-up for oxygen 18 substitution. . . . .	46
4.5	XRD pattern of $\text{CaMn}_7\text{O}_{12}$ before and after oxygen isotope substitution. . . . .	47
4.6	Raman spectra of $\text{CaMn}_7\text{O}_{12}$ before and after oxygen isotope substitution. Two dashed vertical lines at the centre of each peak are also drawn as a guide to eyes. The step seen to the left of the main peak of $\text{CaMn}_7^{16}\text{O}_{12}$ are also assigned to oxygen modes but they are not well resolved (see text). . . . .	48

4.7	Temperature evolution of magnetization of $\text{CaMn}_7^{16}\text{O}_{12}$ and $\text{CaMn}_7^{18}\text{O}_{12}$ . The insets show the magnetic transition points. . . . .	50
4.8	Compare the temperature evolution of magnetization of $\text{CaMn}_7^{16}\text{O}_{12}$ and $\text{CaMn}_7^{18}\text{O}_{12}$ taken in field cooled mode. . . . .	51
4.9	Hysteresis loops of $\text{CaMn}_7^{16}\text{O}_{12}$ and $\text{CaMn}_7^{18}\text{O}_{12}$ . . . . .	52
5.1	(a) The crystal structure of $\text{PrRu}_4\text{P}_{12}$ in the $\text{Im}\bar{3}$ phase at room temperature created by VESTA program [39], based on the atomic positional parameters reported in [84]. A Pr atom (denoted as a black ball) is in an icosahedron environment of P atoms (omitted for clarity) and a cubic environment of Ru atoms (denoted as purple balls); Note that below $T_{MI}$ , the structure changes to $\text{Pm}\bar{3}$ in which the Ru cube in the centre expands while the Ru cubes surrounding shrink, or vice versa, forming a CDW state and leaving two distinct Pr sites. (b) Lower panel: $\text{PrRu}_4\text{P}_{12}$ single crystal sample mounted on the stage by silver paste; Upper panel: the scattering geometry. . . . .	56
5.2	The (100) reflection (purple dots) recorded at 10 K for $\sigma$ polarization and selected energies a) 907 eV, b) 924 eV, c) 927 eV, d) 944 eV, e) 947 eV and f) 967 eV, and their Lorentzian fittings (red lines). . . . .	58
5.3	The integrated intensity of (100) diffraction after absorption correction as a function of energy. The inset is a magnified figure showing the detailed structure around the $M_4$ edge, near 947 eV. The arrows denote the energies selected for observations with focused beams. . . . .	59
5.4	The square root of integrated intensity of (100) diffraction normalized at 10 K as a function of temperature. The Ru displacements taken from [86, 87] and interpolated to the measured temperature points are also plotted for a comparison. Two energies marked with asterisks are for unfocused beams while the others are for focused beams. . . . .	60
5.5	$I_\sigma/I_\pi$ measured with a focused beam at different azimuthal angles. The theoretically calculated $I_\sigma/I_\pi$ based on the charge order is shown in red line for a comparison. . . . .	61
5.6	The Pr $M_{4,5}$ edge absorption spectra of $\text{PrRu}_4\text{P}_{12}$ measured at different temperatures and plotted with a) the spectrum vertically shifted to each other by an almost fixed value and b) Pr $M_5$ edge and $M_4$ edge separately normalized to 1 after subtracting a linear background from the respective spectrum in a). . . . .	63
5.7	The integrated intensity of (100) diffraction as a function of energy for $\sigma$ polarization plotted together with the calculated curves assuming different displacement of Pr. . . . .	64

5.8	The theoretical Cromer-Lieberman anomalous scattering factors of Pr. . . . .	65
5.9	The integrated intensity of (100) diffraction as a function of energy for $\sigma$ polarization plotted together with the calculated curve based on charge disproportionation of $\text{Pr}^{3+}$ . . . . .	67

# List of Tables

2.1	Absorption edges and the corresponding core levels. . . . .	18
3.1	Reliability factors of refinement of $\text{La}_2\text{Ti}_{2-x}\text{V}_x\text{O}_7$ ( $x = 0, 0.0625$ and $0.125$ ). . . . .	35
4.1	Chemical composition of $\text{CaMn}_7\text{O}_{12}$ measured by EDX. . . . .	43
4.2	Summary of refined crystallographic information for $\text{CaMn}_7\text{O}_{12}$ . . . . .	45
A.1	. . . . .	72

# Declaration

I hereby declare that this submission is my own work and to the best of my knowledge it contains no materials previously published or written by another person, or substantial proportions of material which have been accepted for the award of any other degree or diploma at UNSW or any other educational institution, except where due acknowledgement is made in the thesis. Any contribution made to the research by others, with whom I have worked at UNSW or elsewhere, is explicitly acknowledged in the thesis. I also declare that the intellectual content of this thesis is the product of my own work, except to the extent that assistance from others in the project's design and conception or in style, presentation and linguistic expression is acknowledged.

Signed:

---

Date:

---

# Acknowledgements

This thesis is not possible without the aid from the following people and institutions.

I would like to thank Dr Annemieke Mulders, Dr Wayne Hutchison and Assoc. Prof. Glen Stewart for their supervision during the past two and a half years. I heartily acknowledge that Dr Wayne Hutchison and Dr Annemieke Mulders co-proposed PrRu<sub>4</sub>P<sub>12</sub> sub-topic and measured the Resonant Soft X-ray Diffraction data that I could work on. Dr Annemieke Mulders introduced me to the field of scattering science using large facilities. I appreciate she encouraged me to attend the Summer School on Condensed Matter Research in Switzerland and Powder Diffraction Data Analysis Workshop in Australia as well as many other academic conferences. I benefit a lot from these academic activities. She proposed the multiferroic sub-topics that I could work and write on in this thesis, and provided insightful suggestions for sample preparation and/or data analysis; I would like to express my sincere gratitude for these and her willingness to comment on my work on PrRu<sub>4</sub>P<sub>12</sub> after her leaving our campus. Dr Wayne Hutchison provided numerous practical and helpful suggestions on experiments concerning three material systems, particularly on that of La<sub>2</sub>Ti<sub>2-x</sub>V<sub>x</sub>O<sub>7</sub> and CaMn<sub>7</sub>O<sub>12</sub>; He also measured the magnetic properties of La<sub>2</sub>Ti<sub>2-x</sub>V<sub>x</sub>O<sub>7</sub>; Without his critical readings and comments, this thesis would never come out smoothly; I sincerely appreciate these kind supports. Prof. Glen Stewart offered me many opportunities to bother him whenever I have stupid questions. I am really grateful for his great patience and warm encouragements.

Thanks must also go to Dr Narendrakumar Narayanan, Dr Vernon Edge, Prof Katsuhiko Nishimura, Professor Hoe Tan and Dr Fan Wang for their helps in the multiferroic sub-topics. Dr Narendrakumar Narayanan taught me some critical experimental skills in both of these sub-topics, such as solid state reaction sample preparation and Rietveld refinement by using *Fullprof* software package, etc., and also provided many experimental helps and suggestions; Dr Vernon Edge helped with building the oxygen exchange system that I could use for my CaMn<sub>7</sub>O<sub>12</sub> sub-topic and sealing the quartz tube for La<sub>2</sub>Ti<sub>2-x</sub>V<sub>x</sub>O<sub>7</sub> samples; Prof Katsuhiko Nishimura from University of Toyama measured the magnetic properties of CaMn<sub>7</sub>O<sub>12</sub> by using

their SQUID magnetometer; Professor Hoe Tan approved me to access to the Micro-Raman System at Australian National University to characterise  $\text{CaMn}_7\text{O}_{12}$  and Dr Fan Wang helped with the measurements.

I would also like to thank our international collaborators Prof Hitoshi Sugawara, Dr Urs Staub, Dr Marios Garganourakis, Dr Yoshikazu Tanaka, Dr Ashish Chainani and Dr Masaki Oura for their supports for the  $\text{PrRu}_4\text{P}_{12}$  sub-topic. More concretely, Prof Hitoshi Sugawara supplied high quality  $\text{PrRu}_4\text{P}_{12}$  single crystals which are the footstone of this project; Dr Urs Staub and Dr Marios Garganourakis offered us the beam time of resonant soft x-ray diffraction in Swiss Light Source, Paul Scherrer Institute and provided experimental supports; Dr Yoshikazu Tanaka, Dr Ashish Chainani and Dr Masaki Oura from Spring-8 accompanied me several long nights to collect the X-ray Absorption Near Edge Structure data. I also thank them for their suggestions on the latter data analysis and interpretation.

I would also like to thank UNSW Canberra for offering me the Research Training Scholarship for this research course study and the student research funding for purchasing chemicals, combustion boats and crucibles used in multiferroic sub-topics and student version MATLAB software for the  $\text{PrRu}_4\text{P}_{12}$  sub-topic; Travel funding for the experiments of  $\text{PrRu}_4\text{P}_{12}$  sub-topic in Paul Scherrer Institute and Spring-8 provided by the International Synchrotron Access Program managed by the Australian Synchrotron and funded by the Australian Government is also acknowledged.

Special thanks are due to my wife Mingfang Yu for accompanying me almost one year in Australia and supporting me to pursue a research career all these years.

# Abstract

In this thesis, electric and magnetic properties of exotic strongly correlated electron systems are explored via studies of  $\text{La}_2\text{Ti}_{2-x}\text{V}_x\text{O}_7$ ,  $\text{CaMn}_7\text{O}_{12}$  and  $\text{PrRu}_4\text{P}_{12}$ .

In order to form a proper multiferroic, single phase  $\text{La}_2\text{Ti}_{2-x}\text{V}_x\text{O}_7$  ( $x = 0, 0.0625, 0.125$ ) was synthesised successfully by a vacuum annealing plus water quenching method. The magnetic properties of the doped samples were studied and compared with that of undoped  $\text{La}_2\text{Ti}_2\text{O}_7$ . The results reveal a primary paramagnetic-like behaviour and a weak magnetic order rather than the ferromagnetic order for the doped samples, which is explained by a vanadium monomer phase formed at the high synthesis temperature. To obtain a single phase with ferromagnetic order, other novel synthesis method with a lower synthesis temperature has to be used.

The multiferroic  $\text{CaMn}_7\text{O}_{12}$  was synthesised successfully by a flux method and isotope substitution effect on magnetic properties was studied. The  $^{18}\text{O}$  concentration was estimated to be 61 at.% by Raman Spectroscopy and 64 at.% from the mass difference. Smaller magnetization was observed for  $50 < T < 120$  K wherein two characteristic magnetic transitions occur and ferroelectric polarization develops. This can be considered as direct evidence that oxygen affects the magnetic properties and the ferroelectric polarization. However different divergence temperatures were also observed. Two additional experiments are suggested that would further clarify these changes in magnetization with oxygen mass.

To investigate the order parameter of Pr below  $T_{MI} = 62.3$  K in  $\text{PrRu}_4\text{P}_{12}$  temperature dependent resonant soft x-ray diffraction in combination with x-ray absorption spectroscopy were performed at the Pr  $M_{4,5}$  edges. A resonance enhancement of the (100) superlattice reflection signalling the order parameter of the Pr 4f shells was observed below  $T_{MI}$ , with a steady increase with decreasing temperature. The experimental spectra and subsequent analysis rule out the existence of magnetic and/or orbital order as well as any Pr lattice displacement. The order parameter below  $T_{MI}$

is likely due to charge disproportionation. Our results also indicate that a synergistic coupling of Pr 4f - Ru states plays an important role in the metal-insulator transition associated with charge density wave state formation.

*To nature itself...*

# Chapter 1

## Introduction

In recent years, strongly correlated electron systems have attracted much research interest in condensed matter physics. In these systems, electrons strongly interact with each other, which is completely different from the classic free electron picture. Different electronic orders, including charge order, orbital order, magnetic order, charge density wave, etc, may compete or even coexist in the systems because of such strong interactions. This leads to a variety of novel physical phenomena which may find potential applications yet challenge our understanding of condensed matter, for example high temperature superconductivity, colossal magnetoresistance, multiferroicity and metal-insulator (MI) transitions. The latter two phenomena are the subject of this thesis. Many specific anomalous strongly correlated electron systems exhibit novel multiferroicity or subtle MI transitions, which are the issues to be addressed in this thesis.

### 1.1 Multiferroicity

Functional materials with one of the ferroic properties ferromagnetism, ferroelectricity and ferroelasticity are essential for modern technologies. In the so-called multiferroic materials, more than one of the above three properties exist simultaneously [1]. Among them, those with ferromagnetism and ferroelectricity attract more attention and are the most studied thus far since they can find potential applications in spintronics technology in an ever-expanding information industry. This type of multiferroic is the one

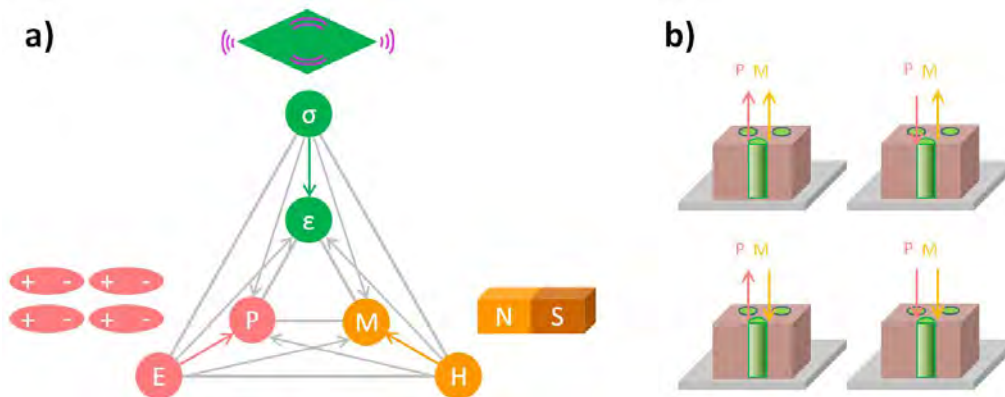


Figure 1.1: Schematic diagram of a) coupling ferroelectricity, ferromagnetism and ferroelasticity to form a multiferroic (redrawn after [2]) and b) a conceptual four-state multiferroic memory device.

of interests in this thesis. The coexistence of both charge and spin components can be exploited and one property can be used to drive the other, i.e., magnetic field can change the polarization state or vice versa. They can form the basis for four-state memory and for example using a multiferroic material in a one Megabyte memory stick could have its capacity increased to one Terabyte(see Fig 1.1).

Research into multiferroic materials dates back to as early as 1894 when Curie tried to predict the possibility of an intrinsic magnetoelectric (ME) effect (i.e., the coupling of electric and magnetic fields) in some crystals [3] and to the 1960's when this effect was first successfully observed in  $\text{Cr}_2\text{O}_3$  [4]. The ME effect can be explained by Landau theory. In Landau theory, the free energy of the ME effect can be expanded as [5] ,

$$\begin{aligned}
 F(E, H) = & F_0 - P_i^s E_i - M_i^s H_i - \frac{1}{2} \epsilon_{0ij} E_i E_j - \frac{1}{2} \mu_{0ij} H_i H_j \\
 & - \alpha_{ij} E_i H_j - \frac{1}{2} \beta_{ijk} E_i H_j H_k - \frac{1}{2} \gamma_{ijk} H_i E_j E_k - \dots ,
 \end{aligned} \tag{1.1}$$

where subscripts  $i, j$  and  $k$  denote the components of a variable in a spatial coordinate;  $F_0$  is the free energy;  $E$  means the electric field and  $H$  the magnetic field;  $P$  and  $M$  with a subscript  $s$  refers to a spontaneous electric polarization and magnetization respectively;  $\epsilon_0$  and  $\mu_0$  stand for the dielectric and magnetic susceptibilities of vacuum,  $\epsilon_{ij}$  and  $\mu_{ij}$  being the second-order tensors of dielectric and magnetic susceptibilities,  $\beta_{ijk}$  and  $\gamma_{ijk}$  the third-order tensor coefficients; and  $\alpha_{ij}$  are the components of tensor  $\alpha$  describing the linear magnetoelectric effect and corresponds to the

induction of polarization by a magnetic field or a magnetization by an electric field; and the apostrophe consists of the linear magnetoelectric effects denoted by tensors  $\beta$  and  $\gamma$ . Hence the electric polarization can be written as,

$$\begin{aligned} P_i(E, H) &= -\frac{\partial F}{\partial E_i} \\ &= P_i^s + \epsilon_0 \epsilon_{ij} E_j + \alpha_{ij} H_j + \frac{1}{2} \beta_{ijk} H_j H_k + \gamma_{ijk} H_i E_j + \dots, \end{aligned} \quad (1.2)$$

and the magnetization is,

$$\begin{aligned} M_i(E, H) &= -\frac{\partial F}{\partial H_i} \\ &= M_i^s + \mu_0 \mu_{ij} H_j + \alpha_{ij} E_j + \beta_{ijk} H_j E_i + \frac{1}{2} \gamma_{ijk} E_j E_k + \dots, \end{aligned} \quad (1.3)$$

Since the first observation, hundreds of material systems with the ME effect have been discovered. Based on these observations, to enhance the magnetoelectric response, a more novel and effective coupling, the one between ferromagnetism and ferroelectricity was proposed to exist in one material in the absence of external magnetic and electric fields. These materials were named multiferroics by Schmid [1] in 1994 and to date due to their multifunctionality yet rarity, considerable efforts have been devoted to synthesizing and investigating them.

### 1.1.1 Incompatibility between ferroelectricity and magnetism

The rarity of a multiferroic lies in the fact that ferroelectricity and magnetism are repulsive in nature in a material system. Considering symmetry, ferroelectricity requires the broken spatial inverse symmetry, i.e., as a polar vector, the electric field  $\mathbf{E}$  and polarization  $\mathbf{P}$  change sign when space  $\mathbf{r}$  is inversed to  $-\mathbf{r}$ ; however it remains invariant in a time inversion operation. This is contrary to the situation in spin order for which the magnetic field  $\mathbf{H}$  and magnetization  $\mathbf{M}$  as axial vectors change sign under time inversion but are invariant under a space inversion operation.

### 1.1.2 Routes to multiferroicity: proper multiferroics

Magnetism of a material is generally generated from the exchange interactions between spins of electrons which can be usually found in partially filled d or f shells of transition-metal or rare earth ions. However ferroelectricity can have a variety of origins. Depending on the origin of ferroelectricity, a multiferroic material can fall in one of these two categories: proper or improper multiferroics. In the first category, the magnetism and ferroelectricity have different origins and are almost independent of each other even though they have a certain degree of interplay. In the second category, ferroelectricity is a result of magnetism and a strong coupling between the two usually exists.

In a proper multiferroic, ferroelectricity has nothing to do with magnetism in most cases and the coupling between these two orders is also weak. Various microscopic mechanisms for the ferroelectric moment have been proposed and made use of to synthesize this category of multiferroics.

Doping the magnetic perovskite oxides with ferroelectric  $d^0$  ions is one scenario. In this case ferroelectric ions (shown in green points Fig 1.2 a)) can displace from the centre to form strong covalent bonds with the neighbouring oxygens and thus generate ferroelectric (FE) polarization which can coexist with magnetism originating from  $d^n$  ions (shown as red spins in Fig 1.2 a)).

Lone pairs (usually found as two outer 6s electrons of Bi and Pb) that do not form any bonds can be ordered in one direction thus give rise to FE polarization (see Fig 1.2 b)).

The charge ordering scenario is presented in Fig 1.2 c). In a chain with -X-O-X- structure wherein X stands for a positively charged metal ion and O is oxygen, after charge ordering, the bond X-O (shown as a bar) and O-X (shown as the gap between bars) are inequivalent in dimension and can lead to ferroelectricity.

Geometric ferroelectricity as its name indicates is realized by geometric factors, such as a distortion or tilting in structure, usually to achieve a closer packing and an energetically more stable state. This mechanism is seen in  $\text{YMnO}_3$  [7] (see Fig 1.2 d)).

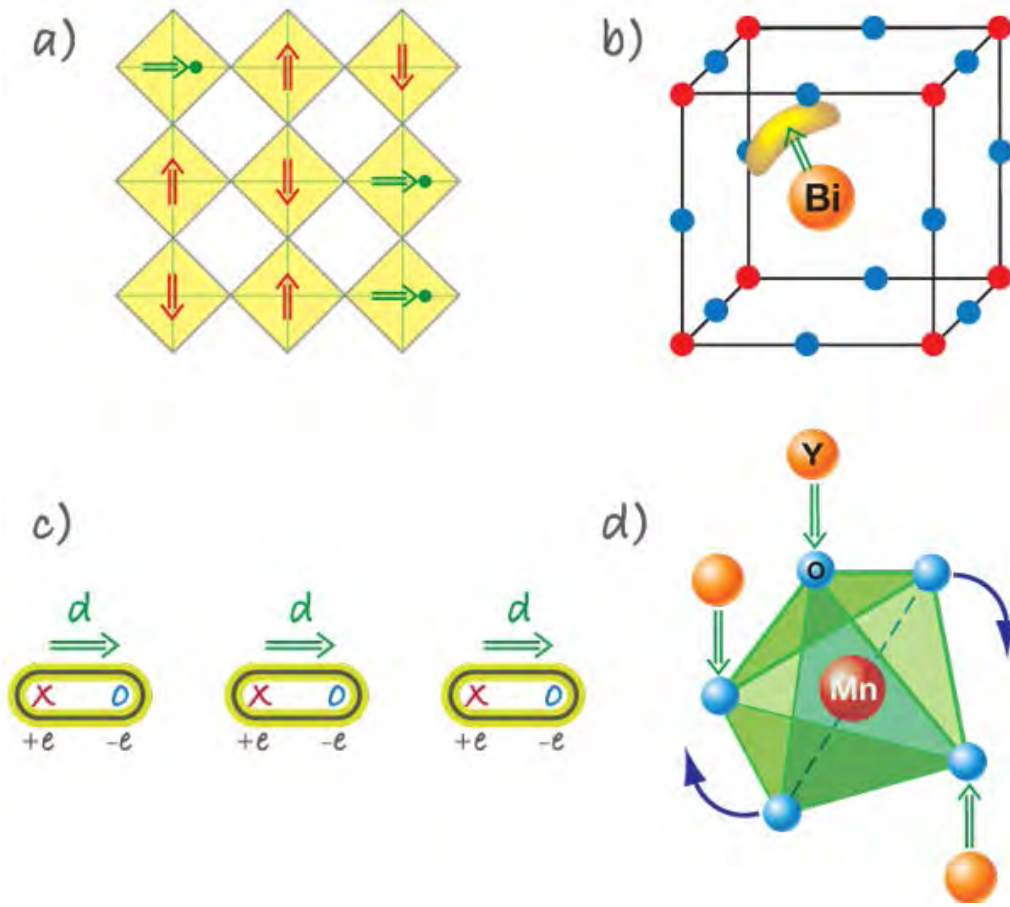


Figure 1.2: Schematic showing different microscopic mechanisms of ferroelectricity in proper multiferroics [6] (see text).

$\text{La}_2\text{Ti}_2\text{O}_7$  is a novel geometric ferroic whose ferroelectric polarization arises spontaneously from the so called antiferrodistortive distortions and persists to a temperature as high as 1770 K. Exploration of routes to multiferroicity based on this material system is of scientific interest as well as of significance to applications. A study of magnetic vanadium ion doped  $\text{La}_2\text{Ti}_2\text{O}_7$  is given in Chapter 3.

### 1.1.3 Routes to multiferroicity: improper multiferroics

Compared with proper multiferroics, improper multiferroics are more complex and rare because of the existence of strong coupling between spin and charge orders. Despite that various efforts have been spent on the study of improper multiferroics, at the moment, the theory is still a controversial

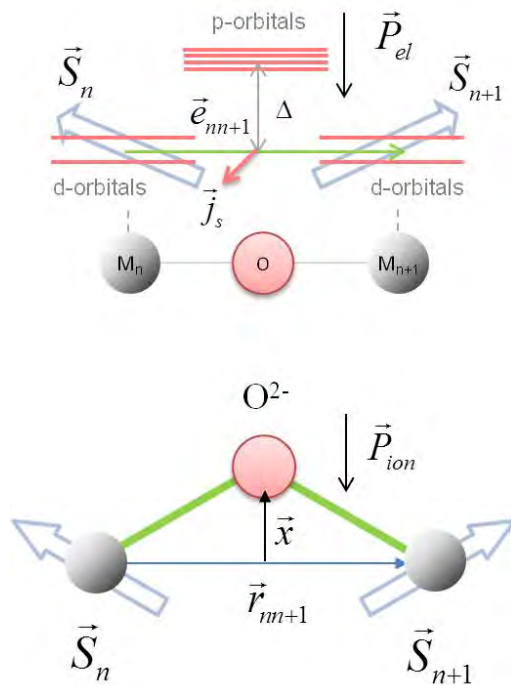


Figure 1.3: Schematic show of mechanisms for improper multiferroics. Top: the KNB model [8]; bottom: the inverse DM model [9].  $\mathbf{P}_{el}$  and  $\mathbf{P}_{ion}$  refers to FE polarization induced by electronic and ionic displacement contribution respectively.

issue. Many physical pictures have been proposed among which, the scenario of inherent electronic structure and ionic displacement are the most typical two ones.

The inherent electronic structure scenario was early reported as a spin current model, developed by Katsura, Nagaosa and Balatsky and known as KNB model [8]. For a three-atom model (see Fig 1.3) in which two transition metal ions  $M_n$  and  $M_{n+1}$  are bonded through an oxygen atom  $O$ , from the calculation of the electronic Hamiltonian taking into account the spin-orbital interaction, ferroelectric (FE) polarization  $\mathbf{P}$  is found to be correlated with spin supercurrent  $\mathbf{j}_s$  generated in noncollinear spin structures (such as the spiral state) as below,

$$\mathbf{P} \propto \mathbf{e}_{nn+1} \times \mathbf{j}_s \propto \mathbf{e}_{nn+1} \times (\mathbf{S}_n \times \mathbf{S}_{n+1}), \quad (1.4)$$

where  $\mathbf{e}_{nn+1}$  is the unit vector connecting  $M_n$  and  $M_{n+1}$ ;  $\mathbf{S}_n$  and  $\mathbf{S}_{n+1}$  refers to the spin of  $M_n$  and  $M_{n+1}$ . The above equation makes the estimation of not only the direction but also the order of magnitude of FE polarization

possible in a spiral magnet. According to the authors' estimation, the order of magnitude estimated for a cubic system with the lattice constant  $a = 5 \text{ \AA}$  is comparable to that of  $(\text{Ga,Fe})\text{O}_3$  at  $H = 10 \text{ T}$ . The FE polarization generated by spin current in this model depends on the detailed electronic level structure as well as the band structure for a particular material system. Current theoretical studies also indicate a contribution from valence electrons to FE polarization [10, 11] and a purely electronic contribution was experimentally observed in the absence of lattice distortion in  $\text{YMn}_2\text{O}_5$  by soft x-ray resonant scattering [12].

In the scenario of ionic displacement, however the lattice distortion, usually driven by magnetic phase transitions for a lower of energy, is essential to the generation of FE polarization [6, 13–15]. It is well known that to optimize the energy of the system, the conventional Dzyaloshinskii-Moriya (DM) interaction on the non-centrosymmetric bond leads to a canting of the interacting spins and a weak ferromagnetism [16]; then one would assume an inverse DM effect, that is, the canting of the existing spins (e.g., the spiral magnetic structure) for some reasons might cause displacement of the ion (usually O) bonding the spin sites in order to generate a new DM vector. The local FE polarization can therefore be resulted with a direction opposite to the ionic displacement. Sergieko et al [9] proposed this inverse DM model to explain the coexistence and strong coupling between the FE polarization and incommensurate magnetism and found that in the cubic perovskite manganites the portion of Hamiltonian depending on the displacement of O,

$$\delta H = \sum \mathbf{D}^x(\delta \mathbf{r}_n) \cdot [\mathbf{S}_n \times \mathbf{S}_{n+1}] + H_{el} \quad (1.5)$$

can be minimized by a nonzero oxygen displacement  $\delta z_n$  along z axis,

$$\delta z_n = \frac{\gamma}{\kappa} S_0^x S_0^z \sin \theta \sin(\alpha_x - \alpha_z) \quad (1.6)$$

while  $\delta x_n$  in x axis and  $\delta y_n$  in y axis are both zero, where  $\delta \mathbf{r}_n = (\delta \mathbf{x}_n, \delta \mathbf{y}_n, \delta \mathbf{z}_n)$  denotes the displacement related to incommensurate structure;  $\mathbf{D}^x(\delta \mathbf{r})_n$  is the DM vector depending on  $\delta \mathbf{r}_n$ ;  $\mathbf{S}_n$  and  $\mathbf{S}_{n+1}$  is the spin of two neighbouring Mn atoms;  $H_{el}$  is the elastic energy;  $\kappa$  is stiffness;  $S_0^x = S_0^y \approx$

$S_0^z = 1.4$ ,  $\theta = 0.28\pi$ . The value of  $\gamma$  estimated from equation (1.6) agrees well with the previously reported experimental estimations, indicating that this model seems valid for perovskite manganites.

To clarify this, in Chapter 4 a novel oxygen 18 substitution experiment is performed on the interesting improper multiferroic  $\text{CaMn}_7\text{O}_{12}$  and the effect of oxygen 18 substitution on magnetism is studied.

## 1.2 Metal-insulator transitions and electronic orderings

The metal-insulator (MI) transition, a transition from a conductive metal to an insulator, has been theoretically and experimentally investigated for over 80 years. Generally speaking, there are five typical types of transitions that can be described in terms of underlying physics which is closely related to strong couplings among charge, lattice, orbital, and/or spin degrees of freedom (see Fig 1.4), according to [17, 18]. In a real material system, however these transitions are not mutually exclusive and the observed MI transition is not necessarily dominated by one interaction alone but rather by a combination effect. Even though a single interaction in some case may drive the transition, its nature can be (and most often is) strongly influenced by the others.

The Wilson transition originates from interaction between electrons and the periodic potential of the ions giving rise to an energy gap between the lowest conduction band and the highest valence band. For some divalent

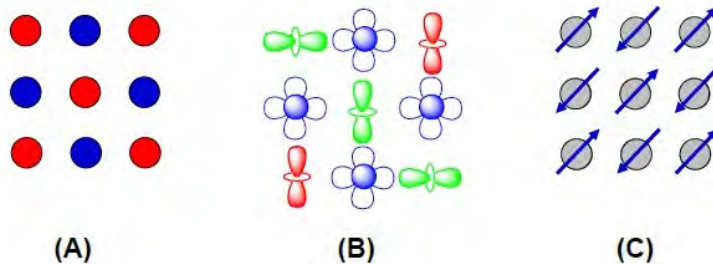


Figure 1.4: Schematic showing A) charge, B) orbital and C) spin degree of freedom [19].

semimetals, the energy gap is quite small which may be opened by external field to transform to a Wilson insulator. An example is Bi [17, 20]; it shows such a MI transition under pressure. The pressure can increase the mixing of the 4f and 5d shells and eventually result in the opening of a hybridization gap.

The Peierls transition arises from the interaction between electrons and the lattice. For metals with a partially occupied band, doubling of lattice constant due to crystal structural change can result in splitting of the band. If Brillouin zone boundary shifts to the Fermi surface, then the band may split into a filled one and an empty one and Peierls transition therefore takes place. The insulating phase is termed a Peierls insulator, wherein a (commensurate) charge-density wave (CDW) of the electrons, a kind of charge ordering is yielded finally. This transition is seen in low-dimensional electronic crystals, for example, NbSe<sub>3</sub> [21].

The Verwey transition is another MI transition which is associated uniquely with long range charge ordering. At low temperatures, because of strong interaction, the electrons are able to localize and form an charge ordered state. Due to its localized nature this phase is insulating. While at high temperatures the localized and ordered state is lost, the electrons become itinerant and therefore show a conducting state. It is usually observed in narrow band solids such as transition metal oxides or organic conductors in which the number of electrons is smaller than the number of equivalent lattice sites. The typical material is the famous magnetite (Fe<sub>3</sub>O<sub>4</sub>). It was found to show a first order resistivity transition at 120K which is accompanied by a charge ordering [22, 23].

The Anderson transition is due to the interaction of free, independent electrons with randomly distributed lattice defects (i.e., disorder). The disorder may generate particle localization, thus electrons in a disordered solid system possess localized and extended states, wherein extended electrons are known to contribute to conductivity while localized electrons contribute to insulating state. Since net conductivity of a material is mainly from the contribution of electrons in vicinity to the Fermi surface, location of the Fermi surface in extended state region or localized state region may lead to a metal or insulator behaviour. Therefore any factors that can move the Fermi surface from an extended state region to a localized state region

may cause the MI transition. It has been proved that, variation of electron concentration, a change of strength of the impurity (disorder) potential, and tuning the effective bandwidth with the aid of external magnetic field [17] offers routes to Anderson insulator.

The Mott transition is the result of the electron–electron interaction. There are several types of this transition, namely Mott-Hubbard transition and Mott-Heisenberg transition [17]. In a picture proposed by Mott [24], when atoms are brought close to form a crystal system, the energy levels expands to energy bands which consist of upper Hubbard bands with bandwidth  $W_1$  and lower Hubbard bands with bandwidth  $W_2$ . The bandwidth can be narrow and an energy gap is formed if the distance of the atoms is large wherein overlap in the neighbouring atomic wave functions is small and

$$\frac{W_1 + W_2}{2} \approx W \ll U, \quad (1.7)$$

where  $U$ , the intra-atomic energy, is called Hubbard energy equaling to ionization energy minus electron affinity. In this case if the lower Hubbard band is filled while the upper Hubbard band is empty, then the system is an insulator. Upon reducing the distance between atoms, the overlap in the neighbouring atomic wave functions increases and the combined bandwidth  $W_1 + W_2$  increases accordingly and two bands eventually overlap without a gap in between. If  $W \gg U$  then the system is a metal. When  $W \approx U$  a MI transition is expected and the insulating phase is called a Mott-Hubbard insulator. Obviously, in a Mott-Hubbard insulator, the ordering of magnetic moments is not considered and the local magnetic moments do not display long-range order (i.e., it is a paramagnetic insulator). However the possibility of an ordering of magnetic moments exists and this is the case for a Mott-Heisenberg insulator. An antiferromagnetic coupling  $J \sim t_{ij}^2/U$  (where  $t_{ij}$  is tunneling element describing the inter-orbital hybridization) exists between the spin-1/2 electrons on neighbouring lattice. For  $U \gg W$  and half band-filling, the system is in the Mott-Hubbard insulating state until the temperature reaches near or below that of the exchange coupling where the spin energy scale is not negligible. The local moments are then long range ordered and the system turns into a Mott-Heisenberg insulator. For  $U \ll W$ , the Hubbard gap is gone however pre-formed magnetic moments arise due to the correlations for all  $U > 0$ . The moments may then

ordered at the Néel temperature, and a thermodynamic phase transition from a paramagnetic (correlated) metallic state into an antiferromagnetic insulating state is seen [17].

Yet there are many anomalous material systems for which the MI transitions are of orbital ordering origin and cannot be explained in terms of any one or any combinations of transitions listed above. To name but a few, in  $V_2O_3$  long-range order of vanadium 3d orbitals which was detected by resonant x-ray scattering appears at a critical temperature where the MI transition as well as magnetic transition takes place [25]; the MI transition of  $La_{1-x}Ca_xMnO_3$  ( $x \sim 0.2$ ) is found to be driven by d-type orbital ordering [26];  $La_{0.88}Sr_{0.12}MnO_3$  shows a phase transition at 145 K from a ferromagnetic metal to a novel ferromagnetic insulator. The order parameter of the transition was directly identified as the orbital degree of freedom by resonant x-ray scattering [27].

Clearly the nature of the ordering of electrons, i.e., charge, orbital, and/or spin ordering, plays a role in a MI transition and holds the key to revealing the origin of the transition. It is therefore of great significance to know the concrete nature of the electronic order. An individual electronic order is easily probed by a traditional technique. For instance, magnetic order can be revealed by specific heat or bulk magnetic measurement; and charge order which forms a superlattice can be observed via an XRD experiment. While all of these three electronic orders can be conveniently checked and clearly identified by resonant x-ray scattering. This novel technique is employed in Chapter 5 to study the nature of order of 4f electrons driving the MI transitions in the third material system of interest the filled skutterudite  $PrRu_4P_{12}$ .

# Chapter 2

## Experimental principles<sup>1</sup>

In this thesis, a variety of experimental techniques, such as traditional X-ray diffraction, X-ray absorption spectroscopy, resonant X-ray diffraction, scanning electron microscope and magnetization measurements are employed to study the three material systems  $\text{La}_2\text{Ti}_{2-x}\text{V}_x\text{O}_7$ ,  $\text{CaMn}_7\text{O}_{12}$  and  $\text{PrRu}_4\text{P}_{12}$ . The principles of these techniques are given in this chapter.

### 2.1 X-ray diffraction

X-rays, neutrons and electrons are the main beam sources used in a diffraction experiment to determine the crystal structure of materials. Among them, X-rays are particularly prevalent and the light sources are readily available in both laboratories and synchrotrons. X-rays are well suited for the crystal structure determination in that they are able to "react" with the electrons of atoms in the materials of interest. More concretely, in a so-called elastic scattering or diffraction, secondary X-rays with the same energy and phase are radiated when the electrons of atoms are accelerated by the electric field of incident X-rays [28], and flux intensity of the secondary X-rays is related with the position of the atoms and the number of electrons of a atom, i.e., the atomic number, as a result the spatial locations of the atoms are resolved.

---

<sup>1</sup>The specific experimental conditions in an experiment are concretely described in every experiment section later.

### 2.1.1 Diffraction geometry

The principle of X-ray diffraction (XRD) was simply explained by W. L. Bragg [29]. In a typical XRD experiment (see Fig 2.1), a monochromatic X-ray beam with wavelength  $\lambda$ , is incident on planes with a certain Miller index (hkl) in the real lattice of the crystalline sample. The reflected beams with strengthened intensity are observed by the detector when constructive interference occurs for the plane set, i.e., when the famous Bragg's Law is satisfied,

$$n\lambda = 2d_{hkl}\sin\theta \quad (2.1)$$

where  $n$  is the order of diffraction;  $d_{hkl}$  is the interplanar spacing for planes (hkl); and  $2\theta$  is the angle between incident and reflected beams.

If  $\mathbf{a}$ ,  $\mathbf{b}$  and  $\mathbf{c}$  are primitive vectors of the real lattice, then the axis vectors  $\mathbf{A}$ ,  $\mathbf{B}$  and  $\mathbf{C}$  of the so called reciprocal lattice are defined as

$$\mathbf{A} = 2\pi \frac{\mathbf{b} \times \mathbf{c}}{\mathbf{a} \cdot \mathbf{b} \times \mathbf{c}}; \mathbf{B} = 2\pi \frac{\mathbf{c} \times \mathbf{a}}{\mathbf{a} \cdot \mathbf{b} \times \mathbf{c}}; \mathbf{C} = 2\pi \frac{\mathbf{a} \times \mathbf{b}}{\mathbf{a} \cdot \mathbf{b} \times \mathbf{c}} \quad (2.2)$$

The diffraction geometry is also conveniently expressed in reciprocal lattice as

$$\Delta\mathbf{k} = \mathbf{G}_{hkl} \quad (2.3)$$

where  $\Delta\mathbf{k} = \mathbf{k}' - \mathbf{k}$ ,  $\mathbf{G}_{hkl}$  is a vector in reciprocal lattice and represents a plane set (hkl) in the real lattice. This expression is easily demonstrated using Ewald construction (see Fig 2.1, bottom panel).

### 2.1.2 Diffraction cross section

The traditional XRD experiment described above is in essence Thomson scattering arising from the charged electrons. The diffraction intensity consists of contribution from all the charges of electrons of atoms in the lattice. Every kind of atom has a specific scattering strength  $f$ , which is termed as atomic form factor  $f_j$  for the  $j$ th atom,

$$f_j = \int dV n_j(\mathbf{r} - \mathbf{r}_j) e^{-i\mathbf{G} \cdot (\mathbf{r} - \mathbf{r}_j)} \quad (2.4)$$

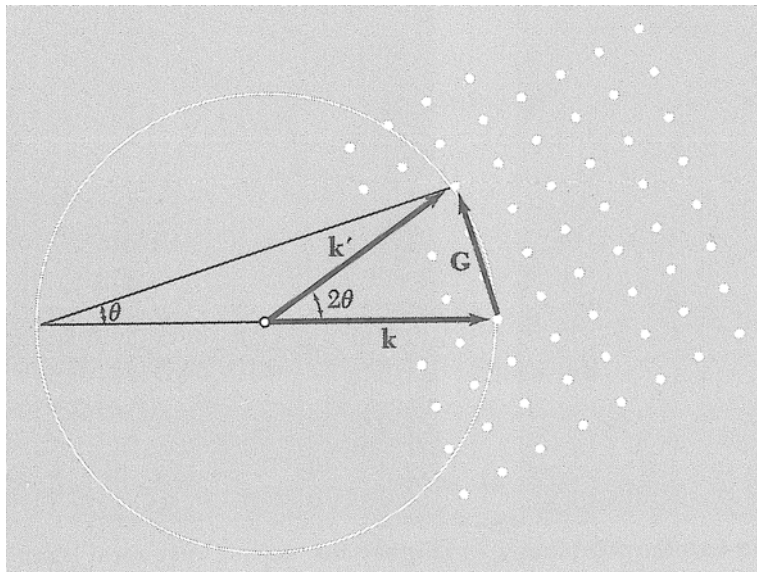
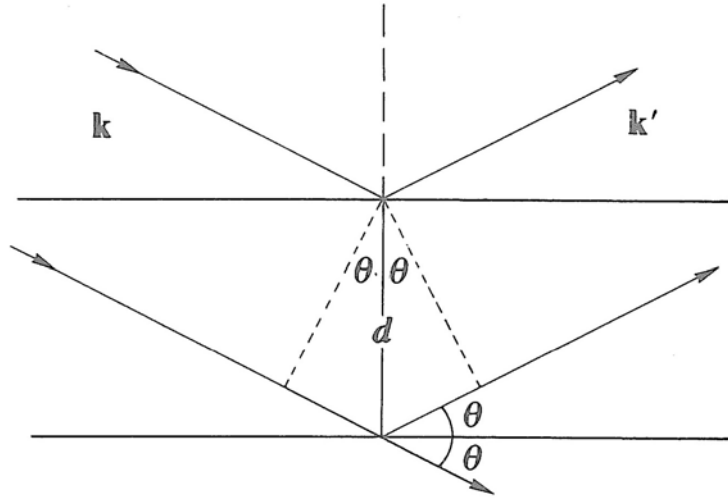


Figure 2.1: Geometry of X-ray diffraction in real lattices (top) and in reciprocal lattices (bottom). Figure taken from [28] and [30] respectively.

where  $\mathbf{r}_j$  is the vector to the centre of atom  $j$ ;  $n_j(\mathbf{r} - \mathbf{r}_j)$  gives the contribution of the  $j$  atom to the electron density at  $\mathbf{r}$ ; and  $\mathbf{G}$  is a vector in reciprocal lattice, as defined in the last subsection. The atomic form factor is therefore an atomic property which depends on the number of electrons, i.e., the atomic number  $Z$  the atom has. Moreover, the atomic form factor is anisotropic. This arises in that the size of the atom is comparable to the wavelength of the X-rays and beams are scattered slightly out of phase by different parts of the atomic charge cloud. The angular dependence of the atomic form factor for different elements are constructed and given in

reference books. Taking into account the contributions from all kinds of atoms in a cell, yields the so called structure factor,

$$F_{\mathbf{G}} = \sum_j f_j e^{-i\mathbf{G}\cdot(\mathbf{r}-\mathbf{r}_j)} \quad (2.5)$$

For the reflection labelled by  $h, k, l$ , it reads,

$$F_{\mathbf{G}}(hkl) = \sum_j f_j e^{-i2\pi(hu_j+kv_j+lw_j)} \quad (2.6)$$

where  $u, v$  and  $w$  are the coordinates of the atoms in units of the cell vectors. The scattering intensity for a crystal is then given as

$$I = F_{\mathbf{G}}(hkl) \cdot F_{\mathbf{G}}(hkl)^* \quad (2.7)$$

## 2.2 X-ray absorption spectroscopy

When a beam of X-rays are incident on matter, their oscillating electric field may "react" with the electrons of the atoms. The photons may either be scattered as a process of X-ray diffraction, or be absorbed by the electrons and excite the electrons from a core shell to an empty state above the Fermi level, provided that the photon energy is equal or higher than the binding energy of the core level. The latter process forms the basis of X-ray absorption spectroscopy (XAS) (see Fig 2.3), which is an important technique capable of providing information on the electronic, structural and magnetic properties of materials.

### 2.2.1 Theory

The Hamiltonian associated with the interaction of X-rays with electrons can be given approximately in perturbation theory which describes the action of an electric field  $\mathbf{E}$  of X-rays on the electron moments is given as

$$\mathcal{H}_{int} = \sum_l \frac{e}{mc} \mathbf{p}_l \cdot \mathbf{A}(\mathbf{r}_l, t) + \frac{e^2}{2mc^2} \mathbf{A}(\mathbf{r}_l, t) \cdot \mathbf{A}(\mathbf{r}_l, t), \quad (2.8)$$

where the subscript  $l$  means the  $l$ th electron of the atom;  $e$  is the electron charge;  $m$  is the mass;  $c$  is the speed of light;  $\mathbf{p}$  is momentum operator of an electron; and  $\mathbf{A}$  is the vector field of X-rays which is collinear with the electric field  $\mathbf{E}$ . The quantized electromagnetic field coupling to the electrons is given as

$$\mathbf{A}(\mathbf{r}, t) = \sqrt{\frac{2\pi\hbar c}{V}} \sum_{i, \mathbf{k}} \frac{1}{\sqrt{k}} e_i (a_{\mathbf{k}, i}(t) e^{i\mathbf{k}\cdot\mathbf{r}} + a_{\mathbf{k}, i}^+(t) e^{-i\mathbf{k}\cdot\mathbf{r}}), \quad (2.9)$$

where operator  $a_{\mathbf{k}, i}$  and  $a_{\mathbf{k}, i}^+$  annihilates and creates a photon with polarization  $\mathbf{e}_i$  and wave vector  $\mathbf{k}$  respectively.  $a_{\mathbf{k}, i}(t) = a_{\mathbf{k}, i}(0) \exp(-i\omega_{\mathbf{k}} t)$  and  $a_{\mathbf{k}, i}^+(t) = a_{\mathbf{k}, i}^+(0) \exp(-i\omega_{\mathbf{k}} t)$ . Therefore in the equation (2.8), the first term changes the number of photons by  $\pm 1$  while the second term by 0 or  $\pm 2$ . In the absorption process, a photon is annihilated therefore to describe the absorption process theoretically only the first term of equation (2.9) needs to be inserted into the first term of equation (2.8).

Similarly, the vector field  $\mathbf{A}$  can also be written in the form of a plane wave of electromagnetic radiation as [31],

$$\mathbf{A} = \hat{\mathbf{e}}_q A_0 \cos(kx - \omega t), \quad (2.10)$$

where  $\hat{\mathbf{e}}_q$  is the unit vector for a polarization  $q$ ;  $A_0$  is the amplitude;  $k$  is the wavevector;  $x$  is displacement;  $\omega$  is the frequency and  $t$  is the time. By using Euler's formula and keeping only the absorbing term  $e^{-i\omega t}$  the above equation reads

$$\mathbf{A} = \frac{1}{2} \hat{\mathbf{e}}_q A_0 e^{i(kx - \omega t)}. \quad (2.11)$$

The transition rate of the above interaction can be quantified by Fermi's golden rule

$$W_{fi} = \frac{2\pi}{\hbar} |\langle \Phi_f | T | \Phi_i \rangle|^2 \delta_{E_f - E_i - \hbar\omega}, \quad (2.12)$$

where  $W_{fi}$  is the probability of transition per unit time from an initial state  $i$  to a final state  $f$ ;  $\Phi_i$  and  $\Phi_f$  is the wavefunction of the initial and final state of the reaction respectively which is built from an electron component and a photon component;  $E_i$  and  $E_f$  is the energy for the initial and final state respectively; and  $T$  is the transition operator. The condition indispensable for an transition to occur is given in the delta function in which  $E_f$  must

be equal to the sum of  $E_i$  and the energy of the incident X-rays, which reflects the energy conservation. The transition rate is given in the squared matrix.

All the possible transitions are given in  $T$  and written as  $T = \sum T_i$ . The XAS process involving one-photon transitions is then given by the first order transition operator  $T_1$ , which equals the first term of the interaction Hamiltonian  $\mathcal{H}_{int}$ . Inserting exponential form of  $\mathbf{A}$  (i.e., equation (2.11)) into this term yields

$$T_1 \propto \sum_q (\hat{\mathbf{e}}_q \cdot \mathbf{p}) e^{i\mathbf{k} \cdot \mathbf{r}}, \quad (2.13)$$

In dipole approximation, the transition operator  $T_1$  is written as

$$T_1 \propto \sum_q (\hat{\mathbf{e}}_q \cdot \mathbf{p}) \quad (2.14)$$

This equation is further simplified by omitting the summation over  $\mathbf{k}$  and using the commutation law between the position vector  $\mathbf{r}$  and the atomic Hamiltonian and reads

$$T_1 = \sum_q (\hat{\mathbf{e}}_q \cdot \mathbf{r}). \quad (2.15)$$

Fermi's golden rule can then be transcribed as

$$W_{fi} \propto \sum_q |\langle \Phi_f | \hat{\mathbf{e}}_q \cdot \mathbf{r} | \Phi_i \rangle|^2 \delta_{E_f - E_i - \hbar\omega}, \quad (2.16)$$

Assuming only one electron is excited upon absorbing the photon energy and all other electrons remain unaffected, then  $\Phi_i$  may be written as a core wave function  $c$  and  $\Phi_f$  as a free electron wave function  $\varepsilon$ , then the transition rate is

$$W_{fi} \propto \sum_q |\langle \varepsilon | \hat{\mathbf{e}}_q \cdot \mathbf{r} | c \rangle|^2 \delta_{E_f - E_i - \hbar\omega}, \quad (2.17)$$

The squared matrix element is found to be affected very little by energy but the delta function certainly is. Fermi's golden rule can then be rewritten as intensity observed in XAS as follow,

$$I_{XAS} \propto a^2 \rho \quad (2.18)$$

where  $\rho$  is the density of empty states above the Fermi level and  $a$  is the dipole transition matrix.  $a$  is nontrivial when the transition satisfies the selection rules in which the spin remains the same for the final state and the initial state while the orbital quantum number is different by 1, for instance,  $s \rightarrow p$ . This final expression suggests that XAS probes in essence the density of empty states, which is the theoretical basis of the XAS.

### 2.2.2 Techniques

In a practical XAS experiment, the X-ray absorption cross-section as a function of the photon energy will show an abrupt increase which corresponds to a characteristic core-electron binding energy and is called an absorption edge. The edges are named in terms of the principal quantum number of the electron that is excited: e.g., K for  $n = 1$ , L for  $n = 2$  and M for  $n = 3$  (see Table 2.1). The absorption edges are characteristic of an element, therefore XAS is an element specific technique.

Table 2.1: Absorption edges and the corresponding core levels.

Absorption edge	Core state
M <sub>5</sub>	3d <sub>5/2</sub>
M <sub>4</sub>	3d <sub>3/2</sub>
M <sub>3</sub>	3p <sub>3/2</sub>
M <sub>2</sub>	3p <sub>1/2</sub>
M <sub>1</sub>	3s
L <sub>3</sub>	2p <sub>3/2</sub>
L <sub>2</sub>	2p <sub>1/2</sub>
L <sub>1</sub>	2s
K	1s

Two main regions can generally be found in a typical absorption spectrum: X-ray absorption near-edge structure (XANES) and X-ray absorption fine structure (EXAFS). The former is the technique of interest in this thesis. It is usually characterized by a jump in the vicinity of the absorption edge. This arises from transitions of core electrons to unoccupied states above the Fermi level with close energy and can provide information on the electronic properties of the absorbing atom. Since the XANES is capable of directly probing the valence state, it is well-established to determine the valence of elements in materials [32]. An element with different charge states has

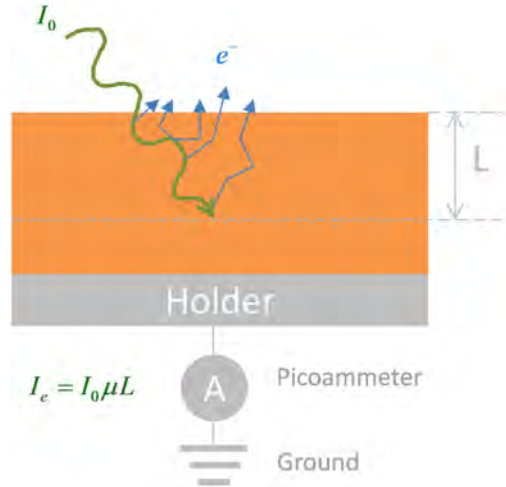


Figure 2.2: Total electron yield mode for soft X-ray absorption spectroscopy.

different ionization potentials, therefore the absorption edge is different. More concretely, the edge is shifted to lower (higher) photon energy if the element is present as anion (cation).

Usually either of two modes are used to detect the absorption. In **transmission mode**, the absorption is observed by comparing the intensity of the X-rays before and after transmission through the sample. The intensity of X-ray beam is attenuated in an exponential fashion,

$$I(\omega) = I_0(\omega)e^{-\mu(\omega)L}, \quad (2.19)$$

and absorption cross-section  $\mu$  is then given by

$$\mu(\omega) = \frac{1}{L} \ln \frac{I_0}{I}, \quad (2.20)$$

where  $I_0$  is the intensity of the incident X-rays;  $I$  is intensity of transmitted beam; and  $\omega$  denotes the energy of the photons;  $L$  is the attenuation length. Transmission mode suits hard X-rays which are of high energies and have a large typical attenuation length. For soft X-rays of typical energies less than 1 keV, the **total electron yield** (TEY) is usually used (see Fig 2.2). The electric current induced by the electrons that escape from the sample surface are detected when the energy of the photons is absorbed, similarly by using

$$I_e(\omega) = I_0(\omega)e^{-\mu(\omega)L}, \quad (2.21)$$

the absorption cross-section  $\mu$  is obtained. The attenuation length is typically only  $3 \sim 10$  nm.

## 2.3 Resonant X-ray diffraction

Resonant X-ray diffraction (RXD) has proved to be a powerful tool in modern solid state physics to investigate magnetic, orbital and charge ordering phenomena associated with electronic degrees of freedom [33]. It is a combination of XRD and XAS in one single experiment and thereby possesses the advantages of both techniques. The XRD component resolves the spatial modulations and the XAS component provides sensitivity to the electronic states.

### 2.3.1 Theory

RXD is in essence a two-photon transition process (see Fig 2.3): firstly, as for standard XAS, when absorbing the energy of the incident photon a core electron in the initial state  $|G\rangle$  is virtually excited into the unoccupied states close to the Fermi level creating a core hole and an intermediate state  $|I\rangle$ ; then the excited electron is recombined with the core hole and a photon with the same energy as the incident one is re-emitted and can be detected like a conventional XRD. In this way, the initial state  $|G\rangle$  is recovered.

This resonant scattering may be seen as a process of first annihilating and then creating a photon and can be described as

$$|G, \mathbf{k}, \mathbf{e}\rangle \rightarrow |G, \mathbf{k}', \mathbf{e}'\rangle \quad (2.22)$$

where  $\mathbf{e}$  and  $\mathbf{e}'$  denote respectively the polarization of X-rays before and after scattering. Defining the first order matrix element as,

$$a_1 = \langle G, \mathbf{k}', \mathbf{e}' | \mathcal{H}_{int} | G, \mathbf{k}, \mathbf{e} \rangle \quad (2.23)$$

and the second order matrix element as,

$$a_2 = \langle G, \mathbf{k}', \mathbf{e}' | \mathcal{H}_{int} \mathcal{H}_{int} | G, \mathbf{k}, \mathbf{e} \rangle \quad (2.24)$$

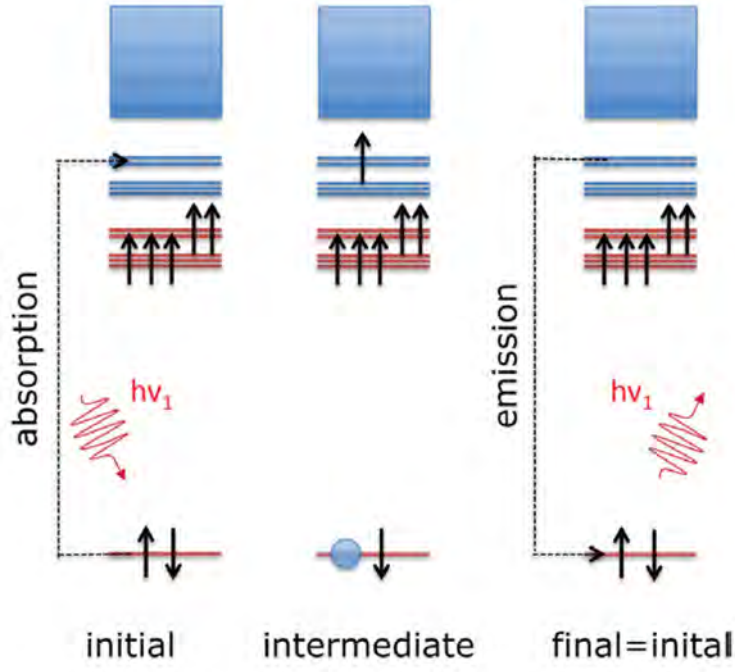


Figure 2.3: Schematic illustration of the resonant X-ray diffraction (after [34]). Note that the first two processes corresponding to absorption are in essence the basic principles of X-ray absorption spectroscopy.

where  $\mathcal{H}_{int}$  is given in equation (2.8). It is easily seen that only the second term of equation (2.8), i.e.,  $\mathbf{A} \cdot \mathbf{A}$  contributes to  $a_1$  since it does not change number of photons. Nevertheless the first term  $\mathbf{p}_l \cdot \mathbf{A}$  gives non-zero contribution to the  $a_2$  in a way of two successive  $\mathbf{p}_l \cdot \mathbf{A}$  interactions. Considering both of the orders  $a_1$  and  $a_2$ , the probability of a photon to be scattered into the solid angle  $d\Omega$ , i.e., the differential cross-section is

$$\frac{d\sigma}{d\Omega} = \frac{e^2}{mc^2} \left| \mathbf{e} \cdot \mathbf{e}' \langle G | \rho(\mathbf{Q}) | G \rangle - m \sum_I \frac{\langle G | \mathbf{e}' \cdot \mathbf{J}(\mathbf{k}') | I \rangle \langle I | \mathbf{e} \cdot \mathbf{J}(-\mathbf{k}) | G \rangle}{E_I - E_G - \hbar\omega - i\Delta_I/2} \right|^2, \quad (2.25)$$

where  $\rho(\mathbf{Q})$  is the Fourier amplitude of the charge density;  $\Delta_I$  is the life time of the intermediate state  $|I\rangle$ ;  $\mathbf{J}(\mathbf{k}) = 1/m \sum_l \mathbf{p}_l \exp(i\mathbf{k} \cdot \mathbf{r}_l)$  denotes the current operator which describes the transitions between the state  $|G\rangle$  and the  $|I\rangle$ ; and the other parameters are defined as before. This expression actually corresponds to form factor and is of the form

$$|f(\omega, \mathbf{e}, \mathbf{e}')|^2 = f^0(\mathbf{Q}, \mathbf{e}, \mathbf{e}') + \Delta f(\hbar\omega, \mathbf{e}, \mathbf{e}', \mathbf{k}, \mathbf{k}'), \quad (2.26)$$

where  $f^0$  is the Thomson scattering and  $\Delta f$  represents the anomalous dispersion correction which has the complex form of

$$\Delta f = f' - if'', \quad (2.27)$$

where  $f'$  and  $f''$  are all real numbers.  $\Delta f$  serves as a modulation of the atomic form factor and it is large at the absorption edge. These are tabulated well as Henke-Gullikson factors wherein  $f_1 = Z+f'$  and  $f_2 = f''$ .

The reason why RXD is powerful for investigating magnetic, orbital and charge ordering phenomena is seen from the structure factor expressed according to Loversey *et al* [33]

$$F(E) \propto \sum_{K,Q} \sum_q (-1)^Q H_{-Q}^K D_{Qq}^K \sum_d \langle T_q^k \rangle_d e^{id \cdot \tau}, \quad (2.28)$$

where  $d$  is the position of the resonant ions in the unit cell;  $\tau$  is the reciprocal lattice vector in question;  $D_{Qq}^K$  expresses an axis transformation of the operators from the local site system to the experiment setup;  $H_{-Q}^K$  describes the polarization and direction of the X-ray; and  $\langle T_q^k \rangle$  stands for the expectation value for an atomic multipole moment with rank  $k$  and projection  $q$  in the local axis system of the resonant ion and

$$\langle T_q^k \rangle \propto \sum_n \frac{\langle G|O|I \rangle \langle I|O^*|G \rangle}{E_I - E_G - \hbar\omega + i\Delta/2} \quad (2.29)$$

shows that the expectation value for an atomic multipole moment becomes larger when the energy of the incident X-ray matches the absorption edge. The resulting tensor  $\langle T_q^k \rangle$  gives the atomic multipole of the relevant valence shell with  $k = 0$  for charge order (monopole),  $k = 1$  for magnetic order (dipole) and  $k = 2$  for orbital order (quadrupole).

### 2.3.2 Diffraction geometry and cross section

The geometry of a typical RXD experiment is shown in Fig 2.4 within a Cartesian system. X-rays with a chosen linear polarization,  $\sigma$  or  $\pi$ , are incident on a single crystal specimen and are scattered elastically with linear polarization(s)  $\sigma'$  and/or  $\pi'$ . The  $\sigma$  ( $\pi$ ) polarization is defined as electric field vector perpendicular (parallel) to the scattering plane  $xy$ .

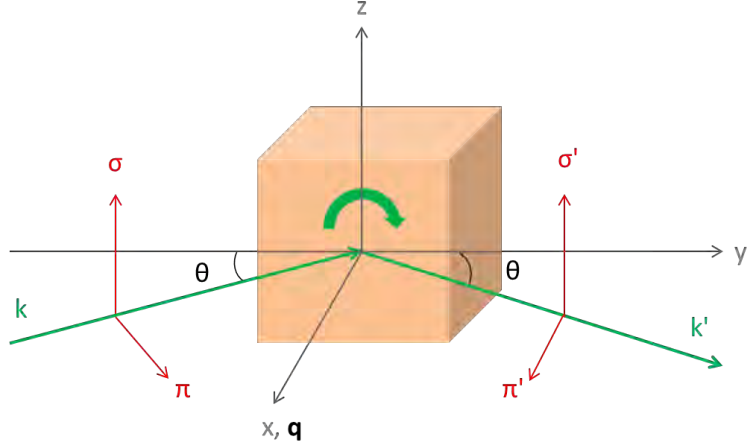


Figure 2.4: The scattering geometry of resonant X-ray diffraction.

Conventionally, there are three scan types. A  $\theta - 2\theta$  scan is defined as scanning along the scattering vector  $\mathbf{q} = \mathbf{k}' - \mathbf{k}$ . In practice, the specimen and the detector are rotated in steps of  $\Delta\theta$  and  $2\Delta\theta$  respectively. An energy scan is a measurement of photon energy dependence of a given reflection at a fixed  $\mathbf{q}$ . While in an azimuth scan, the resonant reflection signal is measured as the specimen is rotated about  $\mathbf{q}$ . Information on the polarization dependence of the resonant scattering is obtained via this scan.

The resonant scattering structure factor for a free atom with a magnetic moment  $\hat{\mathbf{s}}$  can be expressed more concretely in the dipole approximation as [35],

$$\Delta f = (\hat{\boldsymbol{\varepsilon}}' \cdot \hat{\boldsymbol{\varepsilon}})F^{(0)} - i(\hat{\boldsymbol{\varepsilon}}' \times \hat{\boldsymbol{\varepsilon}}) \cdot \hat{\mathbf{s}}F^{(1)} + (\hat{\boldsymbol{\varepsilon}}' \cdot \hat{\mathbf{s}})(\hat{\boldsymbol{\varepsilon}} \cdot \hat{\mathbf{s}})F^{(2)}, \quad (2.30)$$

where  $\hat{\boldsymbol{\varepsilon}}$  and  $\hat{\boldsymbol{\varepsilon}}'$  are the incident and scattered polarization electric field vectors respectively and  $F^{(j)}$  ( $j = 0, 1, 2$ ) are photon energy dependent resonance factors.

The first term has no dependence on the magnetic moment and corresponds to Thomson charge scattering; the second term contributes to first-harmonic magnetic satellites and the third term gives second-harmonic magnetic satellites.

The first dipole operator in equation (2.30) results in a  $\sigma - \sigma'$  or  $\pi - \pi'$  scattering with no change of polarization. It can be written as a  $2 \times 2$  matrix diagonal with elements  $\hat{\boldsymbol{\varepsilon}}'_{\perp} \cdot \hat{\boldsymbol{\varepsilon}}_{\perp} = 1$  and  $\hat{\boldsymbol{\varepsilon}}'_{\parallel} \cdot \hat{\boldsymbol{\varepsilon}}_{\parallel} = \cos 2\theta = \hat{\mathbf{k}}' \cdot \hat{\mathbf{k}}$  ( $\theta$

is the Bragg angle), and

$$\hat{\varepsilon}' \cdot \hat{\varepsilon} = \begin{pmatrix} 1 & 0 \\ 0 & \hat{\mathbf{k}}' \cdot \hat{\mathbf{k}} \end{pmatrix}. \quad (2.31)$$

In contrast,  $\sigma - \sigma'$  scattering is forbidden by the second dipole operator but  $\sigma - \pi'$  and  $\pi - \sigma'$  are allowed. That is,  $\hat{\varepsilon}'_{\parallel} \times \hat{\varepsilon}_{\perp} = -\hat{\mathbf{k}}'$ ,  $\hat{\varepsilon}'_{\perp} \times \hat{\varepsilon}_{\parallel} = \hat{\mathbf{k}}$ , and  $\hat{\varepsilon}'_{\parallel} \times \hat{\varepsilon}_{\parallel} = \hat{\mathbf{k}}' \times \hat{\mathbf{k}}$  can enter the matrix as

$$\hat{\varepsilon}' \times \hat{\varepsilon} = \begin{pmatrix} 0 & \hat{\mathbf{k}} \\ \hat{\mathbf{k}}' & \hat{\mathbf{k}}' \times \hat{\mathbf{k}} \end{pmatrix}. \quad (2.32)$$

The resonant scattering structure factor can then be written as

$$\begin{aligned} \Delta f = & F^{(0)} \begin{pmatrix} 1 & 0 \\ 0 & \cos 2\theta \end{pmatrix} \\ & - iF^{(1)} \begin{pmatrix} 0 & s_y \cos \theta + s_x \sin \theta \\ s_x \sin \theta + s_y \cos \theta & -s_z \sin 2\theta \end{pmatrix} \\ & + F^{(2)} \begin{pmatrix} s_z^2 & -s_z(s_y \sin \theta + s_x \cos \theta) \\ s_z(s_y \sin \theta + s_x \cos \theta) & -\cos^2 \theta (s_y^2 \tan^2 \theta + s_x^2) \end{pmatrix}. \end{aligned} \quad (2.33)$$

## 2.4 Scanning Electron Microscopy

Scanning Electron Microscopy (SEM) uses high-energy electron beams to probe the surface morphology and chemical composition of the sample. When a focused beam of high-energy electrons is incident on the sample surface, a variety of signals are generated from the interactions of the incident electrons with the atoms at or close to the sample surface. Secondary electrons are signals that arise from the ionisation of the inner-shell electrons when their energy exceeds the ionization potential upon absorbing the energy of the incident electrons. The number of secondary electrons generated depends on the angle between the surface and the beam. This signal can thus be detected and employed to image the surface and to reveal the morphology and topology of the sample. The characteristic X-ray with a specific wavelength is another useful signal which is resulted from decaying of the high-level electrons to the core-holes that are left behind

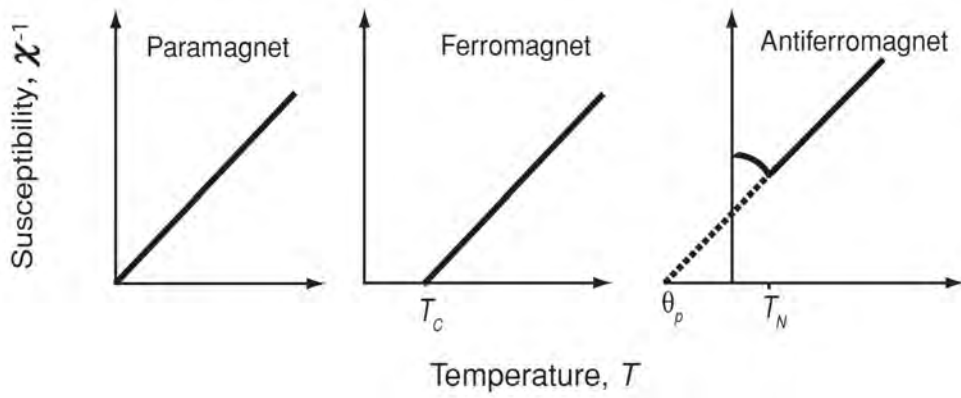


Figure 2.5: Dependence of inverse susceptibility on temperature for three typical types of magnetic materials [36].

during emission of secondary electrons. The characteristic X-ray is sensitive to elements and is a fingerprint of a certain element. Moreover the relative intensity of the characteristic X-ray reflects the abundance of that element in a sample. This signal can therefore be exploited to determine the chemical composition of the sample, which is usually performed on an energy-dispersive X-ray spectroscopy (EDS) integrated in a SEM system.

## 2.5 Magnetization measurements

Magnetic properties of a matter are characterised by magnetization and magnetic susceptibility. Magnetization is defined as the magnetic dipole moments which are induced by a magnetic field or inherent to a magnetic material, in a unit volume,

$$M = N\mu \quad (2.34)$$

where  $N$  is the number of magnetic dipole moments per unit volume;  $\mu$  is the magnetic moment. Magnetic susceptibility is defined as

$$\chi = \frac{M}{H} \quad (2.35)$$

where  $H$  is the external magnetic field. Different type of magnetic materials have distinct responses to an applied magnetic field, therefore the behaviour of magnetization and susceptibility is distinct (see Fig 2.5).

Magnetic susceptibility of **paramagnetism** shows a reciprocal temperature dependence that was found by Curie in 1895 and termed as Curie's law as,

$$\chi = \frac{C}{T} \quad (2.36)$$

where C is the Curie constant. The law is theoretically explained by Langevin as

$$M = N\langle\mu\rangle = N\mu L(\alpha) \quad (2.37)$$

where  $L(\alpha) = \coth\alpha - 1/\alpha$  is the Langevin function;  $\alpha = \mu B_0/k_B T$ ; N is the number of atoms per unit volume;  $\mu$  is the atomic magnetic moment; and  $B_0$  is the magnetic field.

For that of **ferromagnetism**, Curie's law is modified to give the Curie-Weiss law,

$$\chi = \frac{C}{T - T_C} \quad (2.38)$$

where  $T_C$  is Curie temperature. It is a critical point above which the exchange coupling of the neighbouring atomic moments is ruined by the thermal energy and the spontaneous magnetization is lost. The material therefore becomes paramagnetic and obey the the Curie-Weiss law.

While for that of **antiferromagnetism**,

$$\chi = \frac{C}{T - \theta_p} \quad (2.39)$$

where  $\theta_p$  is the antiferromagnetic Curie temperature which is a negative value. This formula is valid above  $T_N$ , the *Néel* temperature. Below  $T_N$ , the system becomes ordered and the magnetic moments in two sublattices are aligned more antiparallel to each other as temperature decreases, with eventually a zero net magnetization at  $T = 0$  K. The susceptibility therefore increases as the temperature increases. Above  $T_N$  because of the thermal fluctuation the antiferromagnetic order is lost and the system becomes paramagnetic. The susceptibility decreases with increasing temperature. Therefore  $T_N$  is usually observed as a peak in a  $\chi - T$  curve. In a  $1/\chi - T$  curve the antiferromagnetic feature is usually seen as a negative intercept on the temperature axis and a linear relationship between  $1/\chi$  and T above  $T_N$ .

**Diamagnetism** is a negative contribution to the total susceptibility and is present in all forms of matter due to a small negative induced moment in an applied magnetic field. It is characterised by a negative constant susceptibility or a straight line passing through zero with a negative slope in a  $M-H$  curve. Diamagnetism dominates in case where the material has closed electron shells and no magnetic moment.

# Chapter 3

## Synthesis and characterisation of vanadium doped $\text{La}_2\text{Ti}_2\text{O}_7$

### 3.1 Introduction

The layered perovskite oxide  $\text{La}_2\text{Ti}_2\text{O}_7$  (LTO) of the type  $\text{A}_n\text{B}_n\text{O}_{3n+2}$  ( $n = 4$ ) is reported to be ferroelectric (FE) with a spontaneous polarization of magnitude  $5 \mu\text{C}/\text{cm}^2$  at room temperature and a  $T_C$  of 1770 K [37]. The ferroelectricity was recently found to originate from dipoles induced by antiferrodistortive oxygen octahedral rotations which do not cancel out in a naturally layered structure, rather than the conventional physical pictures [38]. Because of the essential role of its unique layered structure, the material is named a topological ferroelectric.

Recently density function calculations suggest a novel route to multiferroicity by doping a certain amount of magnetic ion vanadium into ferroelectric LTO to substitute for Ti [40, 41]. At a suitable temperature, vanadium with nominally a valence of 4+ and an outer orbital of  $3d^1$  in LTO was found to be able to cluster in long, homogeneous dimer-like chains -V-V-Ti-Ti- along  $a$  direction and generate robust ferromagnetic order which is more desired in techniques, and preserve the FE polarization as well as a small gap. However, so far no experimental evidence exists to prove the validity of this theoretical calculation.

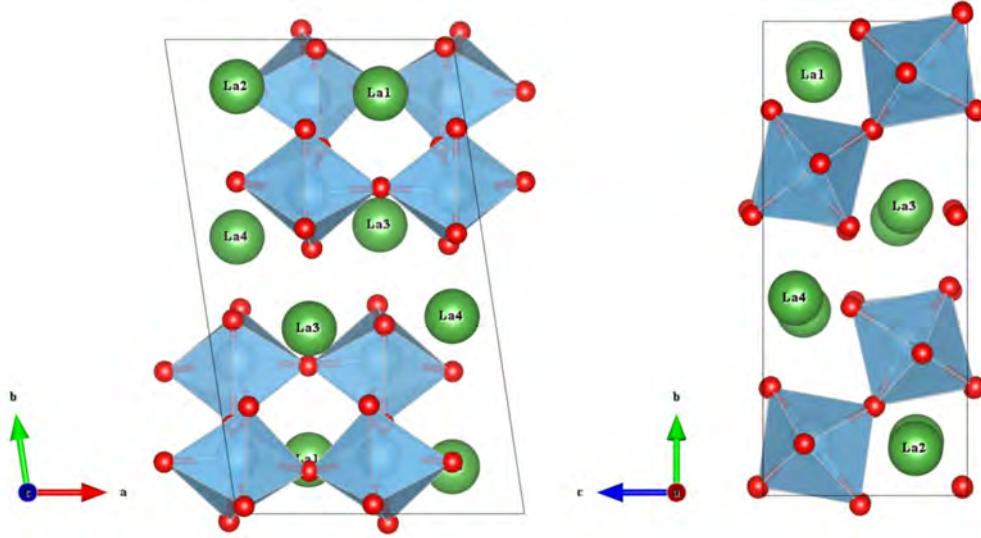


Figure 3.1: Crystal structure of the layered perovskite oxide  $\text{La}_2\text{Ti}_2\text{O}_7$  with space group  $P2_1$  in different views created by VESTA program [39]. Ti atoms (represented by blue balls) are in an octahedral environment of oxygen (red dots).

In this study, we have synthesized  $\text{La}_2\text{Ti}_{2-x}\text{V}_x\text{O}_7$  experimentally and investigated its crystal structure, magnetic properties, for the purpose of experimentally assessing whether the above theoretical calculations are valid.

## 3.2 Synthesis and characterization

### 3.2.1 Challenges of doping vanadium into $\text{La}_2\text{Ti}_2\text{O}_7$

There are several challenges in preparing  $\text{La}_2\text{Ti}_{2-x}\text{V}_x\text{O}_7$  samples which are outlined below.

Firstly, the  $\text{La}_2\text{V}_2\text{O}_7$  pyrochlore compound is not a stable phase. This is due to the disproportionation reaction of light rare-earth vanadium oxides [42]. For  $\text{La}_2\text{V}_2\text{O}_7$  the disproportionation reaction is:



wherein  $\text{V}^{4+}$  disproportionates into  $\text{V}^{3+}$  and  $\text{V}^{5+}$ . The Gibbs energy change for the above equation is negative thus the reaction is prone to proceed. Based on this, we may expect that, although the doping might be successful, there is an upper limit to the doping concentration.

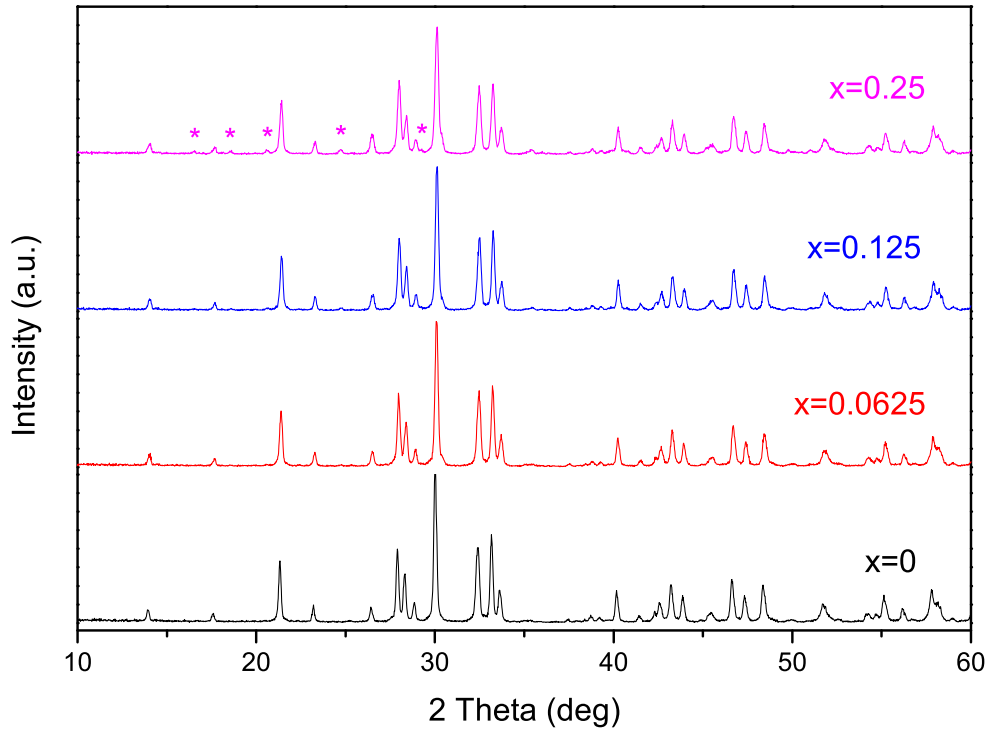


Figure 3.2: XRD pattern of  $\text{La}_2\text{Ti}_{2-x}\text{V}_x\text{O}_7$  ( $x = 0.0625, 0.125$  and  $0.25$ ) prepared by annealing in air. The peaks marked by asterisks are identified as the  $\text{LaVO}_4$  phase.

Secondly, preparation of the LTO phase itself is also a challenge. This lies in the fact that  $\text{La}_2\text{O}_3$  must be used as a starting material if a solid state reaction method is adopted for the synthesis.  $\text{La}_2\text{O}_3$  is reported to be very hygroscopic [43] and consist of carbonate and dioxycarbonate which are still stable at temperatures as high as  $500\text{ }^\circ\text{C}$  [44]. This suggests that the as-received raw material of this chemical contains many impurities. Therefore to yield the right stoichiometry in the final products, prior to use, proper heat treatment should be carried out in order to remove the impurities and water.

### 3.2.2 Synthesis

LTO and the doped samples were synthesized by solid state reaction.  $\text{La}_2\text{O}_3$  (99.9% pure, Aldrich),  $\text{TiO}_2$  (99.9% pure, Aldrich) and  $\text{VO}_2$  (99.99% pure, Aldrich) were chosen as starting materials which were treated differently prior to use. The  $\text{VO}_2$  was used as received. The  $\text{TiO}_2$  was heated in a box furnace at  $200\text{ }^\circ\text{C}$  overnight and stored in an oven set at  $95\text{ }^\circ\text{C}$ .

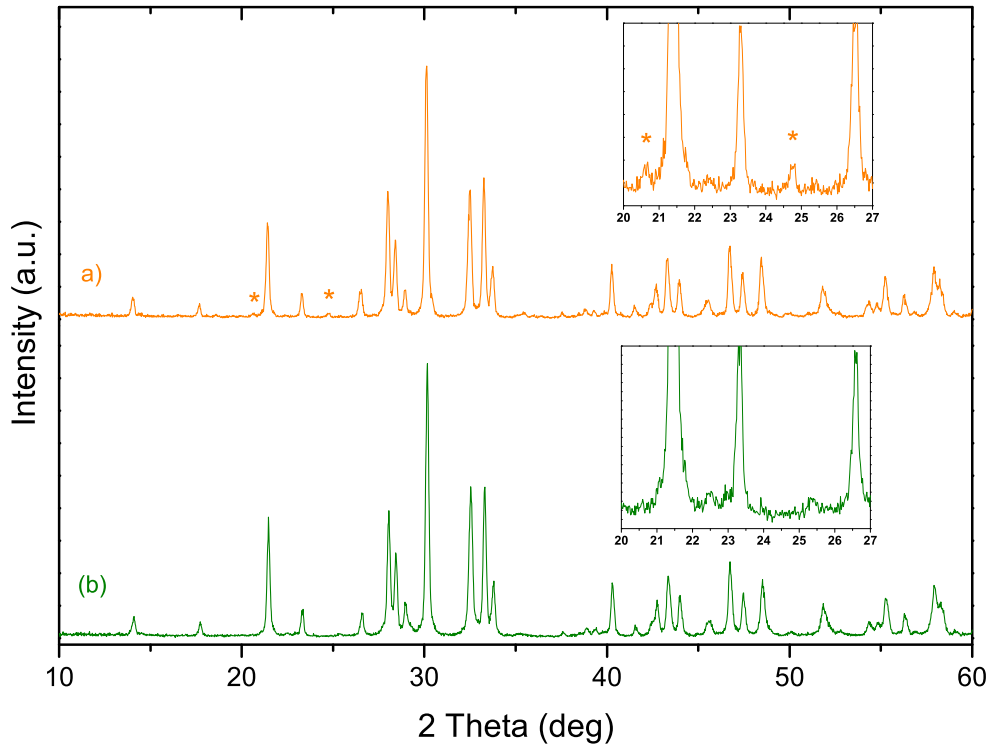


Figure 3.3: XRD pattern of  $\text{La}_2\text{Ti}_{2-x}\text{V}_x\text{O}_7$  ( $x = 0.125$ ) prepared by a) air annealing and b) water quenching. The peaks marked by asterisks are identified as a  $\text{LaVO}_4$  phase. The insets show the magnified patterns with  $2\theta$  of  $20 \sim 27^\circ$ .

However  $\text{La}_2\text{O}_3$  was heated in a box furnace at  $900^\circ\text{C}$  overnight to remove completely water, possible carbonate and dioxycarbonate and weighed out as soon as it was cooled down to room temperature to avoid its further absorption of the water from the environment and other possible reactions in air. The mixture of the treated chemicals with the proper stoichiometry was then ground manually for approximately 30 min in an agate mortar and pressed into a pellet of a diameter 0.5 cm with a steel die. Afterwards two different annealing procedures were adopted, namely air annealing, and vacuum annealing plus water quenching (referred to as the water quenching method in the coming text). In the former method, the pellet sample was placed in a high-alumina crucible, heated at  $850^\circ\text{C}$  for 10 h in a box furnace followed by a  $1100^\circ\text{C}$  annealing session for another 10 h and finally cooled to room temperature. The heating and cooling ramp rate was set to 6 and  $15^\circ\text{C}/\text{min}$  respectively. While in the latter method, which is similar to that reported in [45], first, the pellet was placed on a high-alumina pad, and carefully inserted into a quartz tube, in order to prevent from possible reactions with the quartz tube during the subsequent heating

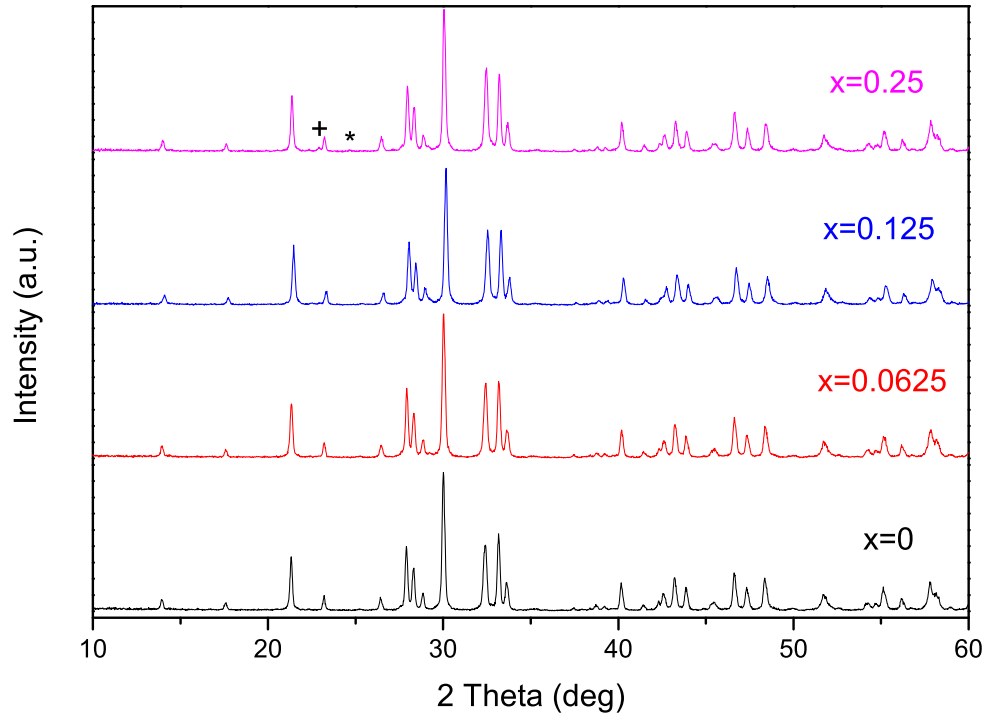


Figure 3.4: XRD pattern of  $\text{La}_2\text{Ti}_{2-x}\text{V}_x\text{O}_7$  ( $x = 0.0625, 0.125$  and  $0.25$ ) prepared by water quenching. A trace amount of  $\text{LaVO}_3$  and  $\text{LaVO}_4$  impurities are found for  $x = 0.25$  sample, marked by a plus mark and an asterisk mark respectively. The  $x = 0$  sample is prepared by air annealing.

sessions. Then the quartz tube with the sample inside was pumped to high vacuum, heated at  $200\text{ }^\circ\text{C}$  for about 30 min to remove possible water that was introduced during the grinding session, and sealed. The sample in a sealed quartz tube was subsequently heated to a temperature with a ramp rate approximately  $6\text{ }^\circ\text{C}/\text{min}$ , held for 2 days, and finally quickly water quenched to room temperature. Several temperatures, 800, 900 and  $1,000\text{ }^\circ\text{C}$  were tried and  $1000\text{ }^\circ\text{C}$  was finally chosen since the sample was only found to crystallize well after heating at this temperature for 2 days.

### 3.2.3 Crystal structure

The crystal structure of the sample was measured by a Miniflex X-ray Diffractometer with  $\text{Cu K}\alpha$  radiation. After a careful air annealing, the undoped sample was found to be the LTO pyrochlore single phase. However a certain amount of  $\text{LaVO}_4$  impurity phase is visible for all the doped samples (with  $x = 0.0625, 0.125$  and  $0.25$ ) and the impurity phase increases with doping concentrations (see Fig 3.2). Interestingly, this impurity phase is

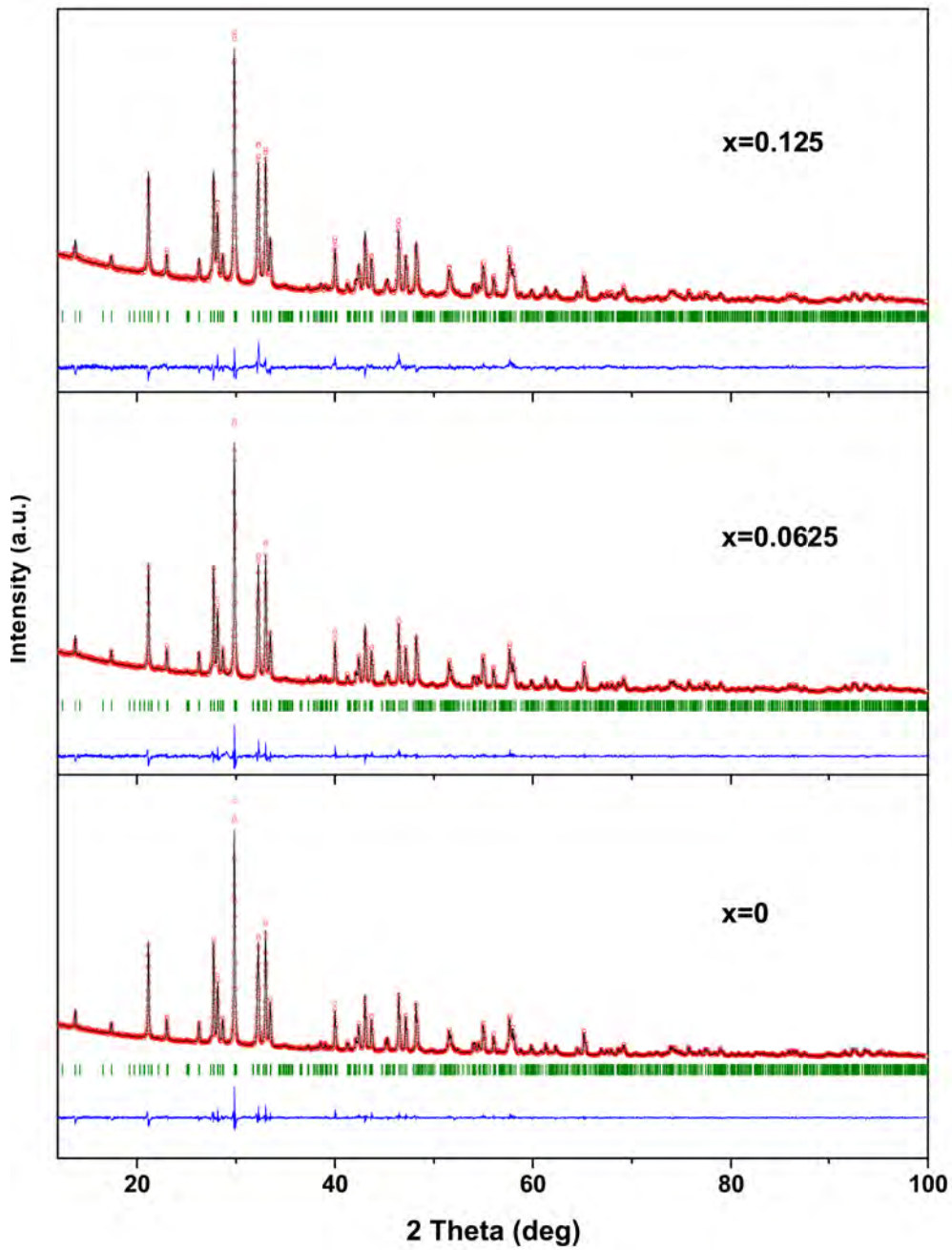


Figure 3.5: The refinement of XRD data of  $\text{La}_2\text{Ti}_{2-x}\text{V}_x\text{O}_7$  ( $x = 0, 0.0625$  and  $0.125$ ). The red circles are the observed data while the black solid line is the square-least fitted line; the green ticks shown below are the Bragg positions; the blue line at the bottom is the difference between the observed and calculated data.

not seen in the doped samples prepared by a water quenching method (with  $x = 0.0625$  and  $0.125$ ) (see Fig 3.3 and 3.4), suggesting that the growth of the impurity phase was effectively suppressed by the vacuum annealing and quick water quenching, for a doping concentration smaller than  $x = 0.125$ .

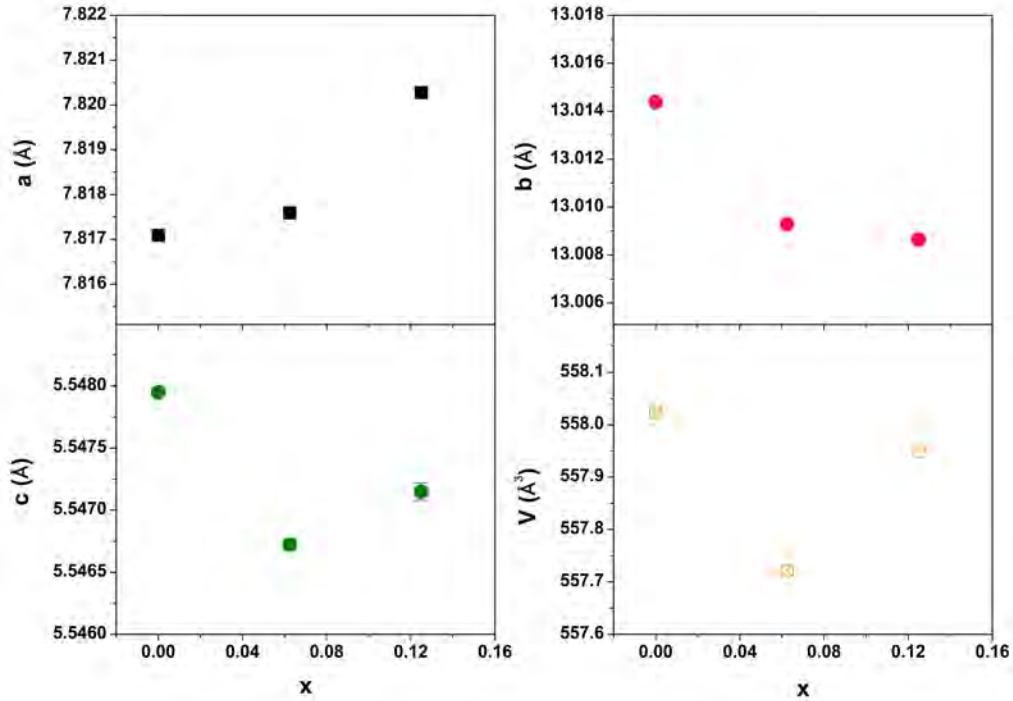


Figure 3.6: The lattice parameters of  $\text{La}_2\text{Ti}_{2-x}\text{V}_x\text{O}_7$  ( $x = 0, 0.0625$  and  $0.125$ ) obtained from the refinement. The error bars are created from the estimated standard deviations of the refined parameters; for  $a$ ,  $b$  and  $V$  they are smaller than the size of the plotting symbols.

While for  $x = 0.25$  sample, a trace amount of  $\text{LaVO}_3$  and  $\text{LaVO}_4$  impurities are found, resulting from the above mentioned disproportionation reaction. The  $\text{LaVO}_3$  phase is not found for the doped samples prepared by air annealing, which is probably due to the fact that this phase is oxidized to  $\text{LaVO}_4$  in the air.

In order to extract the lattice parameters, a PANalytical Empyrean X-ray diffractometer with  $\text{Cu K}\alpha$  radiation was employed to collect the diffracted signals with higher counts on the air annealed LTO and water quenched  $\text{La}_2\text{Ti}_{2-x}\text{V}_x\text{O}_7$  ( $x = 0.0625$  and  $0.125$ ). Counts as high as 14,000  $\sim$  20,000 were achieved for  $2\theta$  of  $10\sim 100^\circ$  in a typical measurement during about 1 h. The full profile Rietveld refinement of the XRD data was carried out on the *FullProf* program set [46], based on the space group  $\text{P2}_1$ . For the doped samples, vanadium atom was not included in the refinement. The refinement pattern are presented in Fig 3.5. The reliability factors of refinement are summarized in Table 3.1. These factors, together with refinement pattern show that all the refinements are well performed and the lattice models constructed are reasonable. The resulted lattice parameters

are shown in Fig 3.6. For the undoped sample,  $a = 7.81709(4) \text{ \AA}$ ,  $b = 13.01438(14) \text{ \AA}$ ,  $c = 5.54795(3) \text{ \AA}$ , and  $\gamma = 98.633(3)^\circ$ <sup>1</sup>, which agrees well with lattice parameters reported in the literature [47] ( $a = 7.800(3) \text{ \AA}$ ,  $b = 13.011(4) \text{ \AA}$ ,  $c = 5.546(2) \text{ \AA}$ , and  $\gamma = 98.60(2)^\circ$ ), and in turn confirms that the phase we obtained from the air annealing is the desired one. As can be seen, the doped sample has a smaller unit cell volume. This is a clue that vanadium atoms enter the lattice and substitute successfully for titanium atoms, since in coordination 6 radius of  $V^{4+}$  is  $0.58 \text{ \AA}$ , smaller than that of  $Ti^{4+}$ , i.e.,  $0.605 \text{ \AA}$ [48]. Surprisingly the volume does not decrease steadily with the doping concentration of vanadium; instead, it undergoes first a decrease for  $x = 0.0625$  sample and then an increase for the sample with  $x = 0.125$  although the volume found is still smaller than that of the pure undoped sample. The increase of volume is primarily due to a steady yet abnormal increase of the lattice parameter  $a$ . According to the theoretical calculation [40, 41], the doped vanadium preferably clusters a chain in  $a$  direction which induces ferromagnetic coupling between magnetic moments of the neighbouring atoms. The expansion of lattice in direction  $a$  indicates that some abnormality such as collapse of the chain might take place in this direction during the formation of the crystallite phase. This may in turn affect the magnetic properties of the samples.

Table 3.1: Reliability factors of refinement of  $La_2Ti_{2-x}V_xO_7$  ( $x = 0, 0.0625$  and  $0.125$ ).

$La_2Ti_{2-x}V_xO_7$	$R_p$	$R_{wp}$	$R_{exp}$	$\chi^2$	Bragg R-factor	RF-factor
$x = 0$	12.6	11.6	7.22	2.57	3.891	2.642
$x = 0.0625$	13.3	12.1	7.60	2.52	4.593	2.661
$x = 0.125$	14.9	13.8	7.97	3.00	6.969	3.280

Notes: definition of these factors are given in Appendix A.

### 3.2.4 Magnetic properties

The magnetic properties of the air annealed LTO and water quenched  $La_2Ti_{2-x}V_xO_7$  ( $x = 0.0625$  and  $0.125$ ) were measured as a function of magnetic field up to 10000 Oe and temperature (5~300 K) with a SQUID

<sup>1</sup>Numbers in parenthesis indicate estimated standard deviations of the refined parameters.

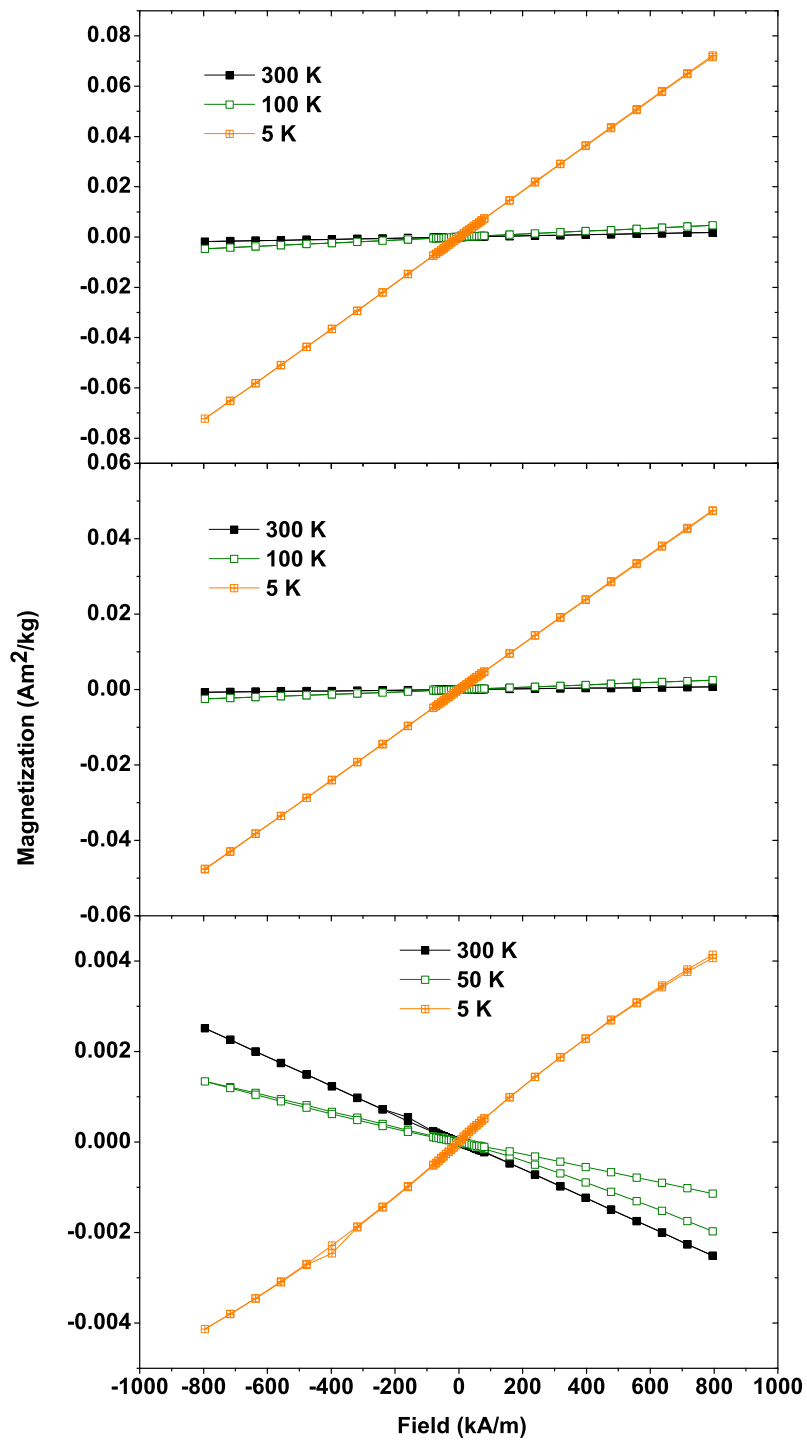


Figure 3.7: M-H curves for La<sub>2</sub>Ti<sub>2-x</sub>V<sub>x</sub>O<sub>7</sub> ( $x = 0, 0.0625$  and  $0.125$ , from bottom to top).

magnetometer.

The field dependence of the magnetization for all the samples is recorded

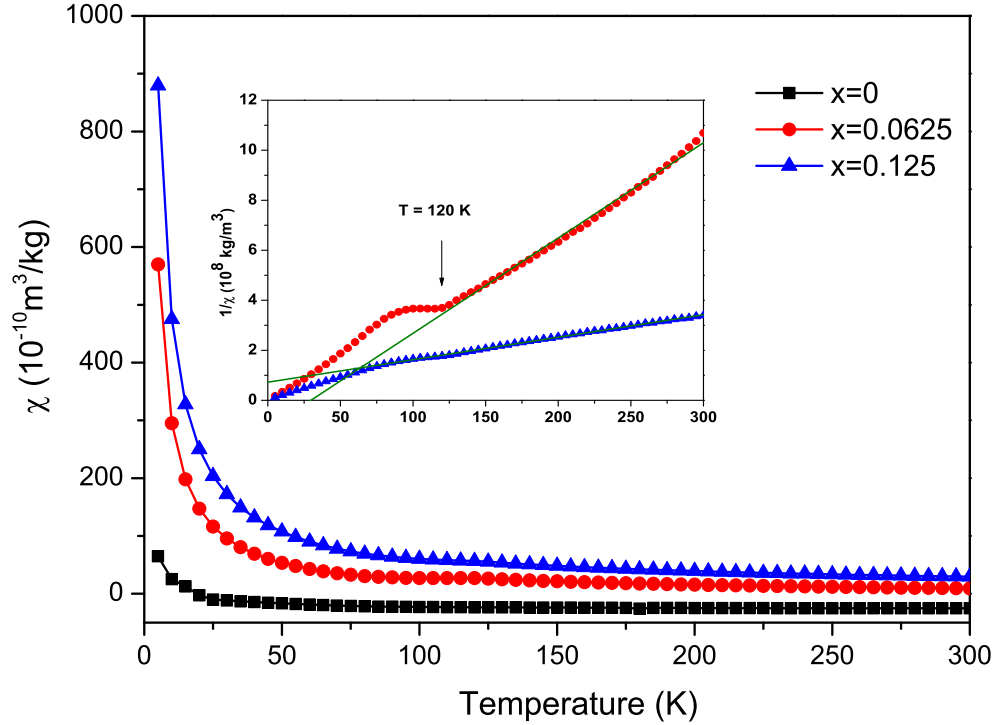


Figure 3.8: Magnetic susceptibility  $\chi$  measured at 500 Oe as a function of temperature for  $\text{La}_2\text{Ti}_{2-x}\text{V}_x\text{O}_7$  ( $x = 0, 0.0625$  and  $0.125$ ). The inset shows the temperature evolution of  $1/\chi$  for the doped samples and the Curie-weiss fitting. The temperature dependence of  $1/\chi$  for the pure sample is not included here, which consists of a large diamagnetic component.

at three different temperatures and shown in Fig 3.7. At room temperature and 50 K, it appears that there is a large diamagnetic contribution to the magnetization of the pure LTO sample and as temperature is decreased to 5 K, a paramagnetic behaviour with a weak contribution from a ferromagnetic-like order is observed. This weak ferromagnetic component is probably induced by the oxygen vacancies formed on the surface of the powder [49]. Surprisingly, all the doped samples are dominated by a typical paramagnetic behaviour and no any ferromagnetic contribution is visible.

The temperature dependence of the magnetic susceptibility is shown in Fig 3.8. As can be seen, the magnetic susceptibility increases with doping concentration; the inverse susceptibility for the doped samples shows a non-linear dependence of temperature  $\chi$  and a turning point at 120 K, suggesting that a magnetic order rather than the simple Curie paramagnetism exists in the doped samples. This weak magnetic order is likely an antiferromagnetism or only partial or short range ferromagnetism, as suggested from the Curie-weiss fitting of the high temperature reverse susceptibility data.

We note that according to [41] wherein the multiferroicity in  $\text{La}_2\text{Ti}_{2-x}\text{V}_x\text{O}_7$  system is predicted, only when the V clusters in dimers or chains in direction  $a$  can long range ferromagnetic order be formed; and V chains and dimers are only stable below an intermediate temperature  $T$  for low doping: for  $x = 0.0625$ ,  $T \sim 900$  K, and for  $x = 0.125$ ,  $T < 1273$  K. Our doped samples with the above doping concentrations were heated at 1273 K and quenched to room temperature, so the high temperature phase was stuck and this phase is a vanadium monomer phase (isolated phase) which is actually not expected to exhibit a strong long range ferromagnetic order [41]. Collapse of the chain in direction  $a$  into monomer phase is evidenced by the abnormal increase of lattice parameter  $a$  as seen from Fig 3.6.

### 3.3 Conclusion

$\text{La}_2\text{Ti}_{2-x}\text{V}_x\text{O}_7$  ( $x = 0, 0.0625, 0.125$  and  $0.25$ ) was synthesized by a conventional solid state reaction and a vacuum annealing plus water quenching method respectively. XRD pattern show that only the doped sample with  $x$  up to 0.125 synthesized by a vacuum annealing plus water quenching method is of a single phase same to the undoped  $\text{La}_2\text{Ti}_2\text{O}_7$ , indicating that vanadium is successfully doped into  $\text{La}_2\text{Ti}_2\text{O}_7$  by the latter method. The magnetic properties of the single phase doped samples were studied by a SQUID magnetometer and compared with that of undoped  $\text{La}_2\text{Ti}_2\text{O}_7$ . The results reveal however a primary paramagnetic-like behaviour and a weak magnetic order rather than the expected ferromagnetic order for the doped samples, which is explained by a vanadium monomer phase formed at the high synthesis temperature. It is thereby demonstrated that the prediction of the phase diagram of vanadium phase in  $\text{La}_2\text{Ti}_{2-x}\text{V}_x\text{O}_7$  [41] is valid at high temperatures.

# Chapter 4

## Oxygen isotope substitution effect on magnetism in multiferroic $\text{CaMn}_7\text{O}_{12}$

### 4.1 Introduction

$\text{CaMn}_7\text{O}_{12}$  has been under investigation for almost 40 years [50]. Recently, a giant improper FE polarization of magnitude  $2870 \mu\text{Cm}^{-2}$  induced by an incommensurate helical magnetic structure was reported in this material below 90 K [51] and this value sets a record for magnetism driven ferroelectricity to date.

As one of the phases in Ca-Mn-O system,  $\text{CaMn}_7\text{O}_{12}$  is reported to be a mixed valence perovskite manganite of the type  $\text{AC}_3\text{B}_4\text{O}_{12}$ . Its chemical formula can be written as  $(\text{Ca}^{2+}\text{Mn}_3^{3+})(\text{Mn}_4^{3.25+})\text{O}_{12}^{2-}$  at room temperature [52] and as  $(\text{Ca}^{2+}\text{Mn}_3^{3+})(\text{Mn}_3^{3+}\text{Mn}^{4+})\text{O}_{12}^{2-}$  below 250 K due to an isostructural charge-ordering transition [53]. The structure is cubic (lattice constant  $a \approx 7.35 \text{ \AA}$ ) with space group  $\text{Im}\bar{3}$  above 440 K and distorts into a rhombohedral structure (lattice constant  $a \approx 10.44 \text{ \AA}$  and  $c \approx 6.34 \text{ \AA}$ ) with space group  $\text{R}\bar{3}$  below 440 K [52, 53] (see Fig 4.1). Two magnetic phase transitions are found at  $T_{N1} = 90 \text{ K}$  and  $T_{N2} = 48 \text{ K}$  [54, 55] respectively and  $T_{N1}$  corresponds to the onset of a giant FE polarization indicating the FE polarization is of magnetic origin [56]. Both low temperature phases

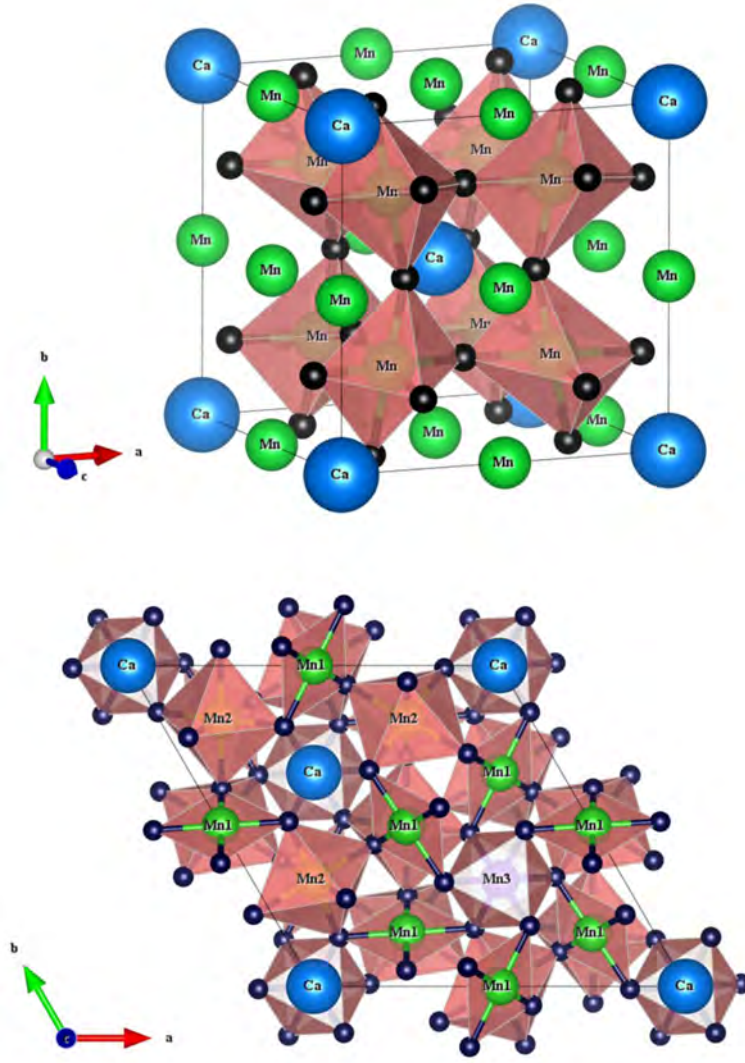


Figure 4.1: The crystal structure of  $\text{CaMn}_7\text{O}_{12}$  (Top:  $\text{Im}\bar{3}$ ; bottom:  $\text{R}\bar{3}$ ) created using the VESTA program [39]. Mn1 denotes  $\text{Mn}^{3+}$  of C in an  $\text{AC}_3\text{B}_4\text{O}_{12}$  formula surrounded by four oxygen atoms forming a plane; Mn2 (Mn3) denotes  $\text{Mn}^{3+}$  ( $\text{Mn}^{4+}$ ) of B which is in an octahedral environment of oxygen.

have incommensurate helical magnetic structures; for  $T_{N2} < T < T_{N1}$ , it is described by the propagation vector  $\mathbf{k}_1 = (0,1,0.0963)$  and for  $T < T_{N2}$   $\mathbf{k}_2 = \mathbf{k}_1 - (0,0, \delta)$  and  $\mathbf{k}_3 = \mathbf{k}_1 + (0,0, \delta)$ , where  $\delta$  is a temperature dependent value [51].

Surprisingly, the FE polarization is found to be perpendicular to the spin rotation planes, quite different from that expected by a KNB model or the inverse DM model where FE polarization lies in the spin rotation plane, which implies that both of these two traditional models seem not applicable to this material. However it could be argued that this does not necessarily

mean that the role of ionic displacement or electronic structure in inducing FE polarization can then be ruled out since these factors might work in combination with others to yield a satisfactory material-specific explanation. Based on their theoretical calculation, Lu *et al.* recently suggested that this large FE polarization can be induced by a combination effect of DM interaction and exchange striction, wherein the magnitude of the polarization is governed by the exchange striction however the direction of the polarization by the chirality of the helical magnetic structure [57], compared to the ferroaxial coupling mechanism proposed in [51] in which both the magnitude and direction are determined by the chirality of the helical magnetic structure. Therefore the underlying physics of  $\text{CaMn}_7\text{O}_{12}$  is still not yet understood and it is essential to develop a method which may shed light on probing those factors inducing the multiferroicity and sorting out a reasonable model.

To understand the microscopic mechanism of the coexistence and coupling of magnetism and ferroelectricity in  $\text{CaMn}_7\text{O}_{12}$ , an idea explored here is to investigate the effect of isotopic substitution of oxygen  $^{16}\text{O}$  by  $^{18}\text{O}$  on the magnetic properties and hence the electric polarization. Isotopically pure oxygen substitution is a widely used technique for the investigation of magnetoresistive systems and high temperature superconductors. To name but a few, giant oxygen-isotope effect on the bulk magnetic properties was observed in the magnetoresistive perovskite  $\text{La}_{1-x}\text{Ca}_x\text{MnO}_{3+y}$  and it provides evidence that lattice distortions are responsible for the magnetoresistive properties [58]; Large oxygen-isotope effect on the bulk magnetic properties was found in  $\text{Sr}_{0.4}\text{K}_{0.6}\text{BiO}_3$  which demonstrates superconductivity is phonon-mediated for this material system [59]. Many improper multiferroics are found to be oxides which are readily available with  $^{16}\text{O}$  since the natural abundance of  $^{16}\text{O}$  is 99.63% and it is possible to replace the  $^{16}\text{O}$  with isotopic pure  $^{18}\text{O}$  in the samples and then compare the two. However, to the best of our knowledge, so far no publications are available on the effect of isotopic substitution on magnetism in multiferroic materials. It is expected that nature of multiferroic coupling may be clarified from an  $^{18}\text{O}$  substitution experiment.

In this study,  $\text{CaMn}_7\text{O}_{12}$  was synthesized successfully by a flux method and an  $^{18}\text{O}$  substitution experiment was subsequently performed on the sample.

The effect of the  $^{18}\text{O}$  substitution on the crystal structure and magnetism were studied by XRD and a SQUID magnetometer, respectively.

## 4.2 Synthesis of $\text{CaMn}_7\text{O}_{12}$

### 4.2.1 Synthesis

Different methods, including the flux method, solid state reactions and the sol-gel method, were trialled to prepare single phase  $\text{CaMn}_7\text{O}_{12}$ . The best sample was obtained using the flux method. To assess the sample quality, the morphology, composition, crystal structure and magnetic properties were studied using scanning electron microscope (SEM), energy dispersive X-ray spectroscopy (EDX), x-ray diffraction (XRD), respectively.

The synthesis process of the flux method followed here was similar to that reported in [51]. A 10 g mixture of  $\text{CaCl}_2$  (99.99% pure, Aldrich) and  $\text{MnO}_2$  (99.99% pure, Aldrich) with a weight ratio of 1:3 was ground manually for 1 hour in an agate mortar and then heated in a high-alumina crucible (99.8% pure, Coorstek) in air at 850 °C in a box furnace for 24 h followed by cooling to room temperature at a rate of 6 °C/h. The reaction product was washed thoroughly with distilled water, to remove the possible remaining overdose  $\text{CaCl}_2$  flux, and then with ethanol and finally dried at 70 °C in an oven.

The resulting shiny sample was found to consist of primarily cubic crystals and a small amount of needle-like structure phase under a preliminary optical microscope investigation, indicating the formation of a second phase during the heat treatment. To remove the needle-like structure, a purification process was carried out. Firstly, the sample was dipped in 36 wt% hydrochloric acid for 10 min, washed and dried as above; then, the big crystals were sorted out by a 90- $\mu\text{m}$  sieve.

### 4.2.2 Morphology and composition

The morphology and composition of the sample was characterised by SEM (Hitachi TM3000) and an EDX system (Bruker Quantax 70) equipped on

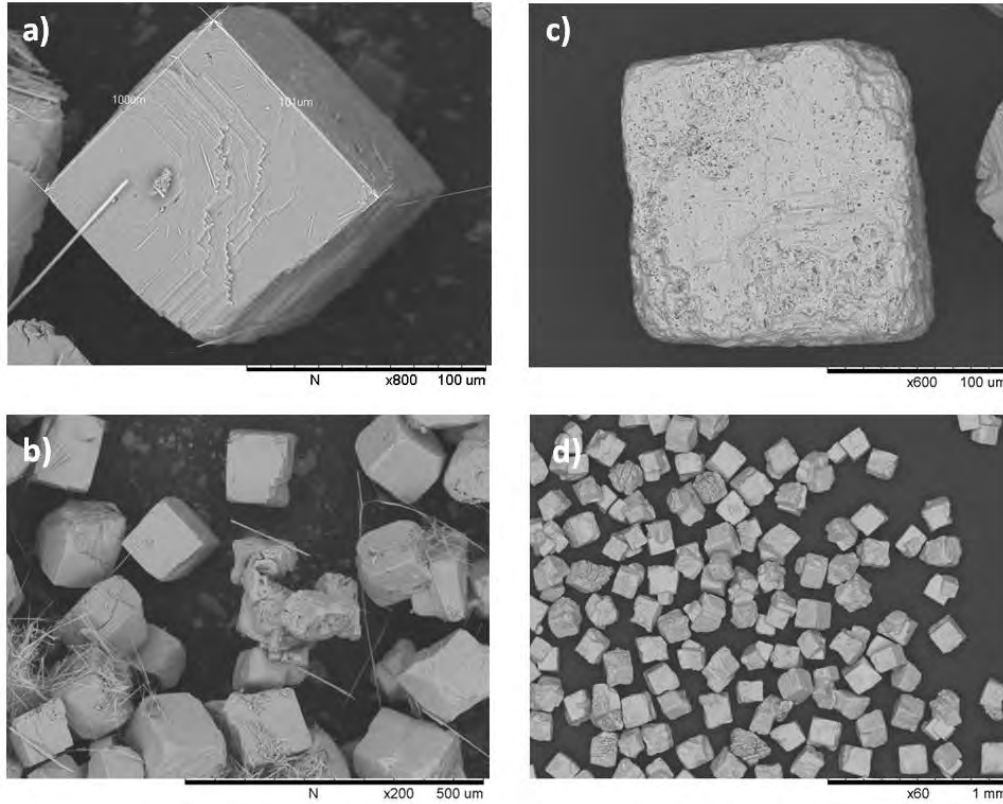


Figure 4.2: SEM image of the sample before (panels a) and b)) and after (panels c) and d)) purification.

the SEM, respectively. To verify the crystal structure, some of the purified crystals were ground into intermediate powder and investigated via XRD measured with Cu  $K\alpha$  radiation on a Bragg-Brentano type powder diffractometer (Sietronics). XRD data of the purified sample was refined by Rietveld method using the *Fullprof* software package.

Table 4.1: Chemical composition of  $\text{CaMn}_7\text{O}_{12}$  measured by EDX.

No.	As prepared (in at%)			After purification (in at%)		
	Ca	Mn	O	Ca	Mn	O
1	6.52	25.28	60.86	5.26	30.68	64.06
2	5.36	25.60	56.30	5.47	29.74	64.79
3	5.42	27.81	58.82	4.68	27.60	67.72
4	5.92	32.03	57.57	5.06	32.57	62.37
5	5.40	28.58	60.06	5.24	30.21	64.54
6	4.78	22.76	67.38	5.40	32.06	62.54
7	5.29	27.81	60.49	4.96	27.84	67.19
8	10.27	44.28	32.84	5.18	32.15	62.67
Average of Mn:Ca		4.85 $\pm$ 0.54		5.89 $\pm$ 0.32		

As can be seen from Fig 4.2 a) and b), the sample before purification contains two crystalline phases: cubic shaped crystals with edge size of about  $100 \sim 150 \mu\text{m}$  as the main phase and needle-like crystals with a diameter of about  $0.2 \sim 2 \mu\text{m}$  as the minor phase. The cubic crystals are characterised by smooth surfaces, sometimes with layered structures on the top. The needle-like crystals are also found lying or embedded in the surface of cubic crystals, except for the independent ones, revealing a possible simultaneous growth for both of these two phases locally. After the purification, the needle-like crystals are not observed anymore (see Fig 4.2 c) and d)) and the surface of cubic crystals becomes rough, showing that the needle-like crystals (as well as some portion of the external surface of the cubic crystals) have been removed successfully, at least from the perspective of SEM observation.

EDX measurements were performed on eight different selected cubic crystals and one needle-like crystals rich area for the sample before purification and eight different cubic crystals for the purified sample. The eight atomic compositions were averaged to give the Mn:Ca ratio for the respective sample. It was found that before purification, the cubic crystals and the needle-like crystals have a Mn:Ca ratio of  $4.85 \pm 0.54$  and  $2.06$  respectively. The composition of the main phase deviates from the expected ratio of 7, which may be explained from the existence of the Ca-rich needle-like crystals on the surface and even possibly within the body of cubic crystals. The EDX result indicates that the needle-like phase is probably  $\text{CaMn}_2\text{O}_4$ . After purification, Mn:Ca ratio of the cubic crystals increases to  $5.89 \pm 0.32$  due to the removal of Ca-rich needles. However it is still less than the nominated ratio, possibly due to the remanence of impurity phase within the cubic body that cannot be removed by the current purification process.

### 4.2.3 Crystal structure

The Rietveld analysis on the XRD data of the purified sample is presented in Fig 4.3. The structural model of  $\text{CaMn}_7\text{O}_{12}$  was created in space group of  $R\bar{3}$  and the atomic positions were referred to that reported in [60]. The crystallographic parameters obtained and agreement factors are summarized in Table 4.2. It can be seen that calculated pattern fits well with

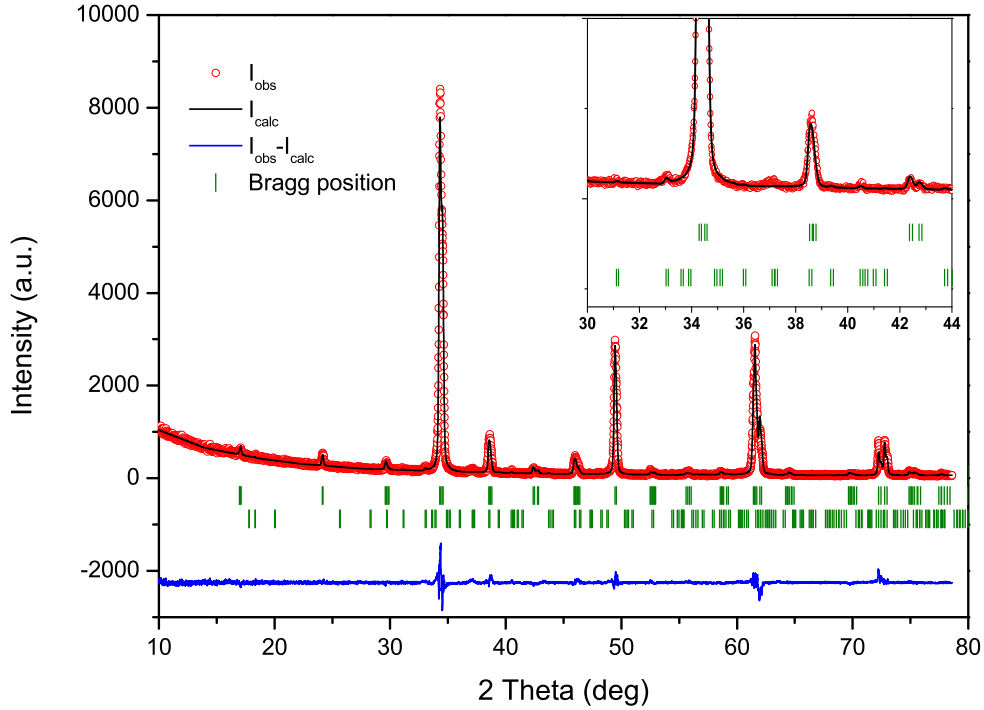


Figure 4.3: Results of the Rietveld refinement of the XRD pattern of  $\text{CaMn}_7\text{O}_{12}$  measure at room temperature. The red points denote measured data; the black line is the calculated pattern. The top tickmarks represent the Bragg peaks for  $\text{CaMn}_7\text{O}_{12}$  while the below ones for the impurity phase  $\text{CaMn}_2\text{O}_4$ . The difference curve is shown as a blue line at the bottom. The inset shows the fit of  $\text{CaMn}_2\text{O}_4$  peaks.

Table 4.2: Summary of refined crystallographic information for  $\text{CaMn}_7\text{O}_{12}$ .

Composition	$\text{CaMn}_7\text{O}_{12}$
Space group	$R\bar{3}$
$a = b$ ( $\text{\AA}$ )	10.45252(14)
$c$ ( $\text{\AA}$ )	6.34237(8)
$V$ ( $\text{\AA}^3$ )	600.101(13)
Calculated density ( $\text{g/cm}^{-3}$ )	5.119
$\chi^2$ , $R_p$ , $R_{wp}$	2.58, 20.5%, 17.6%

the main observed peaks, and the refined lattice constants are quite close to the data reported previously [52, 53], indicating that the main phase is  $\text{CaMn}_7\text{O}_{12}$ . A small amount (1.4 wt%) of  $\text{CaMn}_2\text{O}_4$  impurities were also allowed in the Rietveld analysis as can be seen from the inset. A broad peak at  $\sim 37^\circ$  cannot be fitted well although there are reflections from  $\text{CaMn}_2\text{O}_4$ . This could potential arise from the existence of preferred orientation of grains within this phase or from another Ca-Mn-O phase.

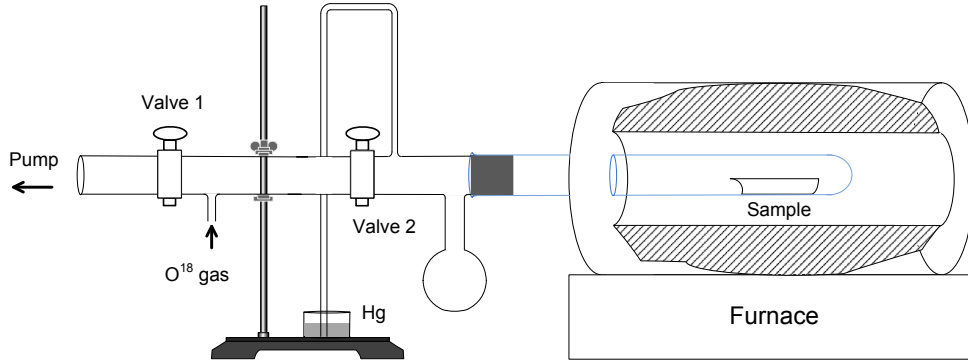


Figure 4.4: The experimental set-up for oxygen 18 substitution.

## 4.3 Oxygen substitution effect on magnetism

### 4.3.1 Oxygen substitution experiment

A furnace with a controlled gas environment was set-up within UNSW Canberra to perform exchange of naturally occurring  $^{16}\text{O}$  with isotopic  $^{18}\text{O}$  in samples (see Fig 4.4). The gas pressure within this apparatus is indicated by a mercury column.  $\text{CaMn}_7\text{O}_{12}$  single crystals were crushed and ground into fine powders in an agate mortar for 30 minutes. A powder sample of 0.4451 g was then placed in a high-alumina boat and the aggregate weight was recorded before loading into a quartz tube. After joining the quartz tube, the exchange apparatus was pumped to high vacuum of  $\sim 76$  cm on the Hg column. Valve 1 (see Fig 4.4) was closed in order to separate the exchange apparatus from the pump. The quartz tube with the sample was subsequently slowly heated to  $500\text{ }^\circ\text{C}$  at a ramp rate of  $8\text{ }^\circ\text{C}/\text{min}$ , held for 15 minutes during which time  $^{18}\text{O}$  gas was slowly loaded into the tube until the Hg column dropped to 34 cm. Valve 2 was then shut down and the furnace was increased to  $850\text{ }^\circ\text{C}$  at a rate of  $6\text{ }^\circ\text{C}/\text{min}$  and finally held for 7 days to allow for oxygen exchanging. After this, the furnace was cooled down to room temperature at a rate of  $5\text{ }^\circ\text{C}/\text{min}$ . The boat with the sample was taken out and carefully weighed for the purpose of further analysis.

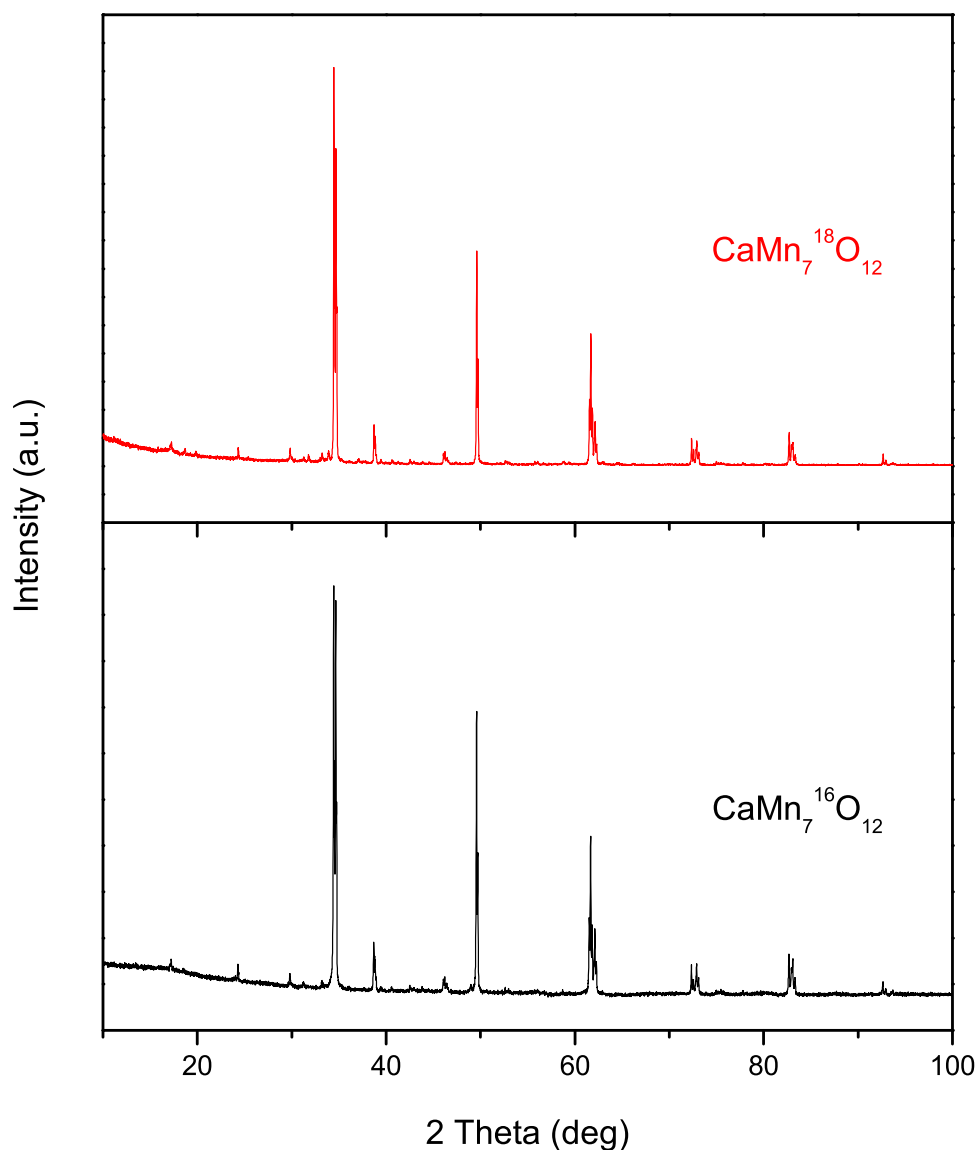


Figure 4.5: XRD pattern of  $\text{CaMn}_7\text{O}_{12}$  before and after oxygen isotope substitution.

### 4.3.2 Crystal structure

Crystal structure of the specimen after oxygen isotope exchange (hereafter labeled as  $\text{CaMn}_7^{18}\text{O}_{12}$ ) was measured using a PANalytical Empyrean X-ray diffractometer with Cu  $K\alpha$  radiation and compared with that of its counterpart  $\text{CaMn}_7^{16}\text{O}_{12}$  in Fig 4.5. No obvious change in crystal structure was observed after oxygen isotope exchange, suggesting that the phase is stable when oxygen exchange takes place at 850 °C. A slight increase of the impurity phase  $\text{CaMn}_2\text{O}_4$  is observed and the amount is estimated to be not more than 5%.

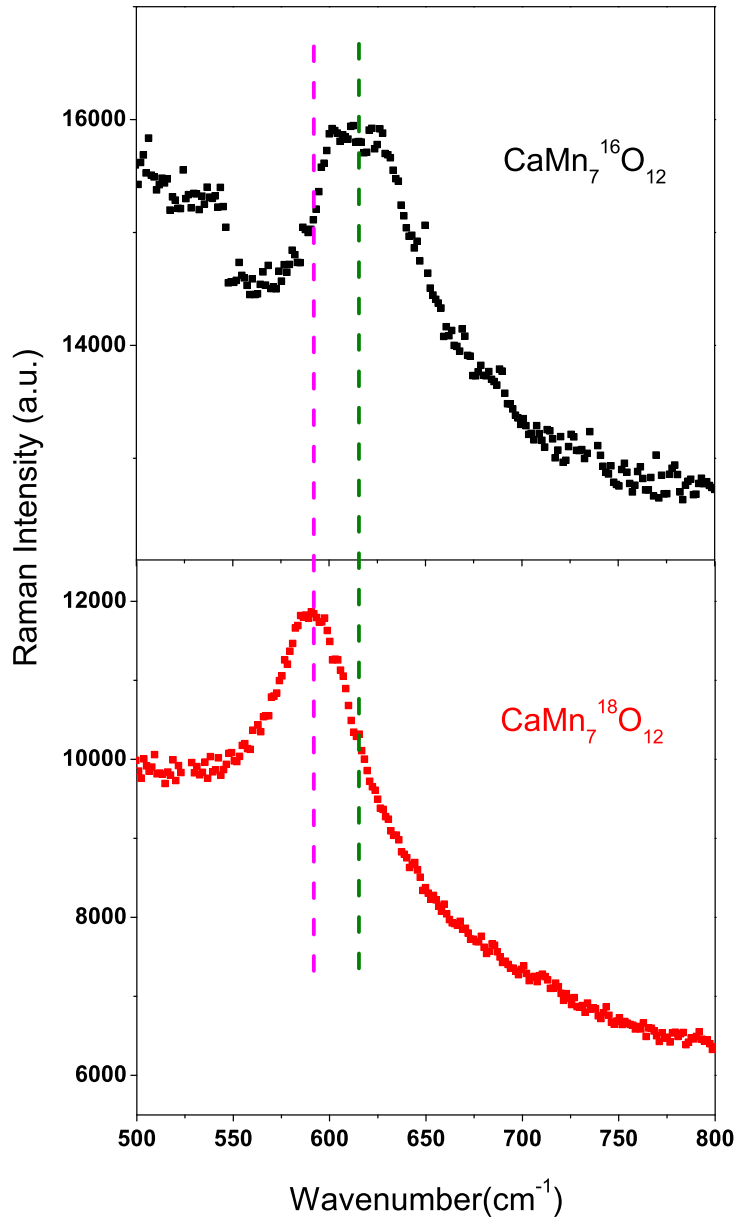


Figure 4.6: Raman spectra of  $\text{CaMn}_7\text{O}_{12}$  before and after oxygen isotope substitution. Two dashed vertical lines at the centre of each peak are also drawn as a guide to eyes. The step seen to the left of the main peak of  $\text{CaMn}_7^{16}\text{O}_{12}$  are also assigned to oxygen modes but they are not well resolved (see text).

### 4.3.3 Determination of $^{18}\text{O}$ content

To estimate the  $^{18}\text{O}$  content of the  $\text{CaMn}_7^{18}\text{O}_{12}$  sample, Raman spectra were recorded for  $\text{CaMn}_7^{18}\text{O}_{12}$  and  $\text{CaMn}_7^{16}\text{O}_{12}$  on the Micro-Raman System at Australian National University. Both samples were pressed into pellets and each measurement was carried out for 30 min in a reflection

mode using a 532 nm laser excitation at room temperature. The Micro-Raman System was calibrated before each measurement using the  $F_{1g}$  line of Si at  $520.2 \text{ cm}^{-1}$  as a reference. The signal-to-noise ratio was found to be low for both spectra, reflecting low power and short time used for the measurements. However a characteristic peak at  $\sim 600 \text{ cm}^{-1}$  was clearly visible for both spectra (see Fig 4.6) and can be used to estimate the  $^{18}\text{O}$  content. This peak is assigned to the  $E_g$  mode of oxygen atom. After oxygen isotope exchange, the peak width decreases and the peak shifts to the left by a wavenumber of  $\sim 24 \text{ cm}^{-1}$ . This shift is a sign that heavier  $^{18}\text{O}$  is present in the sample [61]. Since for vibration modes of pure  $^{16}\text{O}$  and  $^{18}\text{O}$ , the Raman shift  $v_{16}$  and  $v_{18}$  have the relation [61],

$$\frac{v_{18}}{v_{16}} = \sqrt{\frac{m_{16}}{m_{18}}}, \quad (4.1)$$

where  $m_{16}$  and  $m_{18}$  are the atomic weight of  $^{16}\text{O}$  and  $^{18}\text{O}$  respectively. Assuming the atomic concentration of  $^{18}\text{O}$  is  $x$ ,

$$\frac{v}{v_{16}} = \sqrt{\frac{m_{16}}{m}} = \sqrt{\frac{m_{16}}{m_{16} + (m_{18} - m_{16})x}}, \quad (4.2)$$

where  $v$  and  $m$  are the Raman shift and average oxygen mass of  $\text{CaMn}_7^{18}\text{O}_{12}$  respectively. The concentration was found to be 61%, agreeing well with that estimated from the mass difference before and after oxygen isotope substitution, i.e.,  $\sim 64\%$ , and is comparable to the 77% concentration we observed for  $\text{o-DyMn}^{18}\text{O}_3$  which was also prepared in one heating cycle [62]. Comparing with the higher temperature ( $1200 \text{ }^\circ\text{C}$ ) and longer time (14 days) used for  $\text{o-DyMnO}_3$  to achieve this level of  $^{18}\text{O}$  concentration, the heating process we used for  $\text{CaMn}_7\text{O}_{12}$  is milder. This suggests perhaps that the oxygen isotope exchange proceeds more readily for  $\text{CaMn}_7\text{O}_{12}$  than for  $\text{o-DyMnO}_3$ .

### 4.3.4 Magnetic properties

Magnetization was recorded for both samples within the temperature interval of  $5 \sim 300 \text{ K}$  in field-cooled (FC) and zero field-cooled (ZFC) mode respectively in a magnetic field of 1000 Oe using a SQUID magnetometer and plotted in Fig 4.7. For both samples, the two characteristic magnetic

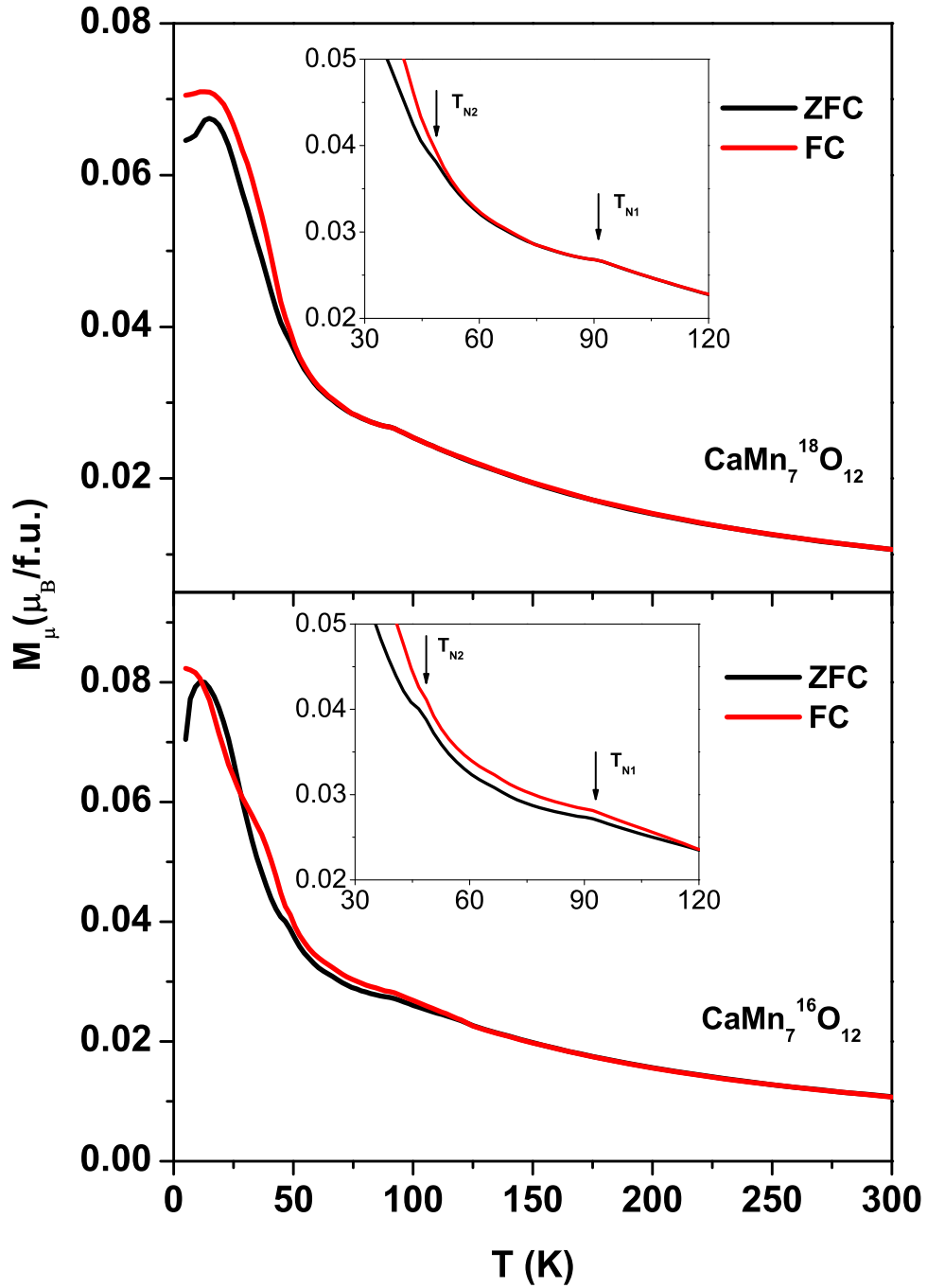


Figure 4.7: Temperature evolution of magnetization of  $\text{CaMn}_7^{16}\text{O}_{12}$  and  $\text{CaMn}_7^{18}\text{O}_{12}$ . The insets show the magnetic transition points.

transition points, one at  $T_{N1} \sim 90$  K and other at  $T_{N2} \sim 47$  K, as well as the low temperature spin glass like phase of  $\text{CaMn}_7\text{O}_{12}$  can be observed. This is consistent with the earlier crystal structure measurements and also supports the premise that both samples have the same phase.

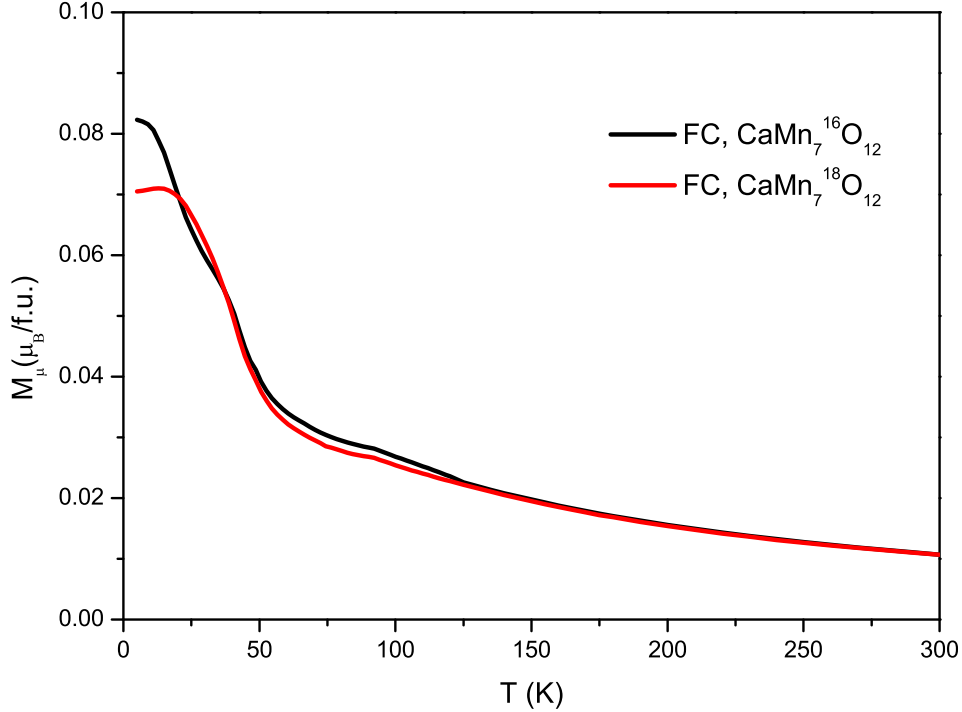


Figure 4.8: Compare the temperature evolution of magnetization of  $\text{CaMn}_7^{16}\text{O}_{12}$  and  $\text{CaMn}_7^{18}\text{O}_{12}$  taken in field cooled mode.

Nevertheless, two samples have different responses to the magnetic field. We first discuss the magnitude of the magnetic moments. Interestingly, as can be seen from Fig 4.8, the  $\text{CaMn}_7^{18}\text{O}_{12}$  has smaller magnetization for  $50 < T < 120$  K and  $T < 20$  K. More importantly, two magnetic transitions fall in the temperature interval  $50 < T < 120$  K wherein FE polarization develops. This appears to be a direct evidence that oxygen is related to the magnetic properties and hence the FE polarization of this material system. According to the inverse DM theory, the canting of the existing spins may cause displacement of the ion (usually O) bonding the spin sites in order to generate a new DM vector. The local FE polarization can therefore be resulted with a direction opposite to the ionic displacement. The heavier oxygen isotope might reduce the extent of canting of the spins by displacing a smaller distance compared with its lighter counterpart, subsequently leading to a smaller net magnetic moment as observed here. There is however another factor that we can not ignore, that is, two samples have different divergence temperatures. For  $\text{CaMn}_7^{16}\text{O}_{12}$ , FC and ZFC curves diverge at  $\sim 120$  K, while for  $\text{CaMn}_7^{18}\text{O}_{12}$ , the divergence temperature is  $\sim 50$  K, the latter being consistent with that of the powder and single crystal  $\text{CaMn}_7^{16}\text{O}_{12}$  reported in the literature [51]. This difference is obviously not

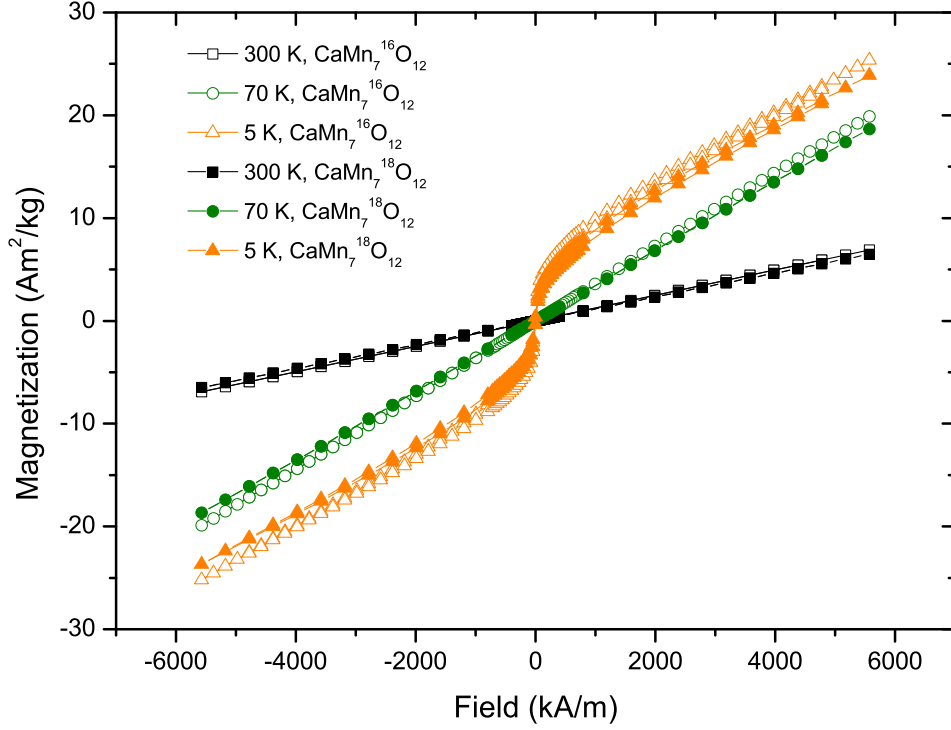


Figure 4.9: Hysteresis loops of  $\text{CaMn}_7^{16}\text{O}_{12}$  and  $\text{CaMn}_7^{18}\text{O}_{12}$ .

an effect of the presence of  $^{18}\text{O}$ ; it is not likely to arise from impurities either since the impurity amount of  $\text{CaMn}_7^{18}\text{O}_{12}$  is seen in the XRD pattern to be even larger than that of  $\text{CaMn}_7^{16}\text{O}_{12}$ . It is noted that the low temperature ( $T < 50$  K) behaviour of  $\text{CaMn}_7^{16}\text{O}_{12}$  is very similar to that of single crystal  $\text{CaMn}_7\text{O}_{12}$  [51]. Since the  $\text{CaMn}_7^{16}\text{O}_{12}$  powder used in the magnetization measurement was crushed from single crystals, the divergence seen at 120 K is perhaps the result of a wider size distribution of the powder. For  $\text{CaMn}_7^{18}\text{O}_{12}$  which underwent a long heat treatment, the crystal size became more homogeneous therefore the sample shows divergence at 50 K. It is not clear whether the change of magnetization observed for  $50 < T < 120$  K is originated from these different divergence temperatures and more experiments are necessary to clarify this point.

Hysteresis loops were also recorded for two samples under magnetic field up to 6000 kA/m for three temperatures: 300, 70 and 5 K. The three selected temperatures represent the three characteristic magnetic phases of  $\text{CaMn}_7\text{O}_{12}$ , i.e., high temperature paramagnetic phase, intermediate temperature antiferromagnetic phase I and low temperature antiferromagnetic phase II. For both samples, the M-H curves show similar shape at every temperature, changing from the room temperature paramagnetic to the

low temperature ferromagnetic-like behaviour. A slight drop in the magnetization is seen for  $\text{CaMn}_7^{18}\text{O}_{12}$  compared with that of  $\text{CaMn}_7^{16}\text{O}_{12}$ . As temperature decreases, the drop amplitude increases, which is consistent with the temperature dependent magnetization measurements.

## 4.4 Conclusion

The multiferroic  $\text{CaMn}_7\text{O}_{12}$  was synthesized successfully by a flux method. The  $^{18}\text{O}$  isotope exchange was subsequently performed on the sample. The  $^{18}\text{O}$  concentration was found to be  $\sim 61$  at.% by Raman Spectroscopy and  $\sim 64$  at.% from the mass difference before and after oxygen isotope substitution. The crystal structure of the sample remains the same after  $^{18}\text{O}$  substitution however smaller magnetization was observed for  $50 < T < 120$  K wherein two characteristic magnetic transitions of  $\text{CaMn}_7\text{O}_{12}$  occur and FE polarization develops. This can be considered as a direct evidence that oxygen is related to the magnetic properties as well as the FE polarization of this material. However different divergence temperatures were also observed which may contribute to this change of magnetization.

# Chapter 5

## Investigation of the order parameter of Pr in the filled skutterudite $\text{PrRu}_4\text{P}_{12}$ by resonant soft x-ray diffraction

### 5.1 Introduction

Filled skutterudites show a large diversity of electronic phenomena including frustrated magnetic ordering, superconductivity and metal-insulator (MI) transitions. For example,  $\text{EuFe}_4\text{As}_{12}$  shows a canted ferromagnetic or ferrimagnetic phase transition [63];  $\text{LaFe}_4\text{P}_{12}$ ,  $\text{LaRu}_4\text{P}_{12}$  and  $\text{LaOs}_4\text{P}_{12}$  are superconductors [64–66]; and  $\text{PrFe}_4\text{P}_{12}$  and  $\text{PrRu}_4\text{P}_{12}$  undergo MI transitions at  $T_{MI} = 6.7$  K and  $T_{MI} = 62.3$  K respectively [67, 68]. Among all the filled skutterudites showing a MI transition,  $\text{PrRu}_4\text{P}_{12}$  perhaps attracts the most attention since the origin of the MI transition is not understood well. A structural phase transition accompanying the MI transition was detected by electron diffraction and synchrotron x-ray diffraction [69, 70]. Weak superlattice peaks at  $(h\ k\ l)$  ( $h + k + l = \text{odd}$ ) appear below the transition temperature and the crystal symmetry reduces from  $\text{Im}\bar{3}$  to  $\text{Pm}\bar{3}$ , leading to two distinct site symmetries for the Pr ions. The fact that no MI transition is observed in  $\text{LaRu}_4\text{P}_{12}$  [71] implies that the Pr 4f electrons have an integral role in the observed changes. The MI transition is believed to

be caused by a charge density wave (CDW) of the conduction electrons due to hybridization with the Pr 4f shells [72]. In spite of this the precise order parameter of the Pr 4f shells remains somewhat elusive. A clear anomaly is observed with specific heat while no sign of magnetic order of Pr ions is observed [73, 74]. Further, X-ray Absorption Near Edge Structure (XANES) at Pr  $L_{2,3}$  edges showed that the electronic state is  $\text{Pr}^{3+}$  and charge order at the Pr sites is not observed [75]. An antiferro type quadrupolar order or hexadecapole order of Pr 4f was reported theoretically for  $\text{PrRu}_4\text{P}_{12}$  in previous studies [76, 77]. RXD at the Pr  $L_{2,3}$  edges through an E1 dipole transition ( $2p \rightarrow 5d$ ) confirmed spatially ordered Pr ions with two different electronic states however no resonant signals were detected in an E2 transition ( $2p \rightarrow 4f$ ) process as expected for the higher multipole order than quadrupole order of 4f shells [78]. Yet recent theoretical work suggested another orbital order, i.e., an ‘antiferro-orbital’ ordered state below  $T_{MI}$  for Pr 4f electrons which comes from a ‘ferro-orbital’ ordered state above  $T_{MI}$  [79].

RXD has proved to be a powerful tool in modern solid state physics to investigate magnetic, orbital and charge ordering phenomena associated with electronic degrees of freedom [33]. The previous work of our group on the rare-earth borocarbides has demonstrated that orbital order up to rank 6 can be observed with resonant soft x-ray diffraction (RSXD) [80, 81]. RSXD at the rare-earth  $M_{4,5}$  edges directly accesses the lanthanide order via the dipolar transition ( $3d \rightarrow 4f$ ). Strong resonant diffraction intensities with distinct energy dependencies have been observed due to orbital order in Dy-, Ho-, and  $\text{TbB}_2\text{C}_2$  [80–83]. This technique is extremely sensitive to the site order of the 4f shell and allows one to distinguish between various order parameters such as charge, magnetic and orbital order via the study of polarization and azimuthal angle (rotation about the wave vector) dependence.

In the present study, we performed SRXD in combination with x-ray absorption spectroscopy (XAS) at the Pr  $M_{4,5}$  edges in  $\text{PrRu}_4\text{P}_{12}$  to probe directly the order parameter of Pr 4f shells. We observed a resonance enhancement of the (100) superlattice reflection at the Pr  $M_{4,5}$  edges below  $T_{MI}$ . Recording and analysing the energy, temperature, polarization and azimuthal angle dependence allows us to determine and characterise

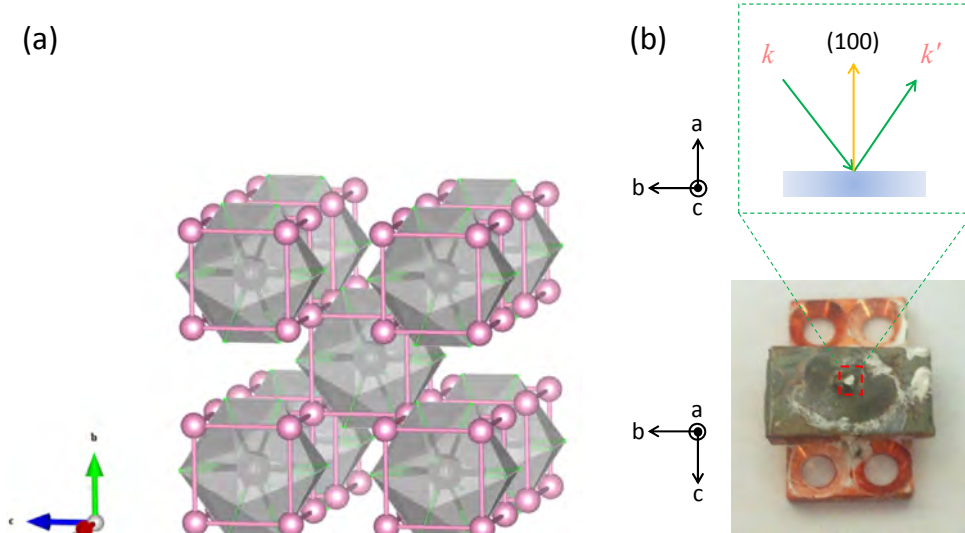


Figure 5.1: (a) The crystal structure of  $\text{PrRu}_4\text{P}_{12}$  in the  $\text{Im}\bar{3}$  phase at room temperature created by VESTA program [39], based on the atomic positional parameters reported in [84]. A Pr atom (denoted as a black ball) is in an icosahedron environment of P atoms (omitted for clarity) and a cubic environment of Ru atoms (denoted as purple balls); Note that below  $T_{MI}$ , the structure changes to  $\text{Pm}\bar{3}$  in which the Ru cube in the centre expands while the Ru cubes surrounding shrink, or vice versa, forming a CDW state and leaving two distinct Pr sites. (b) Lower panel:  $\text{PrRu}_4\text{P}_{12}$  single crystal sample mounted on the stage by silver paste; Upper panel: the scattering geometry.

the possible order parameter associated with the Pr ions below  $T_{MI}$  in  $\text{PrRu}_4\text{P}_{12}$ .

## 5.2 Experimental

$\text{PrRu}_4\text{P}_{12}$  crystallizes in the cubic structure (space group  $\text{Im}\bar{3}$ ) as shown in Fig 5.1 (a).  $\text{PrRu}_4\text{P}_{12}$  single crystals were grown by a tin-flux method [78]. Subsequently, one crystal with an approximate dimension  $500 \times 500 \times 500 \mu\text{m}$  was aligned and polished with the  $a$ -axis perpendicular to the surface. The (100) reflection was recorded at the Pr  $M_{4,5}$  edges at the RESOXS end-station of the SIM beam-line at the Swiss Light Source, with the scattering geometry set up as Fig 5.1 (b). The superlattice peak was fitted with single Lorentzian

$$f(\theta) = \frac{2A}{\pi} \frac{W}{4(\theta - \theta_0)^2 + W^2} + a \quad (5.1)$$

where  $A$  is integrated intensity;  $W$  is Full Width Half Maximum (FWHM);  $\theta_0$  the peak position and  $a$  a constant representing the background.  $A$  and  $W$  were extracted for analysis. The Pr  $M_{4,5}$  XANES were characterized with total electron yield (TEY) at the BL17SU beamline at SPring-8 across a temperature range of  $34 \text{ K} < T < 79 \text{ K}$ . The energy of XANES was calibrated with the Au 4f peak in the photoemission spectroscopic spectra measured by a hemispherical electron analyzer, Scienta SES-2002. The energies of SRXD were subsequently corrected by overlapping the maximum of the energy dependent FWHM in  $\sigma$  polarization to the Pr  $M_5$  edge of the calibrated XANES. The integrated intensity was corrected for absorption by multiplying it by the XANES spectrum measured at 48.4 K.

### 5.3 Results

The (100) reflection is forbidden by the high temperature crystal structure  $\text{Im}\bar{3}$  of  $\text{PrRu}_4\text{P}_{12}$  however allowed by the low temperature crystal structure  $\text{Pm}\bar{3}$ . This superlattice reflection is observed across an energy range of  $900 \sim 970 \text{ eV}$  and a temperature range of  $10 \sim 85 \text{ K}$ . The typical superlattice reflections observed at 10 K for  $\sigma$  polarization and selected energies, and their fittings are shown in Fig 5.2. The experimentally measured integrated intensity of the (100) superlattice reflections as a function of photon energy across the Pr 3d ( $M_{4,5}$ ) thresholds is shown in Fig 5.3. A resonant enhancement of the (100) superlattice reflection was observed at the Pr  $M_{4,5}$  edges below  $T_{MI}$ . The enhancement magnitude, defined as the ratio of the integrated intensity at absorption edges to that at off-edge energies, is approximately 36 for the  $M_5$  edge and 2 for the  $M_4$  edge, respectively. The enhancement at the  $M_5$  edge is 18 times stronger than that at the  $M_4$  and Pr  $L_{2,3}$  edges [78]. The energy dependence of the (100) reflections of  $\text{PrRu}_4\text{P}_{12}$  at 10 K was investigated for both incident linear  $\sigma$  and  $\pi$  polarizations, as shown in Fig 5.3. The energy dependence is similar for both  $\sigma$  and  $\pi$  incoming radiation, except for the large difference in intensity. The satellite structure in the vicinity of the main structure for both of the edges ( $M_5$ : 927 eV;  $M_4$ : 947 eV) is similar to that observed in  $\text{DyB}_2\text{C}_2$  at  $M_{4,5}$  edges [80, 81] and  $\text{NpO}_2$  at the  $M_4$  edge [85]. This structure is ascribed

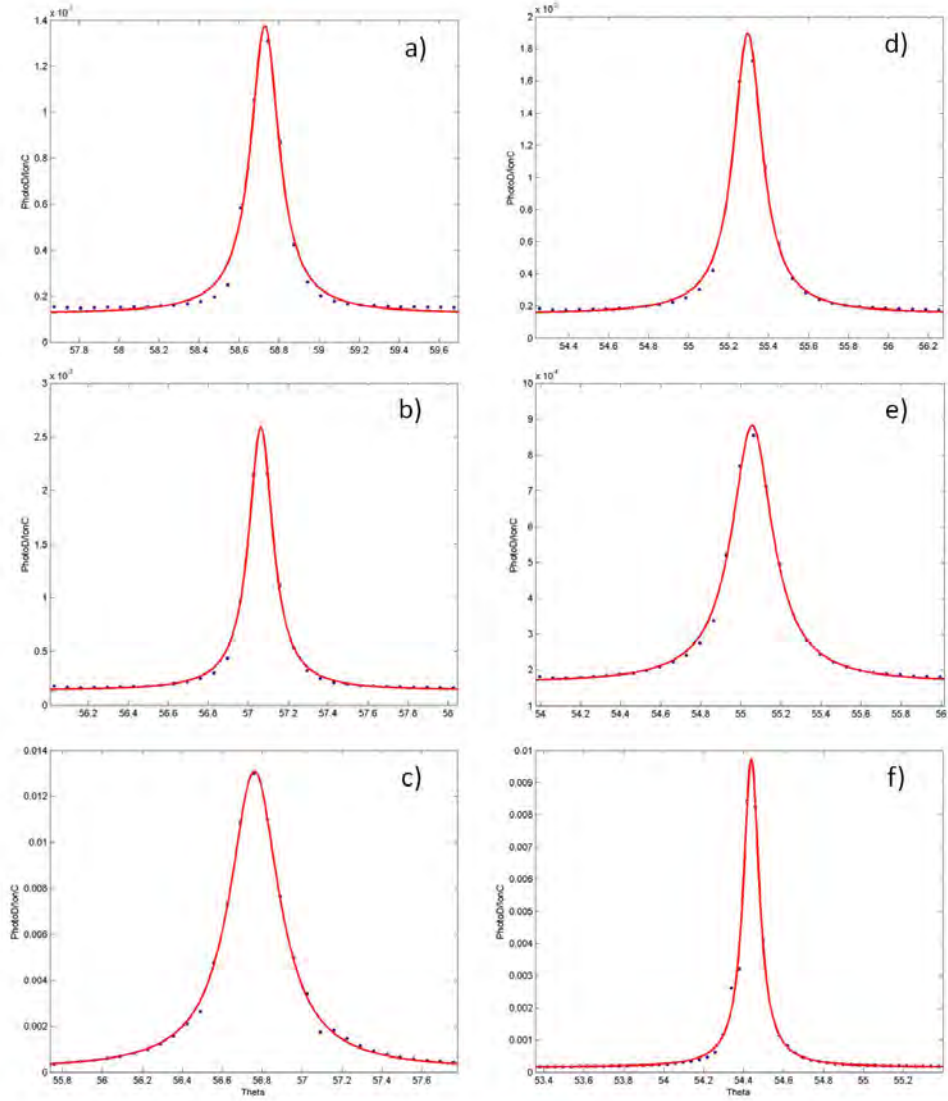


Figure 5.2: The (100) reflection (purple dots) recorded at 10 K for  $\sigma$  polarization and selected energies a) 907 eV, b) 924 eV, c) 927 eV, d) 944 eV, e) 947 eV and f) 967 eV, and their Lorentzian fittings (red lines).

to the splitting of the 3d core states which leads to multiple interfering resonators and subsequently adds structure to the energy profile [80, 81].

The temperature dependence of the square root of the integrated intensity of the (100) reflection for unfocused beams and focused beams of different energies and different incident polarizations is shown in Fig 5.4. Unfocused beams of a near-edge energy (927 eV) and an off-edge energy (917 eV) were chosen to record the superlattice reflection signals in a temperature range  $10 \sim 85$  K, across  $T_{MI}$ ; while focused beams of three near-edge energies

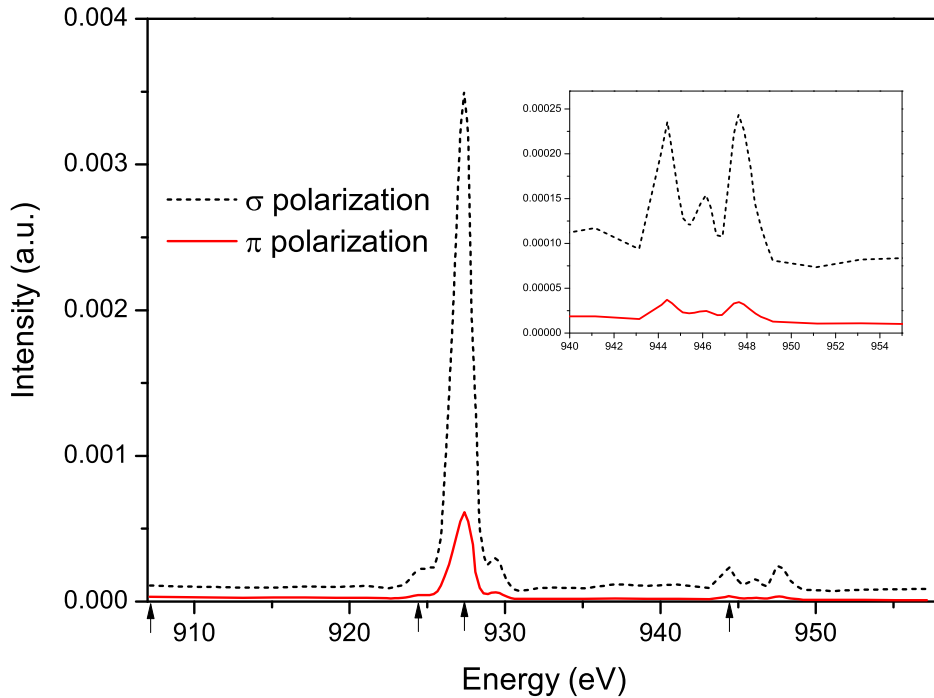


Figure 5.3: The integrated intensity of (100) diffraction after absorption correction as a function of energy. The inset is a magnified figure showing the detailed structure around the  $M_4$  edge, near 947 eV. The arrows denote the energies selected for observations with focused beams.

(924, 927 and 944 eV) and two off-edge energies (907, 967 eV) were selected for observations below  $T_{MI}$ . The reflections at off-edge energies can be explained by lattice distortion, i.e., Ru displacement (P has negligible net contribution to the (100) reflection) [72], as confirmed by the same temperature dependence of the off-edge reflections in this experiment and Ru-ion displacement determined by the nonresonant X-ray diffraction measurements [86, 87]. While the reflections at near-edge energies are expected to have a significant contribution from an order parameter associated with the Pr 4f shells. It is found that the order parameter associated with the Pr 4f shells undergoes a second-order-like transition at  $\sim 62$  K. The transition temperature agrees well with the  $T_{MI}$  and the lattice distortion temperature [68–70]. The transition behaviour is consistent with the previous specific heat measurements where a  $\lambda$ -like second-order-type anomaly was seen at  $T_{MI}$  [73, 88]. Interestingly, we find that below  $T_{MI}$  the (100) reflection shows a steady increase as temperature decreases, independent of energies and incident polarizations. The identical temperature dependence at the near-edge energies and the off-edge energies reveals a single order

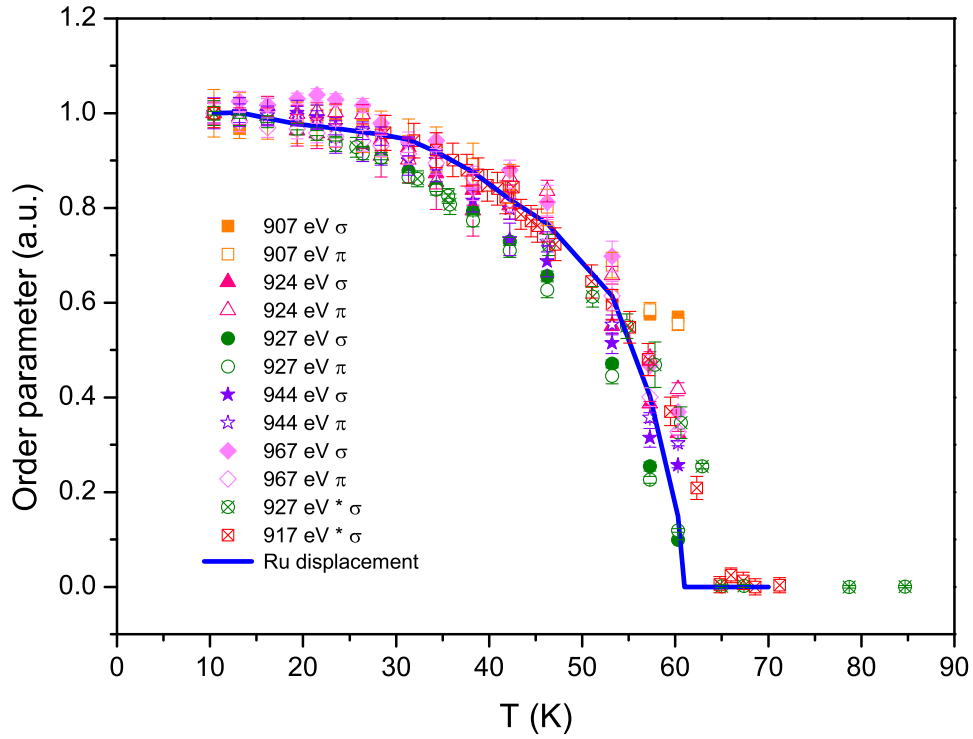


Figure 5.4: The square root of integrated intensity of (100) diffraction normalized at 10 K as a function of temperature. The Ru displacements taken from [86, 87] and interpolated to the measured temperature points are also plotted for a comparison. Two energies marked with asterisks are for unfocused beams while the others are for focused beams.

parameter for Pr, in contrast to  $\text{DyB}_2\text{C}_2$  which shows different temperature dependences of the integrated intensity for different energies reflecting more than one order parameter [80]. It is also evident that the temperature evolution of the resonant signals at the near-edge energies follows that of the Ru-ion displacement [86, 87]. Note that the Ru-ion displacement corresponds to a CDW state with a modulation vector (100) [72], it therefore suggests that the order parameter of Pr and the CDW state of Ru couple closely and evolve in the same manner.

To investigate this order parameter, the (100) superlattice reflection was recorded against different azimuthal angles at 10.4 K with a focused beam for both incident  $\sigma$  and  $\pi$  polarization. The integrated intensity of the reflections for both polarizations were extracted and their ratio  $I_\sigma/I_\pi$  was analyzed and plotted as a function of azimuthal angle (see Figure 5.5). As can be seen, the ratio shows only a small amount of scatter around a constant value with an average of 6.4 over a wide azimuthal angle range (0

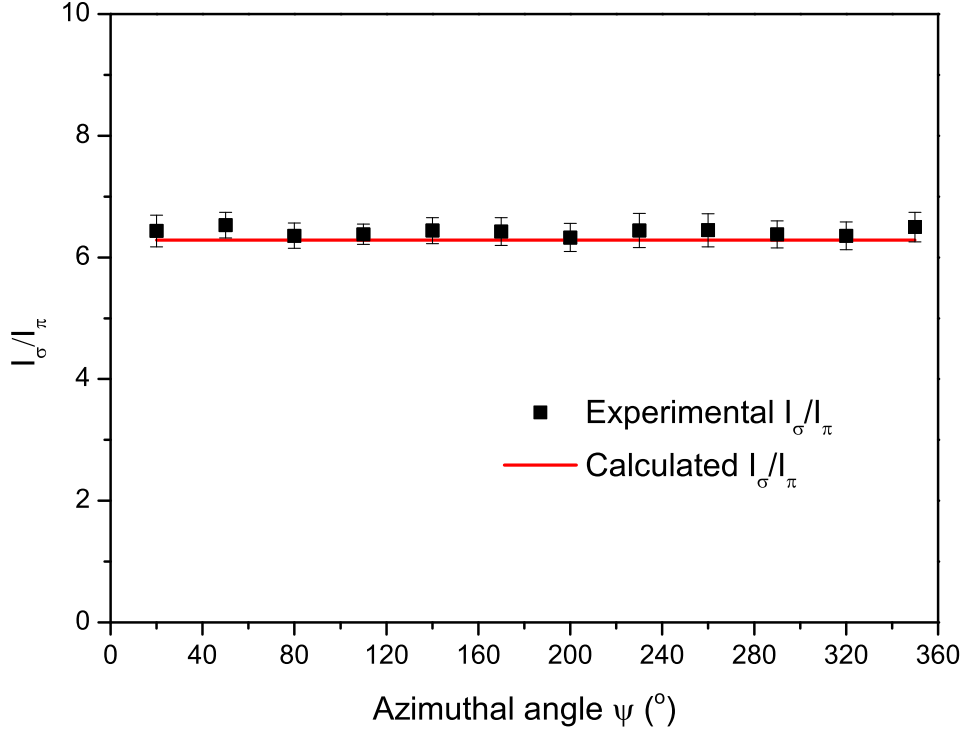


Figure 5.5:  $I_\sigma/I_\pi$  measured with a focused beam at different azimuthal angles. The theoretically calculated  $I_\sigma/I_\pi$  based on the charge order is shown in red line for a comparison.

$< \Psi < 360^\circ$ ) and appears independent of azimuthal angle. A theoretical calculation of  $I_\sigma/I_\pi$  based on charge order was carried out using

$$F = \begin{pmatrix} F_{\sigma'\sigma} & F_{\sigma'\pi} \\ F_{\pi'\sigma} & F_{\pi'\pi} \end{pmatrix} = \begin{pmatrix} 1 & 0 \\ 0 & \cos 2\theta \end{pmatrix} \quad (5.2)$$

and

$$\frac{I_\sigma}{I_\pi} = \frac{F_{\sigma'\sigma}F_{\sigma'\sigma}^* + F_{\pi'\sigma}F_{\pi'\sigma}^*}{F_{\sigma'\pi}F_{\sigma'\pi}^* + F_{\pi'\pi}F_{\pi'\pi}^*}, \quad (5.3)$$

where  $\sigma'$  and  $\pi'$  are the polarization of the scattered X-ray;  $F$  is the form factor and its subscript denotes the channel  $\sigma$ - $\sigma'$ ,  $\pi$ - $\sigma'$ ,  $\pi$ - $\pi'$  and  $\sigma$ - $\pi'$  respectively; and  $\theta$  is the Bragg angle of the superlattice reflection. The calculation yields a constant value of approximately 6.3 which is almost the same to the observed experimental average of 6.4, suggesting the possibility of charge order at Pr sites.

In order to probe the charge state of the sample below  $T_{MI}$ , an XAS measurement was performed. The XAS spectra after energy calibration are displayed in Fig 5.6. These were recorded at six temperatures (two above

and four below  $T_{MI}$ ). The shape of the peaks for  $M_4$  and  $M_5$  edge shows no noticeable change when temperature decreases (see Fig 5.6 b)), constantly indicating features typical of a trivalent state [89]. The small intensity differences in Fig 5.6 a) are likely due to variation of exact spot locations upon cooling, as the incident beam spot size is  $\sim 10 \mu\text{m} \times 30 \mu\text{m}$ . Overall, these data are indicative of stable average Pr valence across the transition temperature, in agreement with a previous Pr  $L_2$  edge XANES study on  $\text{PrRu}_4\text{P}_{12}$  [75].

## 5.4 Discussion

We first discuss the relation between the order parameter associated with Pr 4f electronic states and that of the CDW state of Ru. The temperature evolution of the resonance enhanced signals of (100) at the near-edge energies is found to be similar to that of the CDW state with a wave vector of (100) (see Fig 5.4). This indicates that the order parameter for the Pr 4f electronic states follows that of the CDW state of Ru. The temperature dependence of the order parameter of Pr 4f shells is not hindered by changes in thermal occupancy of the electronic states derived from splitting of the multiplet states due to crystal electric field of the CDW states as observed in [90]. Our results plus previous findings on Ru [87, 91] imply an electronic coupling of the Pr 4f and Ru states which play an important synergistic role in the MI transition.

Next we quantify the possible order parameters associated with the Pr 4f shells below  $T_{MI}$  in  $\text{PrRu}_4\text{P}_{12}$ . The essentially constant RSXD intensities as a function of azimuthal angle in  $\text{PrRu}_4\text{P}_{12}$  preclude magnetic order and/or orbital order which would show an obvious periodic oscillation. Moreover, the intensities observed with the  $\sigma$  polarization are much larger than those using the  $\pi$  polarization (see Fig 5.3), which is opposite to that expected from magnetic order. The lack of indication of magnetic order is consistent with our previous low temperature nuclear orientation study [74]. Therefore the possibility of lattice distortion and charge order is considered.

To model the intensity of the superlattice reflection with lattice distortion of Pr, it is assumed that the Ru displaces as that reported in [75] while

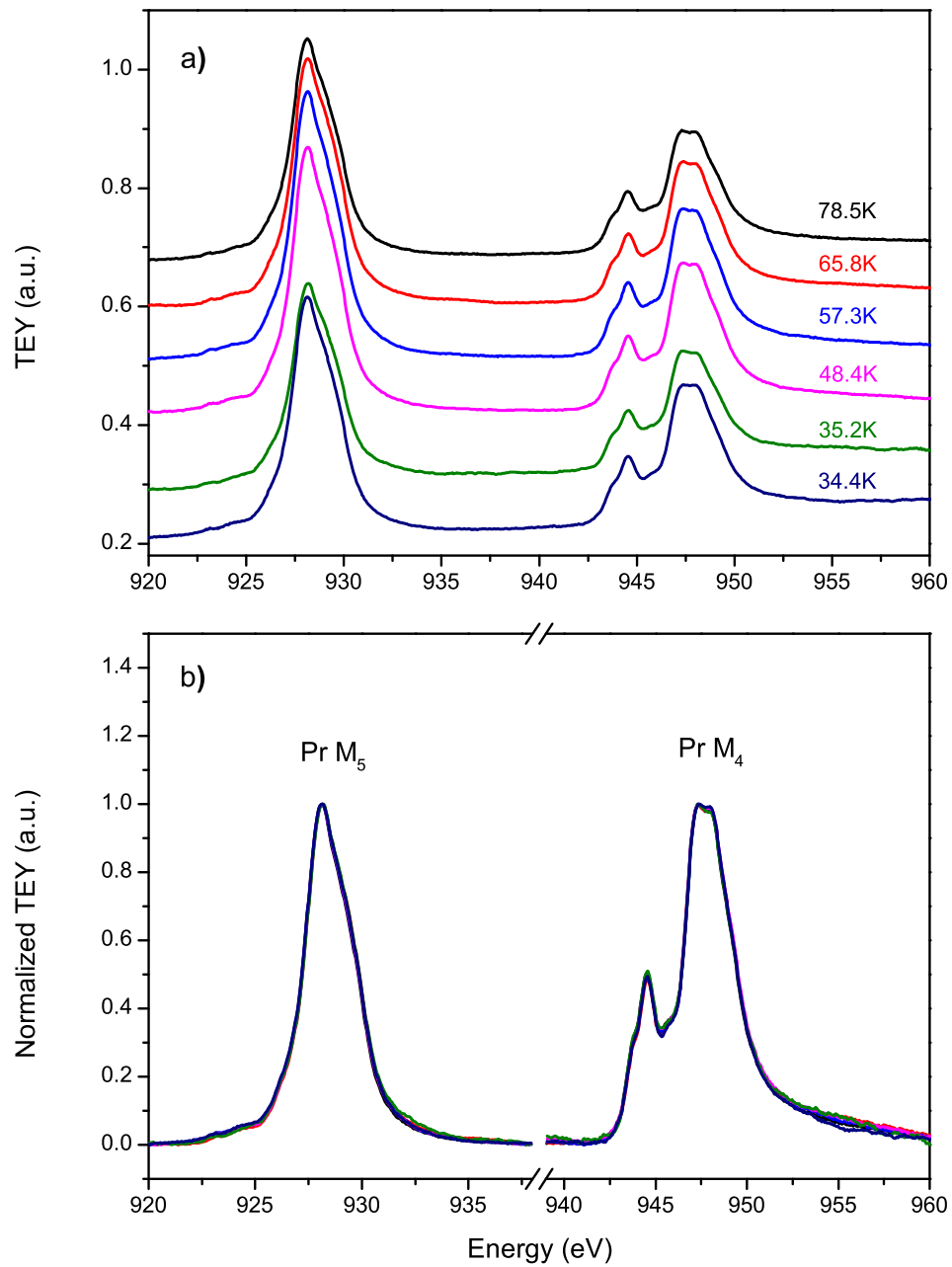


Figure 5.6: The Pr  $M_{4,5}$  edge absorption spectra of  $\text{PrRu}_4\text{P}_{12}$  measured at different temperatures and plotted with a) the spectrum vertically shifted to each other by an almost fixed value and b) Pr  $M_5$  edge and  $M_4$  edge separately normalized to 1 after subtracting a linear background from the respective spectrum in a).

Pr (000) and  $(\frac{1}{2}\frac{1}{2}\frac{1}{2})$  displace slightly away from their high-temperature cell coordinate a distance of  $d$  and  $-d$  respectively along  $a$ -axis where the negative sign means two atoms displace in opposite directions. The intensity

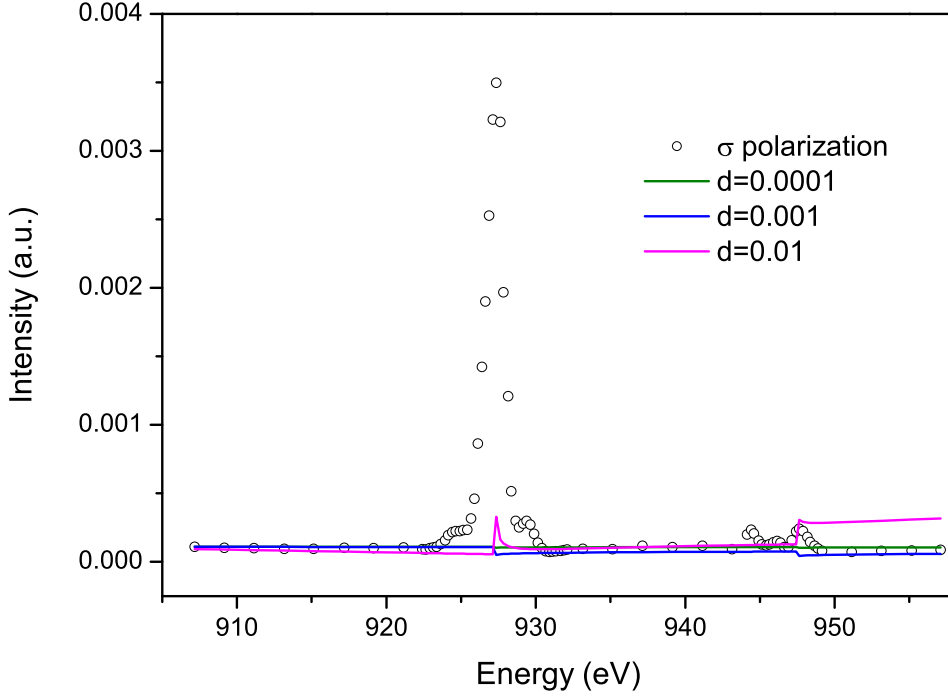


Figure 5.7: The integrated intensity of (100) diffraction as a function of energy for  $\sigma$  polarization plotted together with the calculated curves assuming different displacement of Pr.

of (100) superlattice reflection is then given by

$$|F(E)|^2 = |f_{Ru}[\cos(2\pi x_{Ru}) - i \sin(2\pi x_{Ru})] - 2f_{Pr}i \sin(2\pi d)|^2, \quad (5.4)$$

where  $f_{Ru}$  and  $f_{Pr}$  are the atomic form factors of Ru and Pr respectively and  $x_{Ru}$  is the position of Ru in the  $\text{Pm}\bar{3}$  unit cell. The coupled equations for near-edge energies and off-edge energies however gave complex solutions for  $d$  which are of no physical meaning. Adding any small displacement value within the range of 0.00001 to 0.05 of the unit cell into the expression for the reflection intensity also failed to reproduce the experimental intensities (see Fig 5.7). This is consistent with the previous crystal structure and Pr- $L_3$ -edge extended x-ray absorption fine structure (EXAFS) studies in which the displacement of Pr below  $T_{MI}$  was not observed but the MI transition was proposed to be related to a detectable Ru displacement [69, 70, 91].

The valence of Pr has typical feature of 3+ and appears to remain unchanged across  $T_{MI}$ , suggesting that at low temperature presence of an average valence  $v$  ( $3 < v < 4$ ) is not possible. Therefore the charge order of 3+ and 4+ for the two Pr sites is not likely the case. However possibility

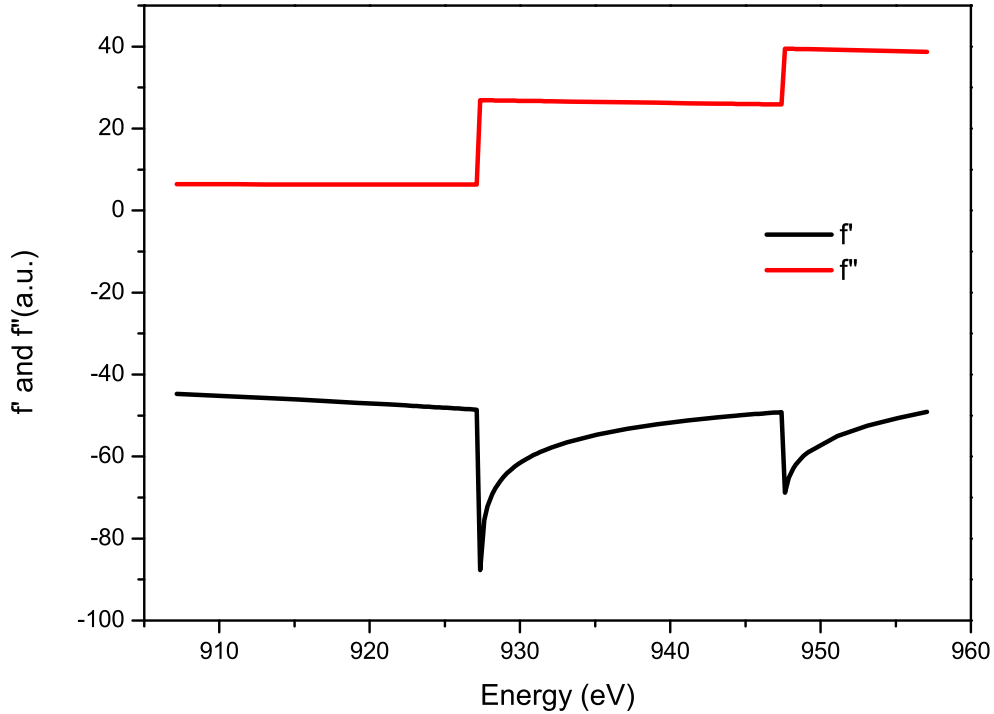


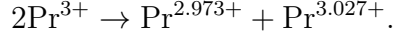
Figure 5.8: The theoretical Cromer-Lieberman anomalous scattering factors of Pr.

of small charge disproportionation is still allowed. Assuming two Pr atoms have charge of  $3 + \varepsilon$  and  $3 - \varepsilon$  respectively, the average charge of Pr is still  $3+$ ; Moreover this is physically possible since there might exist charge transfers between the Pr atom and the surrounding Ru ions. Concretely, the Pr atom within an environment of compressed and expanded cube of Ru (see Fig 5.1) might obtain and lose charge respectively. Correspondingly, they have charge of  $3 + \varepsilon$  and  $3 - \varepsilon$  respectively. Indeed, two configurations were observed in a previous Pr  $L_2$  edge XANES study on  $\text{PrRu}_4\text{P}_{12}$  [75] which might correspond to two charge states, although they were not assigned as two charges by the authors. The structure factor can then be written as

$$|F(E)|^2 = |f_{\text{Ru}}e^{-i2\pi(hx+ky+lz)} + [f_{\text{Pr1}} - f_{\text{Pr2}}]|^2, \quad (5.5)$$

where  $f_{\text{Pr1}}$  and  $f_{\text{Pr2}}$  represent the structure factors for Pr1 and Pr2 due to two different charges. To simplify the problem, we assume that the two different charges correspond respectively to an energy shift of  $+\delta$  and  $-\delta$  for the scattering factor of  $\text{Pr}^{3+}$ , similar to that adopted in [92]. It was found that the model reproduces well the intensities at off-edge energies

and the  $M_5$  edge when using  $\delta = 0.04$  eV and the theoretical Cromer-Lieberman anomalous scattering factors of Pr as shown in Fig 5.8.  $\text{Pr}^{4+}$  is  $\sim 1.5$  eV higher in energy than  $\text{Pr}^{3+}$  [93]. Assuming the charge variation is proportional to the chemical shift, then a 0.04 eV chemical shift corresponds to a change of charge  $\sim 0.027$  electrons, i.e., below  $T_{MI}$  the following charge disproportionation occurs,



This chemical shift has the same order of magnitude as the resolution of the XANES, therefore the small charge disproportionation is not resolved in absorption spectra however it can be observed via RSXD which is sensitive to electronic orders. The theoretical Cromer-Lieberman anomalous scattering factors of Pr fail to account for the rich structures in energy profile which arise from the solid state effect, since they are computed based on bare free atoms, however indeed they are able to account for the intensities of the main structure. The straightforward use of Cromer-Lieberman results here is justified by the fact that near the  $M_5$  edge the white line (i.e., the “step” of the edge) which corresponds to the transition to the continuum is negligibly small. As pointed out by Cross *et al.* [94], Cromer-Lieberman calculations are invalid in cases where the white line is large; deduction of anomalous scattering factors from absorption spectra is then necessary. The discrepancy between the calculated and measured intensities at  $M_4$  edge is then a sign of improper use of the Cromer-Lieberman results, since compared with its  $M_5$  edge counterpart, it has an obviously larger white line and Cromer-Lieberman results are therefore likely to be invalid. It has to be pointed out that efforts have been made to theoretically calculate the RSXD intensities based on the anomalous scattering factors that were extracted from the absorption spectra recorded at the lowest temperature by using the DIFFKK program [94], however the charge disproportionation was found to be as large as 1 electron. This seems impossible, as no sign of such a large charge disproportionation are observed in the absorption spectra, unless the mobile electrons jump between ionic states with times faster than the interaction time for the photoabsorption process. This large charge disproportionation found implies that probably the anomalous scattering factors obtained from the DIFFKK calculation are not good enough or DIFFKK program is not suitable for calculations at low energy scales.

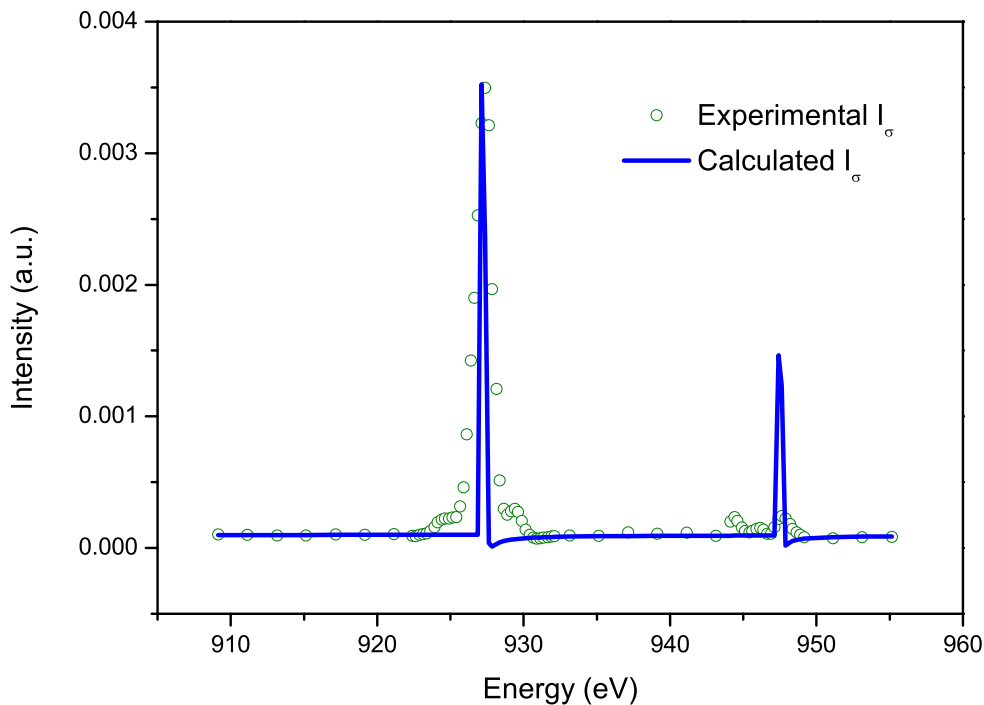


Figure 5.9: The integrated intensity of (100) diffraction as a function of energy for  $\sigma$  polarization plotted together with the calculated curve based on charge disproportionation of  $\text{Pr}^{3+}$ .

As far as we know, there are no publications reporting use of DIFFKK program below 1000 eV.

## 5.5 Conclusion

In conclusion, soft resonant x-ray diffraction in combination with x-ray absorption spectroscopy were performed at the Pr  $M_{4,5}$  edges to investigate the order parameter of Pr below  $T_{MI} = 62.3$  K in  $\text{PrRu}_4\text{P}_{12}$ . The intensities of the (100) superlattice peak were measured as a function of energy, temperature, polarization and azimuthal angle. A resonance enhancement of the (100) superlattice reflection at the Pr  $M_{4,5}$  edges was observed below  $T_{MI}$  which underwent a steady increase with decreasing temperature. The possibility of magnetic and/or orbital order at Pr sites was ruled out by the azimuthal angular profile and x-ray absorption spectra respectively. Displacement of Pr was also ruled out in the subsequent effort to model the energy dependence of intensity of (100). The order parameter of the Pr 4f

shells is likely due to charge disproportionation and must couple closely to Ru and play integral roles in the MI transition synergistically in  $\text{PrRu}_4\text{P}_{12}$ .

# Chapter 6

## Summary and outlook

In this thesis, electric and magnetic properties of exotic strongly correlated electron systems are explored via studies of  $\text{La}_2\text{Ti}_{2-x}\text{V}_x\text{O}_7$ ,  $\text{CaMn}_7\text{O}_{12}$  and  $\text{PrRu}_4\text{P}_{12}$ .

In order to introduce a ferromagnetic order into the ferroelectric  $\text{La}_2\text{Ti}_2\text{O}_7$  to form a proper multiferroic and test the validity of a reported theoretical calculation,  $\text{La}_2\text{Ti}_{2-x}\text{V}_x\text{O}_7$  ( $x = 0, 0.0625, 0.125$  and  $0.25$ ) was synthesized by a conventional solid state reaction and a vacuum annealing plus water quenching method respectively. XRD pattern show that only the doped sample with  $x$  up to 0.125 synthesized by a vacuum annealing plus water quenching method is of a single phase same to the undoped  $\text{La}_2\text{Ti}_2\text{O}_7$ , indicating that vanadium is successfully doped into  $\text{La}_2\text{Ti}_2\text{O}_7$  by the latter method. The magnetic properties of the single phase doped samples were studied by a SQUID magnetometer and compared with that of undoped  $\text{La}_2\text{Ti}_2\text{O}_7$ . The results reveal however a primary paramagnetic-like behaviour and a weak magnetic order rather than the ferromagnetic order for the doped samples, which is explained by a vanadium monomer phase formed at the high synthesis temperature. In this sense we have demonstrated that the prediction of the phase diagram of vanadium phase in  $\text{La}_2\text{Ti}_{2-x}\text{V}_x\text{O}_7$  [41] is valid at high temperatures. To obtain a single phase with ferromagnetic order, other novel synthesis method with a lower synthesis temperature has to be used. We note that single phase  $\text{La}_2\text{Ti}_2\text{O}_7$  was successfully synthesized at  $T \sim 700$  °C by a polymerized complex method [95]. Since soluble chemicals were used as starting materials in this

method and better mixing of the elements was achieved then the synthesis temperature was lowered. We propose that this method may be used in combination with a water quenching method employed in this thesis. The polymerized complex method can be adopted to produce the precursor which may then be treated by the water quenching method. It is also noted that the methods that were proposed in [41], i.e., molecular beam epitaxy and pulsed laser deposition may also be useful.

FE polarization is driven by magnetism in improper multiferroic. In our study, we extend the isotopic substitution technique to a multiferroic with the aim of revealing the coupling mechanism between ferroelectricity and magnetism by studying the isotope substitution effect on magnetic properties. The multiferroic  $\text{CaMn}_7\text{O}_{12}$  was synthesized successfully by a flux method. The  $^{18}\text{O}$  isotope exchange was performed on the sample. The  $^{18}\text{O}$  concentration was found to be  $\sim 61$  at.% by Raman Spectroscopy and  $\sim 64$  at.% from the mass difference before and after oxygen isotope substitution. The crystal structure of the sample remains the same after  $^{18}\text{O}$  substitution however smaller magnetization was observed for  $50 < T < 120$  K wherein two characteristic magnetic transitions of  $\text{CaMn}_7\text{O}_{12}$  occur and FE polarization develops. This can be considered as a direct evidence that oxygen is related to the magnetic properties as well as the FE polarization of this material. However different divergence temperatures were also observed. It is not clear whether the change of magnetization has a contribution from the different divergence temperatures. To clarify this point, two experiments can be alternatively considered. Firstly a  $^{16}\text{O}$  recovery experiment may be done to exchange the  $^{18}\text{O}$  in the sample with  $^{16}\text{O}$ . Secondly the  $\text{CaMn}_7^{16}\text{O}_{12}$  could be heat treated in the same way as for  $^{18}\text{O}$  substitution experiment but under the atmosphere of  $^{16}\text{O}_2$ . If either resultant sample reproduces the magnetic behaviour observed for  $\text{CaMn}_7^{16}\text{O}_{12}$ , i.e., showing a divergence temperature of 120 K, then the change of magnetization is not likely to be induced by the different divergence temperatures but is probably associated with oxygen.

To investigate the order parameter of Pr below  $T_{MI} = 62.3$  K in  $\text{PrRu}_4\text{P}_{12}$  temperature dependent resonant soft x-ray diffraction in combination with x-ray absorption spectroscopy were performed at the Pr  $M_{4,5}$  edges. A resonance enhancement of the (100) superlattice reflection signalling the

order parameter of the Pr 4f shells was observed below  $T_{MI}$ , with a steady increase with decreasing temperature. The experimental spectra and subsequent analysis rule out the existence of magnetic and/or orbital order as well as any Pr lattice displacement. A model based on a small charge disproportionation  $\pm 0.027$  electrons from  $\text{Pr}^{3+}$  reproduces well the RSXD intensities at off-edge energies and the  $M_5$  edge. The order parameter below  $T_{MI}$  is therefore likely due to charge disproportionation. Our results also indicate that a synergistic coupling of Pr 4f - Ru states plays an important role in the metal-insulator transition associated with charge density wave state formation. Extraction of the anomalous scattering factors from the absorption spectra is required in order to account for all the structures observed in the energy profile and further confirm the charge disproportionation model.

The common theme in the study of  $\text{La}_2\text{Ti}_{2-x}\text{V}_x\text{O}_7$  and  $\text{PrRu}_4\text{P}_{12}$  in this thesis is the desire to understand phase transitions in strongly correlated electron systems. The MI transition in the latter system is a classical phase transition driven by thermal fluctuations through temperature variation, while in the former system the emergence of antiferromagnetic or weak ferromagnetic order is believed to be a result of a quantum phase transition, driven by quantum fluctuations which are tuned by chemical impurities of the system. The investigation of these phase transitions in turn enables an understanding of the novel properties of these anomalous strongly correlated electron systems. Both of these two systems clearly warrant further study. The investigation of the isotope substitution effect on magnetism of  $\text{CaMn}_7\text{O}_{12}$  in this thesis contributes to the effort to understand the origin of ferroelectric phenomenon in magnetic strongly correlated electron systems. Isotope substitution is a powerful technique to reveal the subtle physics behind strongly correlated electron systems, which has been demonstrated in magnetoresistive systems and high temperature superconductors. Our study is preliminary and although no decisive conclusion can be made, it is believed that further experiments including additional characterisation techniques, such as inelastic neutron scattering, would shed light on the origin of ferroelectric phenomenon in magnetic strongly correlated electron systems.

# Appendix A

## Reliability factors of Rietveld refinement

Table A.1

Factor name	Computation formula
Profile reliability factor	$R_p = \frac{\sum_i  y_{i,obs} - y_{i,cal} }{\sum_i y_{i,obs}} \times 100$
Weighted profile reliability factor	$R_{wp} = \left[ \frac{\sum_i w_i (y_{i,obs} - y_{i,cal})^2}{\sum_i w_i y_{i,obs}^2} \right]^{1/2} \times 100$
Expected profile reliability factor	$R_{exp} = \left[ \frac{N - P + C}{\sum_i w_i y_{i,obs}^2} \right]^{1/2} \times 100$
Bragg R-factor	$R_{Bragg} = \frac{\sum_{hkl}  I_{hkl,obs} - I_{hkl,cal} }{\sum  I_{hkl,obs} } \times 100$
RF-factor	$R_F = \frac{\sum_{hkl}  F_{hkl,obs} - F_{hkl,cal} }{\sum_{hkl}  F_{hkl,obs} } \times 100$
Goodness of fit	$\chi^2 = \left( \frac{R_{wp}}{R_{exp}} \right)^2$

# Bibliography

- [1] H. Schmid, “Multi-ferroic Magnetoelectrics,” *Ferroelectrics*, **vol. 162**, p. 317, 1994.
- [2] N. A. Spaldin and M. Fiebig, “The Renaissance of Magnetoelectric Multiferroics,” *Science*, **vol. 309**, **no. 5733**, p. 391, 2005.
- [3] P. Curie, “Sur la symétrie dans les phénomènes physiques, symétrie d’un champ électrique et d’un champ magnétique,” *Journal de Physique Théorique et Appliquée*, **vol. 3**, **no. 1**, p. 393, 1894.
- [4] G. Rado and V. Folen, “Observation of the Magnetically Induced Magnetoelectric Effect and Evidence for Antiferromagnetic Domains,” *Physical Review Letters*, **vol. 7**, p. 310, 1961.
- [5] K. F. Wang, J. M. Liu and Z. F. Ren, “Multiferroicity: The Coupling between Magnetic and Polarization Orders,” *Advances in Physics*, **vol. 58**, **no. 4**, p. 321, 2009.
- [6] D. Khomskii, “Classifying Multiferroics: Mechanisms and Effects,” *Physics*, **vol. 2**, p. 20, 2009.
- [7] B. V. Aken, T. Palstra, A. Filippetti and N. Spaldin, “The Origin of Ferroelectricity in Magnetoelectric YMnO<sub>3</sub>,” *Nature Materials*, **vol. 3**, p. 164, 2004.
- [8] H. Katsura, N. Nagaosa and A. V. Balatsky, “Spin Current and Magnetoelectric Effect in Noncollinear Magnets,” *Physical Review Letters*, **vol. 95**, p. 057205, 2005.
- [9] I. A. Sergienko and E. Dagotto, “Role of the Dzyaloshinskii-Moriya Interaction in Multiferroic Perovskites,” *Physical Review B*, **vol. 73**, p. 094434, 2006.

- [10] A. S. Moskvin and R. V. Pisarev, “Charge-transfer Transitions in Mixed-valent Multiferroic  $\text{TbMn}_2\text{O}_5$ ,” *Physical Review B*, **vol. 77**, p. 060102, 2008.
- [11] G. Giovannetti and J. van den Brink, “Electronic Correlations Decimate the Ferroelectric Polarization of Multiferroic  $\text{HoMn}_2\text{O}_5$ ,” *Physical Review Letters*, **vol. 100**, **no. 22**, 2008.
- [12] S. Partzsch, S. B. Wilkins, J. P. Hill, E. Schierle, E. Weschke, D. Souptel, B. Buchner and J. Geck, “Observation of Electronic Ferroelectric Polarization in Multiferroic  $\text{YMn}_2\text{O}_5$ ,” *Physical Review Letters*, **vol. 107**, **no. 5**, 2011.
- [13] S. W. Cheong and M. Mostovoy, “Multiferroics: A Magnetic Twist for Ferroelectricity,” *Nature Materials*, **vol. 6**, **no. 1**, p. 13, 2007.
- [14] T. Kimura, T. Goto, H. Shintani, K. Ishizaka, T. Arima and Y. Tokura, “Magnetic Control of Ferroelectric Polarization,” *Nature*, **vol. 426**, **no. 6962**, p. 55, 2003.
- [15] N. Hur, S. Park, P. A. Sharma, J. S. Ahn, S. Guha and S. W. Cheong, “Electric Polarization Reversal and Memory in a Multiferroic Material Induced by Magnetic Fields,” *Nature*, **vol. 429**, **no. 6990**, p. 392, 2004.
- [16] I. Dzyaloshinskii, “Thermodynamic Theory of Weak Ferromagnetism in Antiferromagnetic Substances,” *Soviet physics, Journal of Experimental and Theoretical Physics*, **vol. 5**, p. 1259, 1957.
- [17] F. Gebhard, *The Mott Metal-Insulator Transition, Springer Tracts in Modern Physics*, vol. 137, Springer Berlin Heidelberg, 1997.
- [18] K. E. Smith, “Chapter 9. Metal to Non-metal Transitions in Solids and on Surfaces Studied using Photoemission Spectroscopy,” *Annu. Rep. Prog. Chem., Sect. C: Phys. Chem.*, **vol. 92**, p. 253, 1995.
- [19] K.-S. Chao, *Charge, Orbital, and Spin Order of Transition-Metal Oxides*, Ph.D. thesis, 2007.

- [20] D. Balla and N. B. Brandt, “Investigation of the Effect of Uniform Compression on the Temperature Dependence of the Electrical Conductivity of Bismuth,” *Soviet physics, Journal of Experimental and Theoretical Physics*, **vol. 20**, p. 1111, 1965.
- [21] S. van Smaalen, “The Peierls Transition in Low-dimensional Electronic Crystals,” *Acta Crystallographica Section A*, **vol. 61**, p. 51, 2005.
- [22] E. Verwey, “Electronic Conduction of Magnetite ( $\text{Fe}_3\text{O}_4$ ) and Its Transition Point at Low Temperatures,” *Nature*, **vol. 144**, p. 327, 1939.
- [23] M. S. Senn, J. P. Wright and J. P. Attfield, “Charge Order and Three-Site Distortions in the Verwey Structure of Magnetite,” *Nature*, **vol. 481**, **no. 7380**, p. 173, 2012.
- [24] N. F. Mott and Z. Zinamon, “The Metal-nonmetal Transition,” *Reports on Progress in Physics*, **vol. 33**, p. 881, 1970.
- [25] L. Paolasini, C. Vettier, F. de Bergevin, F. Yakhou, D. Mannix, A. Stunault, W. Neubeck, M. Altarelli, M. Fabrizio, P. A. Metcalf and J. M. Honig, “Orbital Occupancy Order in  $\text{V}_2\text{O}_3$ : Resonant X-Ray Scattering Results,” *Physical Review Letters*, **vol. 82**, p. 4719, 1999.
- [26] B. B. Van Aken, O. D. Jurchescu, A. Meetsma, Y. Tomioka, Y. Tokura and T. T. M. Palstra, “Orbital-Order-Induced Metal-Insulator Transition in  $\text{La}_{1-x}\text{Ca}_x\text{MnO}_3$ ,” *Physical Review Letters*, **vol. 90**, p. 066403, 2003.
- [27] Y. Endoh, K. Hirota, S. Ishihara, S. Okamoto, Y. Murakami, A. Nishizawa, T. Fukuda, H. Kimura, H. Nojiri, K. Kaneko and S. Maekawa, “Transition between Two Ferromagnetic States Driven by Orbital Ordering in  $\text{La}_{0.88}\text{Sr}_{0.12}\text{MnO}_3$ ,” *Physical Review Letters*, **vol. 82**, p. 4328, 1999.
- [28] H. Myers, *Introductory solid state physics*, Taylor & Francis, 1990.
- [29] W. Bragg, “The diffraction of short electromagnetic waves by a crystal,” “Proceedings of the Cambridge Philosophical Society,” , vol. 17p. 43, 1913.
- [30] C. Kittel, *Introduction to Solid State Physics*, Wiley, 2005.

- [31] F. Groot and J. Vogel, “Fundamentals of X-ray Absorption and Dichroism: The Multiplet Approach,” “Neutron and X-ray Spectroscopy,” (eds.) F. Hippert, E. Geissler, J. Hodeau, E. Lelièvre-Berna and J.-R. Regnard, pp. 3–66, Springer Netherlands, 2006.
- [32] J. M. Tranquada, S. M. Heald, A. Moodenbaugh and M. Suenaga, “X-ray absorption studies of  $\text{La}_{2-x}(\text{Ba},\text{Sr})_x\text{CuO}_4$  superconductors,” *Physical Review B*, **vol. 35**, p. 7187, 1987.
- [33] S. W. Lovesey, E. Balcar, K. S. Knight and J. Fernandez-Rodriguez, “Electronic Properties of Crystalline Materials Observed in X-ray Diffraction,” *Physics Reports*, **vol. 411**, p. 233, 2005.
- [34] J. Fink, E. Schierle, E. Weschke and J. Geck, “Resonant elastic soft x-ray scattering,” *Reports on Progress in Physics*, **vol. 76**, **no. 5**, p. 056502, 2013.
- [35] J. P. Hill and D. F. McMorrow, “Resonant Exchange Scattering: Polarization Dependence and Correlation Function,” *Acta Crystallographica Section A*, **vol. 52**, **no. 2**, p. 236, 1996.
- [36] J. Coey, *Magnetism and Magnetic Materials*, Magnetism and Magnetic Materials, 2010.
- [37] Nanamats.S, M. Kimura, K. Doi, Matsushi.S and N. Yamada, “New Ferroelectric -  $\text{La}_2\text{Ti}_2\text{O}_7$ ,” *Ferroelectrics*, **vol. 8**, **no. 1-2**, p. 511, 1974.
- [38] J. Lopez-Perez and J. Iniguez, “Ab Initio Study of Proper Topological Ferroelectricity in Layered Perovskite  $\text{La}_2\text{Ti}_2\text{O}_7$ ,” *Physical Review B*, **vol. 84**, **no. 7**, p. 075121, 2011.
- [39] K. Momma and F. Izumi, “Vesta 3 for Three-Dimensional Visualization of Crystal, Volumetric and Morphology Data,” *Journal of Applied Crystallography*, **vol. 44**, p. 1272, 2011.
- [40] M. Scarrozza, A. Filippetti and V. Fiorentini, “Ferromagnetism and Orbital Order in a Topological Ferroelectric,” *Physical Review Letters*, **vol. 109**, **no. 21**, p. 217202, 2012.
- [41] M. Scarrozza, A. Filippetti and V. Fiorentini, “Multiferroicity in Vanadium-Doped  $\text{La}_2\text{Ti}_2\text{O}_7$ : Insights from First Principles,” *European Physical Journal B*, **vol. 86**, **no. 4**, p. 128, 2013.

- [42] H. Yokokawa, N. Sakai, T. Kawada and M. Dokiya, “Thermodynamic Stabilities of Perovskite Oxides for Electrodes and Other Electrochemical Materials,” *Solid State Ionics*, **vol. 52, no. 1-3**, p. 43, 1992.
- [43] Gmelin-Institute, *Sc, Y, La und Lanthanide-Verbindungen, Gmelin Handbuch der Anorganischen Chemie*, Springer Berlin Heidelberg, 1974.
- [44] R. Bertram and D. Klimm, “Assay Measurements of Oxide Materials by Thermogravimetry and ICP-OES,” *Thermochimica Acta*, **vol. 419, no. 1-2**, p. 189, 2004.
- [45] Z. Hiroi, H. Hayamizu, T. Yoshida, Y. Muraoka, Y. Okamoto, J. Yamamura and Y. Ueda, “Spinodal Decomposition in the TiO<sub>2</sub>-VO<sub>2</sub> System,” *Chemistry of Materials*, **vol. 25, no. 11**, p. 2202, 2013.
- [46] “Recent advances in magnetic structure determination by neutron powder diffraction,” *Physica B: Condensed Matter*, **vol. 192, no. 1-2**, p. 55, 1993.
- [47] M. Gasperin, “Dititanate de lanthane,” *Acta Crystallographica Section B*, **vol. 31, no. 8**, p. 2129, 1975.
- [48] R. D. Shannon, “Revised effective ionic radii and systematic studies of interatomic distances in halides and chalcogenides,” *Acta Crystallographica Section A*, **vol. 32, no. 5**, p. 751, 1976.
- [49] L. Sun, J. F. Hu, F. Gao, X. W. Kong, H. W. Qin and M. H. Jiang, “Room-Temperature Ferromagnetism and Ferroelectricity of Nanocrystalline La<sub>2</sub>Ti<sub>2</sub>O<sub>7</sub>,” *Journal of Alloys and Compounds*, **vol. 502, no. 1**, p. 176, 2010.
- [50] B. Bochu, J. Chenavas, J. Joubert and M. Marezio, “High Pressure Synthesis and Crystal Structure of A New Series of Perovskite-like Compounds CMn<sub>7</sub>O<sub>12</sub> (C = Na, Ca, Cd, Sr, La, Nd),” *Journal of Solid State Chemistry*, **vol. 11, no. 2**, p. 88, 1974.
- [51] R. D. Johnson, L. C. Chapon, D. D. Khalyavin, P. Manuel, P. G. Radaelli and C. Martin, “Giant Improper Ferroelectricity in the Ferroaxial Magnet CaMn<sub>7</sub>O<sub>12</sub>,” *Physical Review Letters*, **vol. 108**, p. 067201, 2012.

- [52] A. N. Vasil'ev and O. S. Volkova, "New Functional Materials  $\text{AC}_3\text{B}_4\text{O}_{12}$  (Review)," *Low Temperature Physics*, **vol. 33**, **no. 11**, p. 895, 2007.
- [53] R. Przeniosło, I. Sosnowska, E. Suard, A. Hewat and A. Fitch, "Charge Ordering and Anisotropic Thermal Expansion of the Manganese Perovskite  $\text{CaMn}_7\text{O}_{12}$ ," *Physica B: Condensed Matter*, **vol. 344**, **no. 1–4**, p. 358, 2004.
- [54] R. Przeniosło, I. Sosnowska, D. Hohlwein, T. Hauß and I. Troyanchuk, "Magnetic Ordering in the Manganese Perovskite  $\text{CaMn}_7\text{O}_{12}$ ," *Solid State Communications*, **vol. 111**, **no. 12**, p. 687, 1999.
- [55] M. Sánchez-Andújar, S. Yáñez-Vilar, N. Biskup, S. Castro-García, J. Mira, J. Rivas and M. Señarís-Rodríguez, "Magnetoelectric Behavior in the Complex  $\text{CaMn}_7\text{O}_{12}$  perovskite," *Journal of Magnetism and Magnetic Materials*, **vol. 321**, **no. 11**, p. 1739, selected papers from the Symposium F "Multiferroics and Magnetoelectrics Materials" of the E-MRS Conference, 2009.
- [56] G. Zhang, S. Dong, Z. Yan, Y. Guo, Q. Zhang, S. Yunoki, E. Dagotto and J.-M. Liu, "Multiferroic Properties of  $\text{CaMn}_7\text{O}_{12}$ ," *Physical Review B*, **vol. 84**, p. 174413, 2011.
- [57] X. Z. Lu, M.-H. Whangbo, S. Dong, X. G. Gong and H. J. Xiang, "Giant Ferroelectric Polarization of  $\text{CaMn}_7\text{O}_{12}$  Induced by a Combined Effect of Dzyaloshinskii-Moriya Interaction and Exchange Striction," *Physical Review Letters*, **vol. 108**, p. 187204, 2012.
- [58] G.-m. Zhao, K. Conder, H. Keller and K. A. Muller, "Giant Oxygen Isotope Shift in the Magnetoresistive Perovskite  $\text{La}_{1-x}\text{Ca}_x\text{MnO}_{3+y}$ ," *Nature*, **vol. 381**, **no. 6584**, p. 676, 1996.
- [59] G.-m. Zhao, K. Conder, M. Angst, S. M. Kazakov, J. Karpinski, M. Maciejewski, C. Bougerol, J. S. Pshirkov and E. V. Antipov, "Large oxygen-isotope effect in  $\text{Sr}_{0.4}\text{K}_{0.6}\text{BiO}_3$ : Evidence for phonon-mediated superconductivity," *Physical Review B*, **vol. 62**, p. R11977, 2000.
- [60] W. Sławiński, R. Przeniosło, I. Sosnowska and V. Petříček, "Helical Screw Type Magnetic Structure of the Multiferroic  $\text{CaMn}_7\text{O}_{12}$  with

- low Cu-doping,” *Acta Crystallographica Section B*, **vol. 68**, **no. 3**, p. 240, 2012.
- [61] O. Frank, M. Zupalova, B. Laskova, J. Kurti, J. Koltai and L. Kavan, “Raman spectra of titanium dioxide (anatase, rutile) with identified oxygen isotopes (16, 17, 18),” *Phys. Chem. Chem. Phys.*, **vol. 14**, p. 14567, 2012.
- [62] A. Mulders, private communication, 2013.
- [63] C. Sekine, K. Akahira, K. Ito and T. Yagi, “Magnetic Properties of New Filled Skutterudite Compounds  $\text{EuT}_4\text{As}_{12}$  (T = Fe, Ru, and Os) Synthesized under High Pressure,” *Journal of the Physical Society of Japan*, **vol. 78**, **no. 9**, p. 093707, 2009.
- [64] G. P. Meisner, “Superconductivity and Magnetic Order in Ternary Rare Earth Transition Metal Phosphides,” *Physica B*, **vol. 108**, p. 763, 1981.
- [65] U. Eckern, A. Schmid, W. Weber and H. Wühl, (eds.), *Magnetic Susceptibility, Electrical Resistivity, and Specific Heat of Single Crystal  $\text{LaFe}_4\text{P}_{12}$* , Proceedings of the 17th International Conference on Low Temperature Physics, North-Holland/American Elsevier, Amsterdam, 1984.
- [66] M. S. Torikachvili, J. W. Chen, Y. Dalichaouch, R. P. Guertin, M. W. McElfresh, C. Rossel, M. B. Maple and G. P. Meisner, “Low-temperature Properties of Rare-earth and Actinide Iron Phosphide Compounds  $\text{MFe}_4\text{P}_{12}$  (M = La, Pr, Nd, and Th),” *Physical Review B*, **vol. 36**, p. 8660, 1987.
- [67] H. Sato, Y. Abe, H. Okada, T. D. Matsuda, K. Abe, H. Sugawara and Y. Aoki, “Anomalous Transport Properties of  $\text{RFe}_4\text{P}_{12}$  (R= La, Ce, Pr, and Nd),” *Physical Review B*, **vol. 62**, p. 15125, 2000.
- [68] C. Sekine, T. Uchiumi, I. Shirotnani and T. Yagi, “Metal-Insulator Transition in  $\text{PrRu}_4\text{P}_{12}$  with Skutterudite Structure,” *Physical Review Letters*, **vol. 79**, p. 3218, 1997.
- [69] C. H. Lee, H. Matsuhata1, A. Yamamoto, T. Ohta, H. Takazawa, K. Ueno, C. Sekine, I. Shirotnani and T. Hirayama, “Structural Phase

- Transition Accompanied by Metal-insulator Transition in  $\text{PrRu}_4\text{P}_{12}$ ,” *Journal of Physics: Condensed Matter*, **vol. 13**, p. L45, 2001.
- [70] C. H. Lee, H. Matsuhata, H. Yamaguchi, C. Sekine, K. Kihou and I. Shirotni, “A Study of the Crystal Structure at Low Temperature in the Metal–insulator Transition Compound  $\text{PrRu}_4\text{P}_{12}$ ,” *Journal of Magnetism and Magnetic Materials*, **vol. 272-276**, p. 426, 2004.
- [71] S. R. Saha, H. Sugawara, Y. Aoki, H. Sato, Y. Inada, H. Shishido, R. Settai, Y. Onuki and H. Harima, “Fermi Surface of  $\text{LaRu}_4\text{P}_{12}$ : A Clue to the Origin of the Metal-insulator Transition in  $\text{PrRu}_4\text{P}_{12}$ ,” *Physical Review B*, **vol. 71**, p. 132502, 2005.
- [72] C. H. Lee, H. Matsuhata, H. Yamaguchi, C. Sekine, K. Kihou, T. Suzuki, T. Noro and I. Shirotni, “Charge-density-wave Ordering in the Metal-insulator Transition Compound  $\text{PrRu}_4\text{P}_{12}$ ,” *Physical Review B*, **vol. 70**, p. 153105, 2004.
- [73] C. Sekine, T. Inaba, I. Shirotni, M. Yokoyama, H. Amitsuka and T. Sakakibara, “The Specific Heat of the Filled Skutterudite  $\text{PrRu}_4\text{P}_{12}$  in Magnetic Fields,” *Physica B*, **vol. 281-282**, p. 303, 2000.
- [74] W. D. Hutchison, “Applications of Low Temperature Nuclear Orientation,” *Hyperfine Interact*, **vol. 220**, p. 11, 2013.
- [75] C. H. Lee, H. Oyanagi, C. Sekine, I. Shirotni and M. Ishii, “XANES Study of Rare-Earth Valency in  $\text{LRu}_4\text{P}_{12}$  ( $L = \text{Ce}$  and  $\text{Pr}$ ),” *Physical Review B*, **vol. 60**, p. 13253, 1999.
- [76] S. Curnoe, H. Harima, K. Takegaharac and K. Ueda, “Structural Phase Transition and Anti-quadrupolar Ordering in  $\text{PrFe}_4\text{P}_{12}$  and  $\text{PrRu}_4\text{P}_{12}$ ,” *Physica B*, **vol. 312-313**, p. 837, 2002.
- [77] Y. Kuramoto, H. Kusunose and A. Kiss, “Diffraction from Ordered States of Higher Multipoles,” *Physica B*, **vol. 383**, p. 5, 2006.
- [78] K. Ishii, S. Tsutsui, L. Hao, T. Hasegawa, K. Iwasa, M. Tsubota, T. Inami, Y. Murakami, S. R. Saha, H. Sugawara and H. Sato, “Resonant X-Ray Scattering of  $\text{PrRu}_4\text{P}_{12}$ ,” *Journal of Magnetism and Magnetic Materials*, **vol. 310, no. 2**, p. E178, 2007.

- [79] S. Kong, W. Y. Zhang and D. N. Shi, “Orbital-Ordering-Induced Metal-Insulator Transition in PrRu<sub>4</sub>P<sub>12</sub>,” *New Journal of Physics*, **vol. 10**, p. 093020, .
- [80] A. M. Mulders, U. Staub, V. Scagnoli, S. W. Lovesey, E. Balcar, T. Nakamura, A. Kikkawa, G. van der Laan and J. M. Tonnerre, “High-order Dy Multipole Motifs Observed in DyB<sub>2</sub>C<sub>2</sub> with Resonant Soft X-ray Bragg Diffraction,” *Journal of Physics: Condensed Matter*, **vol. 18**, p. 11195, 2006.
- [81] A. J. Princep, A. M. Mulders, U. Staub, V. Scagnoli, T. Nakamura, A. Kikkawa, S. W. Lovesey and E. Balcar, “Triakontadipole and High-order Dysprosium Multipoles in the Antiferromagnetic Phase of DyB<sub>2</sub>C<sub>2</sub>,” *Journal of Physics: Condensed Matter*, **vol. 23**, p. 266002, 2011.
- [82] A. M. Mulders, U. Staub, V. Scagnoli, Y. Tanaka, A. Kikkawa, K. Katsumata and J. M. Tonnerre, “Manipulating 4f Quadrupolar Pair-interactions in TbB<sub>2</sub>C<sub>2</sub> using A Magnetic Field,” *Physical Review B*, **vol. 75**, p. 184438, 2007.
- [83] A. J. Princep, A. M. Mulders, E. Schierle, E. Weschke, J. Hester, W. D. Hutchison, Y. Tanaka, N. Terada, Y. Narumi and T. Nakamura, “High-order Ho Multipoles in HoB<sub>2</sub>C<sub>2</sub> Observed with Soft Resonant X-ray Diffraction,” *Journal of Physics: Condensed Matter*, **vol. 24**, p. 075602, 2012.
- [84] I. Shirotni, J. Hayashi, T. Adachi, C. Sekine, T. Kawakami, T. Nakanishi, H. Takahashi, J. Tang, A. Matsushita and T. Matsumoto, “Metal to insulator transition of filled skutterudite PrRu<sub>4</sub>P<sub>12</sub> at low temperatures and high pressures,” *Physica B: Condensed Matter*, **vol. 322**, **no. 3–4**, p. 408, 2002.
- [85] S. W. Lovesey, E. Balcar, C. Detlefs, G. van der Laan, D. S. Sivia and U. Staub, “Neptunium Octupole and Hexadecapole Motifs in NpO<sub>2</sub> Directly from Electric Dipole (E1) Enhanced X-Ray Bragg Diffraction,” *Journal of Physics: Condensed Matter*, **vol. 15**, **no. 26**, p. 4511, 2003.
- [86] L. Hao, K. Iwasa, K. Kuwahara, M. Kohgi, S. R. Saha, H. Sugawara, Y. Aoki, H. Sato, C. Sekine, C. H. Lee and H. Harima, “Crystal-Lattice

- Modulation of the Metal-Insulator Transition System  $\text{PrRu}_4\text{P}_{12}$  Studied by X-Ray Diffraction,” *Journal of Magnetism and Magnetic Materials*, **vol. 272**, p. E271, 2004.
- [87] K. Iwasa, L. J. Hao, K. Kuwahara, M. Kohgi, S. R. Saha, H. Sugawara, Y. Aoki, H. Sato, T. Tayama and T. Sakakibara, “Evolution of 4f Electron States in the Metal-Insulator Transition of  $\text{PrRu}_4\text{P}_{12}$ ,” *Physical Review B*, **vol. 72**, **no. 2**, p. 024414, 2005.
- [88] K. Matsuhira, Y. Hinatsu, C. Sekine and I. Shirotni, “Specific Heat around Metal-Insulator Transition of Filled Skutterudite  $\text{PrRu}_4\text{P}_{12}$ ,” *Physica B*, **vol. 312**, p. 829, 2002.
- [89] Z. Hu, G. Kaindl, H. Ogasawara, A. Kotani and I. Felner, “Ln-4f/ligand-2p Covalence in  $\text{BaLnO}_3$  and  $\text{Cs}_3\text{LnF}_7$  (Ln=Ce, Pr, Tb),” *Chemical Physics Letters*, **vol. 325**, **no. 1-3**, p. 241, 2000.
- [90] W. S. Lee, A. P. Sorini, M. Yi, Y. D. Chuang, B. Moritz, W. L. Yang, J. H. Chu, H. H. Kuo, A. G. C. Gonzalez, I. R. Fisher, Z. Hussain, T. P. Devereaux and Z. X. Shen, “Resonant Enhancement of Charge Density Wave Diffraction in the Rare-Earth Tritellurides,” *Physical Review B*, **vol. 85**, **no. 15**, p. 155142, 2012.
- [91] D. Cao, R. H. Heffner, F. Bridges, I. K. Jeong, E. D. Bauer, W. M. Yuhasz and M. B. Maple, “Local Distortion Induced Metal-to-Insulator Phase Transition in  $\text{PrRu}_4\text{P}_{12}$ ,” *Physical Review Letters*, **vol. 94**, **no. 3**, p. 036403, 2005.
- [92] J. Herrero-Martin, G. Subias, J. Garcia, J. Blasco and M. Concepción Sánchez, “Evidence for charge-density-wave nature of the charge-ordered phase in  $\text{La}_{1/3}\text{Sr}_{2/3}\text{FeO}_3$ ,” *Physical Review B*, **vol. 79**, p. 045121, 2009.
- [93] J. Herrero-Martin, J. L. Garcia-Muñoz, S. Valencia, C. Frontera, J. Blasco, A. J. Barón-González, G. Subias, R. Abrudan, F. Radu, E. Dudzik and R. Feyerherm, “Valence change of praseodymium in  $\text{Pr}_{0.5}\text{Ca}_{0.5}\text{CoO}_3$  investigated by x-ray absorption spectroscopy,” *Physical Review B*, **vol. 84**, p. 115131, 2011.
- [94] J. O. Cross, M. Newville, J. J. Rehr, L. B. Sorensen, C. E. Bouldin, G. Watson, T. Gouder, G. H. Lander and M. I. Bell, “Inclusion of local

structure effects in theoretical x-ray resonant scattering amplitudes using ab initio x-ray-absorption spectra calculations,” *Physical Review B*, **vol. 58**, p. 11215, 1998.

- [95] H. Kim, S. Ji, J. Jang, S. Bae and J. Lee, “Formation of  $\text{La}_2\text{Ti}_2\text{O}_7$  crystals from amorphous  $\text{La}_2\text{O}_3$ - $\text{TiO}_2$  powders synthesized by the polymerized complex method,” *Korean Journal of Chemical Engineering*, **vol. 21**, **no. 5**, p. 970, 2004.